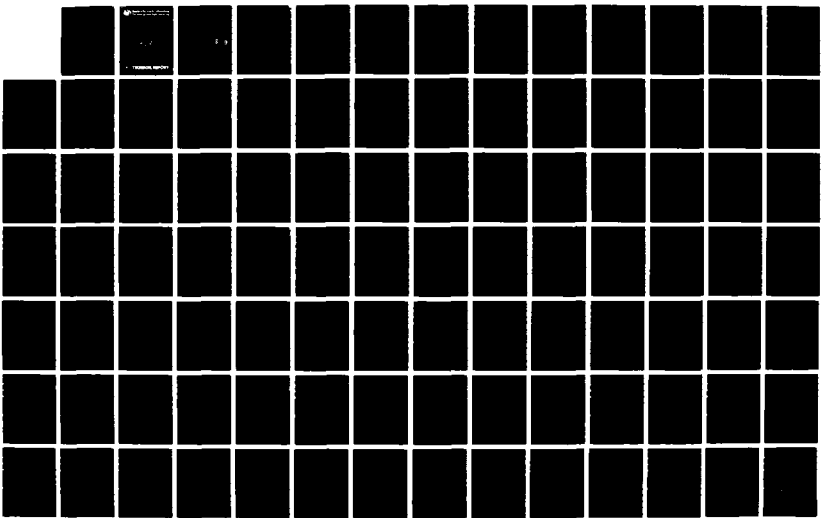
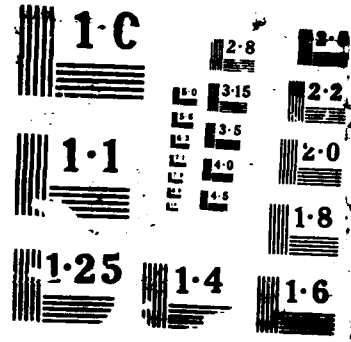


RD-A189 367 ACOUSTIC RADIATION FROM LINE- AND POINT-LLOADED PLATES: 1/2
UNCLASSIFIED UNIFORMLY ASYMPTOT. (U) PENNSYLVANIA STATE UNIV
UNIVERSITY PARK APPLIED RESEARCH LAB. H Y HSU ET AL.
NOV 87 ARL/PSU/TR-87-010 N00024-85-C-6041 F/G 20/1 NL





DTIC FILE COPY



Applied Research Laboratory The Pennsylvania State University

(4)

AD-A189 367

ACOUSTIC RADIATION FROM LINE- AND
POINT-LOADED PLATES: UNIFORMLY
ASYMPTOTIC SOLUTIONS

by

H. Y. Hsu and S. I. Hayek

DTIC
SELECTED
DEC 30 1987
S D

DISTRIBUTION STATEMENT A
Approved for public release
Distribution Unlimited

REF ID: A6520

TECHNICAL REPORT

The Pennsylvania State University
APPLIED RESEARCH LABORATORY
P.O. Box 30
State College, PA 16804

ACOUSTIC RADIATION FROM LINE- AND
POINT-LOADED PLATES: UNIFORMLY
ASYMPTOTIC SOLUTIONS

by

H. Y. Hsu and S. I. Hayek

Technical Report No. TR 87-010
November 1987

DTIC
ELECTED
DEC 30 1987
S D Q

Supported by:
Naval Sea Systems Command

L. R. Hettche
Applied Research Laboratory

Approved for public release; distribution unlimited

87 12 22 078

Unclassified

SECURITY CLASSIFICATION OF THIS PAGE

REPORT DOCUMENTATION PAGE

1a REPORT SECURITY CLASSIFICATION Unclassified		1b. RESTRICTIVE MARKINGS	
2a. SECURITY CLASSIFICATION AUTHORITY		3. DISTRIBUTION/AVAILABILITY OF REPORT (A) Unlimited	
2b. DECLASSIFICATION/DOWNGRADING SCHEDULE			
4 PERFORMING ORGANIZATION REPORT NUMBER(S) TR-87-010		5. MONITORING ORGANIZATION REPORT NUMBER(S)	
6a NAME OF PERFORMING ORGANIZATION Applied Research Laboratory The Penna. State University	6b OFFICE SYMBOL (If applicable) ARL	7a. NAME OF MONITORING ORGANIZATION Naval Sea Systems Command Department of the Navy	
5c ADDRESS (City, State, and ZIP Code) P. O. Box 30 State College, PA 16804		7b. ADDRESS (City, State, and ZIP Code) Washington, DC 20362	
8a. NAME OF FUNDING/SPONSORING ORGANIZATION Naval Sea Systems Command	8b. OFFICE SYMBOL (If applicable) NAVSEA	9. PROCUREMENT INSTRUMENT IDENTIFICATION NUMBER N-00024-85-C-6041	
8c. ADDRESS (City, State, and ZIP Code) Department of the Navy Washington, DC 20362		10. SOURCE OF FUNDING NUMBERS	
		PROGRAM ELEMENT NO.	PROJECT NO.
		TASK NO.	WORK UNIT ACCESSION NO.
11. TITLE (Include Security Classification) ACOUSTIC RADIATION FROM LINE- AND POINT-LOADED PLATES: UNIFORMLY ASYMPTOTIC SOLUTIONS (U)			
12. PERSONAL AUTHOR(S) H. Y. Su and S. T. Havrak			
13a. TYPE OF REPORT Ph.D. Thesis	13b. TIME COVERED FROM _____ TO _____	14. DATE OF REPORT (Year, Month, Day) November 1987	15. PAGE COUNT 140
16. SUPPLEMENTARY NOTATION			
17. COSATI CODES		18. SUBJECT TERMS (Continue on reverse if necessary and identify by block number) Acoustic pressure, asymptotic series, saddle point method, structural damping, fluid-loaded plate, Timoshenko/Mindlin theory	
19. ABSTRACT (Continue on reverse if necessary and identify by block number) The theoretical analysis for predicting the acoustic radiation from an infinite fluid-loaded, elastic plate excited by a line or a point force is presented. The acoustic pressure radiated by this coupled plate-fluid system is obtained by the use of the Fourier transform method for line force excitation and a Hankel transform for point force excitation. The integral representation of the radiated acoustic pressure is evaluated by three methods based on the steepest descent path (SDP). C 6.1			
20. DISTRIBUTION/AVAILABILITY OF ABSTRACT <input checked="" type="checkbox"/> UNCLASSIFIED/UNLIMITED <input type="checkbox"/> SAME AS RPT <input type="checkbox"/> DTIC USERS		21. ABSTRACT SECURITY CLASSIFICATION Unclassified	
22a. NAME OF RESPONSIBLE INDIVIDUAL		22b. TELEPHONE (Include Area Code)	22c. OFFICE SYMBOL

Unclassified

SECURITY CLASSIFICATION OF THIS PAGE

conf'd

The first is the widely used saddle point method which can only lead to the farfield solution. This first-order approximation, due to the contribution at the saddle point, is obtained with the assumption that all the poles of the integrand are located far away from the saddle point and SDP. However, the leaky wave pole may approach the saddle point when the frequency is above the coincidence frequency. Thus, the saddle point method is modified such that all the singularities of the integrand are explicitly isolated regardless of their proximity to the saddle point. (Keywords:
The uniformly asymptotic series solution obtained from this modified method is valid in the farfield and the nearfield, and is especially accurate at the coincidence angle where the saddle point method overpredicts the acoustic pressure. The uniformly asymptotic series solution also predicts a decaying but non-vanishing surface acoustic pressure while the approximate solution from the saddle point method vanishes at the grazing angle. In the farfield, the surface pressure wave propagates unattenuatedly along the surface of the plate for a line force excitation, but decays at a rate $(k_0 R)^{-1/2}$ for a point force excitation.

The third method involves numerical integration along the steepest descent path instead of the original integration path which contains branch cuts in the complex wavenumber plane. Results obtained from the numerical integration are compared with the uniformly asymptotic series solution and an excellent agreement has been observed.

The influence of the structural damping is also investigated. Results show that, in the nearfield, the addition of structural damping has no effect on the acoustic radiation for frequencies below the first coincidence frequency and significantly reduces the radiated pressure above coincidence for all observation angle. In the farfield, structural damping significantly reduces the acoustic pressure only near the coincidence angle for frequencies above the first coincidence frequency.

Unclassified

SECURITY CLASSIFICATION OF THIS PAGE

ABSTRACT

The theoretical analysis for predicting the acoustic radiation from an infinite fluid-loaded, elastic plate excited by a line or a point force is presented. The acoustic pressure radiated by this coupled plate-fluid system is obtained by the use of the Fourier transform method for line force excitation and a Hankel transform for point force excitation. The integral representation of the radiated acoustic pressure is evaluated by three methods based on the steepest descent path (SDP).

The first is the widely used saddle point method which can only lead to the farfield solution. This first-order approximation, due to the contribution at the saddle point, is obtained with the assumption that all the poles of the integrand are located far away from the saddle point and SDP. However, the leaky wave pole may approach the saddle point when the frequency is above the coincidence frequency. Thus, the saddle point method is modified such that all the singularities of the integrand are explicitly isolated regardless of their proximity to the saddle point. The uniformly asymptotic series solution obtained from this modified method is valid in the farfield and the nearfield, and is especially accurate at the coincidence angle where the saddle point method overpredicts the acoustic pressure. The uniformly asymptotic series solution also predicts a decaying but non-vanishing surface acoustic pressure while the approximate solution from the saddle point method vanishes at the grazing angle. In the farfield, the surface pressure wave propagates unattenuatedly along the surface of the plate for a line force excitation, but decays at a rate $(k_0 R)^{-1/2}$ for a point force excitation.

The third method involves numerical integration along the steepest descent path instead of the original integration path which contains branch cuts in the complex wavenumber plane. Results obtained from the numerical integration are compared

with the uniformly asymptotic series solution and an excellent agreement has been observed.

The influence of the structural damping is also investigated. Results show that, in the nearfield, the addition of structural damping has no effect on the acoustic radiation for frequencies below the first coincidence frequency and significantly reduces the radiated pressure above coincidence for all observation angle. In the farfield, structural damping significantly reduces the acoustic pressure only near the coincidence angle for frequencies above the first coincidence frequency.

Accession For	
NTIS	CRA&I <input checked="" type="checkbox"/>
DTIC	TAB <input type="checkbox"/>
Unannounced <input type="checkbox"/>	
Justification _____	
By _____	
Distribution / _____	
Availability Codes	
Dist	A-A1 E-E1 or Special
A-1	



TABLE OF CONTENTS

	<u>Page</u>
ABSTRACT	iii
LIST OF TABLES	vii
LIST OF FIGURES	viii
LIST OF MAJOR SYMBOLS	xii
ACKNOWLEDGMENTS	xiv
<u>Chapter</u>	
1. BACKGROUND	1
1.1 Introduction	1
1.2 Basic Approach	2
2. FORMULATION OF THE PROBLEM	5
2.1 Mathematical Model	5
2.2 Line Force Excitation	6
2.3 Point Force Excitation	9
3. SOLUTION FOR LINE FORCE EXCITATION	12
3.1 Standard Steepest Descent Method	12
3.2 Modified Steepest Descent Method	15
3.3 Numerical Integration	21
4. SOLUTION FOR POINT FORCE EXCITATION	23
4.1 Standard Steepest Descent Method	23
4.2 Modified Steepest Descent Method	24
4.3 Numerical Integration	32
5. NUMERICAL RESULTS AND DISCUSSIONS	33
5.1 Introduction	33
5.2 Pole Contribution	33

5.3 Line Force Excitation	36
5.3.1 Integral Along the Steepest Descent Path	36
5.3.2 Influence of Range ($k_0 r$) on the Solution	37
5.3.3 Radiated Acoustic Pressure	37
5.3.3.1 Frequency Range Below First Coincidence	37
5.3.3.2 Frequency Range $1.23 < \Omega < 6.79$	38
5.3.3.3 Frequency Range Above Second Coincidence	39
5.3.3.4 Radiated Pressure at $\phi = 0^\circ$	39
5.3.3.5 Grazing and Nearfield Radiated Pressure	40
5.3.3.5.1 Surface Wave Pole and Surface Pressure	40
5.3.3.5.2 Nearfield Pressure	41
5.3.3.6 Influence of Structural Damping	43
5.4 Point Force Excitation	44
5.4.1 Integral Along the Steepest Descent Path	44
5.4.2 Radiated Acoustic Pressure	45
5.4.3 Grazing and Nearfield Radiated Pressure	45
6. CONCLUDING REMARKS	47
6.1 Summary and Conclusion	47
6.2 Future Work	48
BIBLIOGRAPHY	122
APPENDIX: THE TAYLOR'S SERIES EXPANSION	124

LIST OF TABLES

	<u>Page</u>
Table 1 Surface wave pole K_0 and $\epsilon(\Omega)$	50

LIST OF FIGURES

	<u>Page</u>
Figure 1 Geometry of a line- or point-excited fluid-loaded elastic plate and the coordinate system.	51
Figure 2 Integration paths and steepest descent path in the complex K - and α -plane.	52
Figure 3 Typical locations of poles in the complex α -plane.	53
Figure 4 Frequency loci of poles in the complex α -plane.	54
Figure 5 Typical locations of poles in the complex Γ - and K -plane.	55
Figure 6 Frequency loci of poles in the complex K -plane.	56
Figure 7 Distance between the saddle point and the poles in the complex α -plane. $\Omega = 1.0$	57
Figure 8 Distance between the saddle point and the poles in the complex α -plane. $\Omega = 5.0$	58
Figure 9 Distance between the saddle point and the poles in the complex α -plane. $\Omega = 10.0$	59
Figure 10 Absolute values of $Im[\cos(\alpha - \phi)]$, $\Omega = 1.0$	60
Figure 11 Absolute values of $Im[\cos(\alpha - \phi)]$, $\Omega = 5.0$	61
Figure 12 Absolute values of $Im[\cos(\alpha - \phi)]$, $\Omega = 10.0$	62
Figure 13 Magnitude of integrand along SDP- line-excited plate at $\Omega = 1.0$ and $\phi = 0^\circ$	63
Figure 14 Magnitude of integrand along SDP- line-excited plate at $\Omega = 1.0$ and $\phi = 60^\circ$	64
Figure 15 Magnitude of integrand along SDP- line-excited plate at $\Omega = 1.0$ and $\phi = 90^\circ$	65
Figure 16 Magnitude of integrand along SDP- line-excited plate at $\Omega = 10.0$ and $\phi = 34^\circ$	66
Figure 17 Magnitude of integrand along SDP- line-excited plate at $\Omega = 10.0$ and $\phi = 11^\circ$	67
Figure 18 Normalized directivity function for a line-excited fluid-loaded steel plate. $k_0 r = 10$, $\Omega = 1.0$	68

Figure 19	Normalized directivity function for a line-excited fluid-loaded steel plate, $k_0 r = 10^2$, $\Omega = 1.0$	71
Figure 20	Normalized directivity function for a line-excited fluid-loaded steel plate, $k_0 r = 10$, $\Omega = 5.0$	74
Figure 21	Normalized directivity function for a line-excited fluid-loaded steel plate, $k_0 r = 10^2$, $\Omega = 5.0$	77
Figure 22	Normalized directivity function for a line-excited fluid-loaded steel plate, $k_0 r = 10^3$, $\Omega = 5.0$	80
Figure 23	Normalized directivity function for a line-excited fluid-loaded steel plate, $k_0 r = 10^4$, $\Omega = 5.0$	81
Figure 24	Normalized directivity function for a line-excited fluid-loaded steel plate, $k_0 r = 10$, $\Omega = 10.0$	82
Figure 25	Normalized directivity function for a line-excited fluid-loaded steel plate, $k_0 r = 10^2$, $\Omega = 10.0$	83
Figure 26	Normalized directivity function for a line-excited fluid-loaded steel plate, $k_0 r = 10^3$, $\Omega = 10.0$	84
Figure 27	Normalized directivity function for a line-excited fluid-loaded steel plate, $k_0 r = 10^5$, $\Omega = 10.0$	85
Figure 28	Radiated pressure from a line-excited steel plate, $\phi = 0^\circ$	86
Figure 29	Grazing pressure field from a line-excited plate, $\Omega = 0.5$	87
Figure 30	Grazing pressure field from a line-excited plate, $\Omega = 5.0$	88
Figure 31	Grazing pressure field from a line-excited plate, $\Omega = 10.0$	89
Figure 32	Nearfield pressure from a line-excited plate, $\Omega = 0.5$	90
Figure 33	Nearfield pressure from a line-excited plate, $\Omega = 5.0$	91
Figure 34	Nearfield pressure from a line-excited plate, $\Omega = 10.0$	92
Figure 35	Radiated pressure from a line-excited steel plate at $\Omega = 1.0$ and $z = 0.01\lambda$	93
Figure 36	Radiated pressure from a line-excited steel plate at $\Omega = 1.0$ and $z = 1.0\lambda$	94
Figure 37	Radiated pressure from a line-excited steel plate at $\Omega = 5.0$ and $z = 0.01\lambda$	95
Figure 38	Radiated pressure from a line-excited steel plate at $\Omega = 5.0$ and $z = 1.0\lambda$	96

Figure 39	Normalized directivity function for a line-excited plate with structural damping, $k_0 r = 10$, $\Omega = 0.5$.	97
Figure 40	Normalized directivity function for a line-excited plate with structural damping, $k_0 r = 10^2$, $\Omega = 5.0$.	98
Figure 41	Normalized directivity function for a line-excited plate with structural damping, $k_0 r = 10^5$, $\Omega = 5.0$.	100
Figure 42	Normalized directivity function for a line-excited plate with structural damping, $k_0 r = 10^2$, $\Omega = 10.0$.	101
Figure 43	Normalized directivity function for a line-excited plate with structural damping, $k_0 r = 10^6$, $\Omega = 10.0$.	102
Figure 44	Grazing pressure field from a line-excited plate with structural damping, $\eta = 0.1$, $\Omega = 0.5$.	103
Figure 45	Grazing pressure field from a line-excited plate with structural damping, $\eta = 0.1$, $\Omega = 5.0$.	104
Figure 46	Grazing pressure field from a line-excited plate with structural damping, $\Omega = 0.5$.	105
Figure 47	Grazing pressure field from a line-excited plate with structural damping, $\Omega = 5.0$.	106
Figure 48	Magnitude of integrand along SDP- point-excited plate at $\Omega = 1.0$ and $\phi = 0^\circ$.	107
Figure 49	Magnitude of integrand along SDP- point-excited plate at $\Omega = 1.0$ and $\phi = 60^\circ$.	108
Figure 50	Magnitude of integrand along SDP- point-excited plate at $\Omega = 1.0$ and $\phi = 90^\circ$.	109
Figure 51	Magnitude of integrand along SDP- point-excited plate at $\Omega = 10.0$ and $\phi = 34^\circ$.	110
Figure 52	Magnitude of integrand along SDP- point-excited plate at $\Omega = 10.0$ and $\phi = 11^\circ$.	111
Figure 53	Radiated pressure from a point-excited steel plate, $\phi = 0^\circ$.	112
Figure 54	Grazing pressure field from a point-excited plate, $\Omega = 0.5$.	113
Figure 55	Grazing pressure field from a point-excited plate, $\Omega = 5.0$.	114
Figure 56	Grazing pressure field from a point-excited plate, $\Omega = 10.0$.	115
Figure 57	Radiated pressure from a point-excited steel plate at $\Omega = 1.0$ and $z = 0.01\lambda$.	116

Figure 58 Radiated pressure from a point-excited steel plate at $\Omega = 1.0$ and $z = 1.0\lambda$.	117
Figure 59 Radiated pressure from a point-excited steel plate at $\Omega = 5.0$ and $z = 0.01\lambda$.	118
Figure 60 Radiated pressure from a point-excited steel plate at $\Omega = 5.0$ and $z = 1.0\lambda$.	119
Figure 61 Radiated pressure from a point-excited steel plate at $\Omega = 10.0$ and $z = 0.01\lambda$.	120
Figure 62 Radiated pressure from a point-excited steel plate at $\Omega = 10.0$ and $z = 1.0\lambda$.	121

LIST OF MAJOR SYMBOLS

A	wavenumber (angular) spectrum function. Eq. (11)
A_r, A_s, A_t	coefficients of the integrand. Eqs. (49) and (75)
$C(\alpha)$	integration path. Eqs. (16) and (29)
C_0, C_1, C_2, C_3	coefficients. Eqs. (17) and (29)
D	bending stiffness of the plate. Eq. (1)
E	Young's modulus
F_1, F_2, F_3, F_5	plate-fluid coefficients. Eqs. (17) and (29)
F_0	amplitude of applied force
G	shear modulus
$H_0^{(1)}$	zero-order Hankel function of first kind
I	rotary inertia factor. Eq. (1)
J_0	zero-order Bessel function
K	normalized wavenumber parallel to plate
K_n	normalized poles of the integrand in the complex K -plane
R	radius in spherical coordinates. $\sqrt{r^2 + z^2}$
S	shear deformation factor. Eq. (1)
a_n^r, a_n^s, a_n^t	coefficients. Eqs. (50) and (77–79)
b_n	a coefficient. Eq. (49)
c	phase velocity of acoustic medium
c_p	phase speed of the plate's longitudinal wave
f_{ij}, g_{ij}, h_{ij}	Taylor series coefficients. Eqs. (80–82)
h	plate thickness
i	imaginary unit. $\sqrt{-1}$
k	wavenumber in the direction parallel to plate
k_n	acoustic wavenumber

k_c	acoustic wavenumber at the classical coincidence frequency
m	mass density of the plate, per unit area
m_i, n_i	coefficients, Eqs. (47) and (74)
$p()$	acoustic pressure in the fluid medium
p_i, q_i	coefficients, Eqs. (47) and (74)
r, z	cylindrical coordinates
x, z	Cartesian coordinates
w	transverse displacement of the plate, Eq. (1)
Φ	fluid velocity potential, Eq. (3)
Ω	normalized radial frequency, ω/ω_c
Γ	normalized wavenumber perpendicular to plate, Eq. (103)
α	a form of the wavenumber
$\bar{\alpha}$	saddle point, Eq. (31)
α_n	poles of the integrand in the complex α -plane
ϕ	observation angle
$\delta()$	Dirac delta function
ω	circular frequency
ω_c	classical coincidence radial frequency
ρ_0	mass density of the acoustic medium
ρ	mass density of the plate material
ν	Poisson's ratio
κ	shear correction factor, $\sqrt{\frac{\pi}{12}}$
χ	a form of the wavenumber, $\sqrt{-i[\cos(\alpha - \theta) - 1]}$, Eq. (45)
χ_n	poles of the integrand in the complex χ -plane.
η	loss factor of plate material, Eq. (106)

ACKNOWLEDGMENTS

The author wishes to express his sincere gratitude to his thesis advisor, Professor Sabih I. Hayek, for suggesting this work, as well as his constant support, guidance and encouragement throughout the entire study. He also wishes to thank Professors Vernon H. Neubert, Vasundara V. Varadan, Courtney B. Burroughs, and Alan D. Stuart for serving on the author's doctoral committee. Special thanks are due to his wife, Lin-Hwa, and to his parents, Mr. and Mrs. Yao-Chie Hsu, for their encouragement and forbearance.

This research has been supported by the Applied Research Laboratory of The Pennsylvania State University under the contract with the U.S. Naval Sea Systems Command.

CHAPTER 1

BACKGROUND

1.1 Introduction

Large portions of many structures consist of plates and panels, which are susceptible to flexural vibrations. The vibrating structures, in turn, radiate acoustic energy from their surfaces into the surrounding medium. Although the applications of damping mechanisms would reduce the vibration level and hence the acoustic radiation, the study of acoustic radiation from an elastic surface still plays an important role and constitutes one of the major areas of concern in acoustics.

Numerous studies have been devoted to acoustic radiation from vibrating structures. The first solution to the radiated power from an elastic plate modeled by the classical plate theory was obtained by Skudrzyk [1-2] and Heckl [3-5] for a time-harmonic point force, and by Thompson and Rattaya [6] for a time-harmonic point moment. The solution for the acoustic radiated pressure from a point-excited plate using the classical plate theory was given by Gutin [7], Feit [8] and by Skudrzyk [9]. The influence of fluid loading on the radiation from an elastic plate was investigated by Maidanik and Kerwin [10]. All of these investigations employed the classical plate theory which fails at high frequencies where the phase and group velocities become infinite as the frequency or the wavenumber becomes unbound.

To improve the high-frequency prediction of the acoustic radiation from an elastic plate excited by a point force, Feit [11] employed the Timoshenko-Mindlin plate theory which accounts for the transverse shear and rotary inertia of the plate. Unlike the classical plate theory, the Timoshenko-Mindlin plate theory correctly predicts the high-frequency flexural phase velocity of the plate. Feit, however, confined his analysis to time-harmonic frequencies below the second coincidence

frequency. Stuart [12–13] considered the same problem with the excitation frequency extended above the second coincidence frequency and thus predicted a second lobe in the radiation pattern due to the thickness shear pole. His solution, with new insights into the leaky waves emanating from the plate, is more accurate when the angle of observation approaches the coincidence angle.

Since the leaky wave poles may approach the saddle point, the first order approximation, obtained from the standard saddle point method by Feit [11] and Stuart [12–13], vanishes at the grazing angle and significantly overpredicts the radiated nearfield acoustic pressure near the coincidence angle. Seren [14] recently used the modified saddle point method to accurately predict the nearfield scattered pressure from an elastic plate with line force and line moment impedance discontinuities due to an incident acoustic plane wave.

In this thesis, the modified saddle point method is used to predict the radiated acoustic pressure, which is expressed in terms of a uniformly asymptotic series. This asymptotic series solution is valid in the farfield and the nearfield, and is especially accurate at the grazing angle.

1.2 Basic Approach

The structure considered in this thesis is an infinite fluid-loaded plate excited by a time-harmonic force. Although it is known that the infinite plate does not exist in reality, the justification for this assumption lies in the fact that the structural damping of the plate is sufficient to neglect boundary-reflected waves, which are assumed to be of relatively small amplitudes as compared to the waves propagating from the excitation point.

Throughout this study, the plate is assumed to be homogeneous, elastic and isotropic. Instead of using the classical plate theory, the Timoshenko-Mindlin theory for plates (or thick plate theory) is considered which includes the transverse shear and rotary inertia effects. These transverse shear and rotary inertia corrections

to the plate equations will be shown to provide two coincidence effects and thus generate two peaks in the acoustic radiation pattern at frequencies above the second coincidence.

The wave motion in the acoustic medium is derived for the fluid velocity potential. At the plate-fluid interface, the fundamental boundary condition of continuity of normal velocity is applied to the coupled plate-fluid system. Two types of excitation, i.e., line and point force, are studied in this thesis and the radiated acoustic pressure is obtained from three different methods, which originate from the same integral representation along the steepest descent path.

The first method used in the analysis is the well-known method of the steepest descent path, also known as the saddle point method, which is based on the assumption that all the singularities of the integrand are located far away from the saddle point and the steepest descent path. Consequently, it can only lead to a farfield solution. As will be seen in the following chapters, this method overpredicts the radiated pressure in the nearfield, especially at the coincidence angles. In order to properly treat these limitations, the saddle point method is modified.

The modified steepest descent method explicitly isolates all the singularities of the integrand and results in a uniformly asymptotic series solution valid not only in the farfield, but in the nearfield. The grazing field can be accurately predicted by this modified saddle point method, since the first order approximation to the solution by the standard steepest descent method vanishes at the surface of the plate.

The third method involves numerical integration along the steepest descent path, where the integrand becomes an exponentially-decaying, non-oscillating function. Results obtained from the numerical integration are compared with those predicted from the previous two methods. As will be seen later, the excellent agreement between the uniformly asymptotic series solution and the numerical

integration indicates that the modified steepest descent method can accurately predict the farfield and the nearfield acoustic radiation from a vibrating plate.

CHAPTER 2

FORMULATION OF THE PROBLEM

2.1 Mathematical Model

The generalized Timoshenko-Mindlin (T-M) plate equation of motion is given by

[15]

$$\begin{aligned} & [(\nabla^2 - \frac{m}{D} S \frac{\partial^2}{\partial t^2})(D \nabla^2 - m I \frac{\partial^2}{\partial t^2}) + m \frac{\partial^2}{\partial t^2}] w(\vec{r}, t) \\ & = (1 - S \nabla^2 + \frac{m}{D} S I \frac{\partial^2}{\partial t^2}) f(\vec{r}, t), \end{aligned} \quad (1)$$

where

∇^2 is the Laplacian operator.

$D = \frac{Eh^3}{12(1-\nu^2)}$ is the plate bending rigidity.

E is the Young's modulus of the plate.

h is the thickness of the plate.

ν is the Poisson's ratio of the plate.

$S = \frac{D}{\kappa^2 G h}$ is the shear deformation factor.

G is the shear modulus of the plate.

$\kappa^2 = \frac{\pi^2}{12}$ is the shear correction factor.

$I = \frac{h^2}{12}$ is the rotary inertia factor.

$m = \rho h$ is the mass density of plate per unit area.

ρ is the mass density of the plate.

and $w(\vec{r}, t)$ is the transverse displacement due to the total transverse loading $f(\vec{r}, t)$ which represents the combination of both the external mechanical forces and the surface acoustic pressure. Two types of external forces, i.e., the line and point forces, are studied in this thesis.

The acoustic wave equation for the fluid velocity potential, Φ , is given by

$$\nabla^2 \Phi(\vec{r}, t) = \frac{1}{c^2} \frac{\partial^2 \Phi(\vec{r}, t)}{\partial t^2}, \quad (2)$$

where c is the phase velocity in the acoustic medium.

The acoustic pressure is related to the velocity potential by

$$p(\vec{r}, t) = \rho_0 \frac{\partial \Phi(\vec{r}, t)}{\partial t}, \quad (3)$$

where ρ_0 is the fluid mass density.

2.2 Line Force Excitation

For a line-excited, fluid-loaded elastic plate, as shown in Fig. 1, the total transverse loading can be expressed as

$$f(x, t) = F(t)\delta(x) - p(x, z = 0^+, t), \quad (4)$$

where $F(t)\delta(x)$ represents the line force applied at $x = 0$ and the rectangular coordinate system has been used.

For a time-harmonic dependent line force excited at a circular frequency ω . $F(t) = F_0 e^{-i\omega t}$, one can suppress the time dependence and the T-M plate equation of motion becomes

$$\begin{aligned} & [(\nabla^2 + \frac{m}{D} S \omega^2)(D \nabla^2 + m I \omega^2) - m \omega^2] w(x) \\ &= (1 - S \nabla^2 - \frac{m}{D} S I \omega^2)[F_0 \delta(x) - p(x, z = 0^+)]. \end{aligned} \quad (5)$$

Letting $\Phi = \bar{\Phi} e^{-i\omega t}$, the acoustic wave equation can be expressed in terms of acoustic pressure as

$$[\frac{\partial^2}{\partial x^2} + \frac{\partial^2}{\partial z^2} - k_0^2] p(x, z) = 0, \quad (6)$$

where $k_0 = \omega/c$ is the acoustic wavenumber excited at frequency ω .

Define the complex Fourier transform pairs as follows:

$$\bar{p}(k, z) = \int_{-\infty}^{+\infty} p(x, z) e^{-ikx} dx, \quad (7)$$

and

$$p(x, z) = \frac{1}{2\pi} \int_{-\infty}^{+\infty} \bar{p}(k, z) e^{ikx} dk. \quad (8)$$

By taking the complex Fourier transform of Eqs. (5) and (6), the plate equation of motion and the acoustic wave equation become

$$\begin{aligned} & [(-k^2 + \frac{m}{D} S \omega^2)(-Dk^2 + mI\omega^2) - m\omega^2] \bar{w}(k) \\ &= (1 + Sk^2 - \frac{m}{D} SI\omega^2) [F_0 - \bar{p}(k, z = 0^+)] \end{aligned} \quad (9)$$

and

$$[\frac{\partial^2}{\partial z^2} + (k_0^2 - k^2)] \bar{p}(k, z) = 0. \quad (10)$$

The solution to Eq. (10) can be obtained as

$$\bar{p}(k, z) = A e^{i\sqrt{k_0^2 - k^2} z}, \quad (11)$$

where A is the wavenumber (angular) spectrum function for the plate. In order to solve for the unknown constant A in the transformed k -plane, one should introduce the continuity equation given as

$$\frac{\partial \bar{p}}{\partial z}(k, z = 0^+) = \rho_0 \omega^2 \bar{w}(k), \quad (12)$$

which essentially states that the normal velocity at the plate-fluid interface must be continuous.

Applying the boundary condition, Eq. (12), to Eq. (11), and substituting the transformed displacement $\bar{w}(k)$ into Eq. (9), results in

$$\bar{w}(k) = \frac{i}{\rho_0 \omega^2} \sqrt{k_0^2 - k^2} A, \quad (13)$$

and

$\Omega = \frac{\omega}{\omega_c}$ is the normalized frequency.

$\omega_c = c^2 \sqrt{\frac{m}{D}} = c^2 \sqrt{\frac{12(1-\nu^2)\rho}{Eh^2}} = \frac{\sqrt{12}c^2}{c_p h}$ is the classical coincidence frequency.

$k_c = \frac{\omega_c}{c}$ is the acoustic wavenumber at ω_c .

$c_p^2 = \frac{E}{(1-\nu^2)\rho}$ is the phase speed of the plate longitudinal wave.

For the Bernoulli-Euler plate, one can obtain the radiated acoustic pressure by neglecting the transverse shear and rotary inertia effects, or simply substituting $S = I = 0$ in Eq. (17).

2.3 Point Force Excitation

For a point-excited, fluid-loaded elastic plate, shown in Fig. 1, the total transverse loading which consists the external force and the acoustic pressure at the plate surface can be expressed as

$$f(r, t) = F(t) \frac{\delta(r)}{2\pi r} - p(r, z = 0^+, t), \quad (18)$$

where $F(t) \frac{\delta(r)}{2\pi r}$ represents the point force applied at $r = 0$ in the cylindrical coordinate system.

For a time harmonic point force, the T-M plate equation of motion and the acoustic wave equation become

$$\begin{aligned} & [(\nabla^2 + \frac{m}{D} S \omega^2)(D \nabla^2 + m I \omega^2) - m \omega^2] w(r) \\ &= (1 - S \nabla^2 - \frac{m}{D} S I \omega^2) [F_0 \frac{\delta(r)}{2\pi r} - p(r, z = 0^+)], \end{aligned} \quad (19)$$

and

$$[\nabla^2 + \frac{\partial^2}{\partial z^2} - k_0^2] p(r, z) = 0. \quad (20)$$

The Hankel transform is applied to the spatial coordinate r and the transform pairs are defined as

$$\bar{p}(k, z) = \int_0^\infty p(r, z) J_0(kr) r dr, \quad (21)$$

where

$$A = \frac{G(k^2, \omega^2)F_0}{G(k^2, \omega^2) + iDF(k^2, \omega^2)\sqrt{\frac{k_0^2 - k^2}{\rho_0\omega^2}}}, \quad (14.1)$$

$$G(k^2, \omega^2) = 1 + Sk^2 - \frac{m\omega^2}{D}IS, \quad (14.2)$$

and

$$F(k^2, \omega^2) = k^4 - \frac{m\omega^2}{D}(I + S)k^2 + \left(\frac{m\omega^2}{D}\right)^2 IS - \frac{m\omega^2}{D}. \quad (14.3)$$

Finally, the pressure field can be obtained by taking the inverse Fourier transform and expressed as

$$p(x, z) = \frac{\rho_0\omega^2 F_0}{2\pi} \int_{-\infty}^{+\infty} \frac{G(k^2, \omega^2)e^{i(\sqrt{k_0^2 - k^2}z + kz)}}{\rho_0\omega^2 G(k^2, \omega^2) + iD\sqrt{k_0^2 - k^2}F(k^2, \omega^2)} dk. \quad (15)$$

To eliminate the integration along the branch cuts in the k -plane, one may use the transformation $k = k_0 \sin \alpha$, $x = r \sin \phi$, and $z = r \cos \phi$. Thus, the pressure field in the cylindrical coordinate system becomes

$$p(r, \phi) = \frac{\rho_0\omega^2 F_0}{2\pi D} \int_{C(\alpha)} \frac{G(k_0^2 \sin^2 \alpha, \omega^2)e^{ik_0 r \cos(\alpha - \phi)}}{\frac{\rho_0\omega^2}{Dk_0}G(k_0^2 \sin^2 \alpha, \omega^2) + i \cos \alpha F(k_0^2 \sin^2 \alpha, \omega^2)} \cos \alpha d\alpha. \quad (16)$$

The integration paths in the complex K - and α -plane are shown in Fig. 2, where $K = k/k_0$. Eq. (16) can be simplified to

$$p(r, \phi) = \frac{\rho_0 F_0}{2\pi m\Omega^2} \int_{C(\alpha)} \frac{(C_0 + C_2 k_0^2 \sin^2 \alpha) \cos \alpha e^{ik_0 r \cos(\alpha - \phi)}}{(F_5 + F_3 \sin^2 \alpha) + i \cos \alpha (\sin^4 \alpha - F_1 \sin^2 \alpha + F_2)} d\alpha, \quad (17)$$

where

$$F_1 = k_c^2(S + I),$$

$$F_2 = k_c^4 SI - \frac{1}{\Omega^2},$$

$$F_3 = \frac{\rho_0 S k_c}{m\Omega},$$

$$F_5 = \frac{\rho_0(1 - \Omega^2 k_c^4 SI)}{mk_c \Omega^2},$$

$$C_0 = 1 - k_c^4 \Omega^2 SI,$$

$$C_2 = S,$$

and

$$p(r, z) = \int_0^\infty \bar{p}(k, z) J_0(kr) k dk. \quad (22)$$

By taking the Hankel transform, Eqs. (19) and (20) become

$$\begin{aligned} D[k^4 - \frac{m\omega^2}{D}(I + S)k^2 + (\frac{m\omega^2}{D})^2 IS - \frac{m\omega^2}{D}] \bar{w}(k) \\ = (1 + Sk^2 - \frac{m}{D} SI\omega^2)[\frac{F_0}{2\pi} - \bar{p}(k, z = 0^+)] \end{aligned} \quad (23)$$

and

$$[\frac{\partial^2}{\partial z^2} + (k_0^2 - k^2)]\bar{p}(k, z) = 0. \quad (24)$$

As discussed in the previous section, the transformed displacement $\bar{w}(k)$ is obtained and expressed as

$$\bar{w}(k) = \frac{i}{\rho_0\omega^2} \sqrt{k_0^2 - k^2} A, \quad (13)$$

where

$$A = \frac{G(k^2, \omega^2) \frac{F_0}{2\pi}}{G(k^2, \omega^2) + iD F(k^2, \omega^2) \frac{\sqrt{k_0^2 - k^2}}{\rho_0\omega^2}}, \quad (25)$$

and $G(\dots)$ and $F(\dots)$ are shown in Eqs. (14.2) and (14.3), respectively.

Finally, the integral representation of the pressure field can be obtained by applying the inverse Hankel transform to Eq. (9). Thus,

$$p(r, z) = \frac{\rho_0\omega^2 F_0}{2\pi} \int_0^\infty \frac{G(k^2, \omega^2) J_0(kr) e^{i\sqrt{k_0^2 - k^2}z}}{\rho_0\omega^2 G(k^2, \omega^2) + iD \sqrt{k_0^2 - k^2} F(k^2, \omega^2)} k dk. \quad (26)$$

By using the Sommerfeld circuit relations, the zero-order Bessel function can be expressed in terms of zero-order Hankel function as

$$J_0(x) = \frac{1}{2}[H_0^{(1)}(x) - H_0^{(1)}(-x)], \quad (27)$$

and Eq. (26) then becomes

$$p(r, z) = \frac{\rho_0\omega^2 F_0}{4\pi} \int_{-\infty}^{+\infty} \frac{G(k^2, \omega^2) H_0^{(1)}(kr) e^{i\sqrt{k_0^2 - k^2}z}}{\rho_0\omega^2 G(k^2, \omega^2) + iD \sqrt{k_0^2 - k^2} F(k^2, \omega^2)} k dk. \quad (28)$$

Again, to eliminate the integration along the branch cuts, the transformation $k = k_0 \sin\alpha$, $r = R \sin\phi$, and $z = R \cos\phi$ are used and the pressure field in the spherical coordinate is of the form

$$p(R, \phi) = \frac{\rho_0 F_0}{4\pi m \Omega^2} \int_{C(\alpha)} \frac{(C_1 + C_3 k_0^2 \sin^2 \alpha) H_0^{(1)}(k_0 R \sin\phi \sin\alpha) k_0 \sin\alpha \cos\alpha e^{ik_0 R \cos\alpha \cos\phi}}{(F_5 + F_3 \sin^2 \alpha) + i \cos\alpha (\sin^4 \alpha - F_1 \sin^2 \alpha + F_2)} d\alpha, \quad (29)$$

where F 's are shown in Eq. (17) and the constants C_1 and C_3 are the same as C_0 and C_2 in Eq. (17), respectively.

CHAPTER 3

SOLUTION FOR LINE FORCE EXCITATION

3.1 Standard Steepest Descent Method

Consider a general integral of the form $I = \int_{C(\alpha)} F(\alpha) e^{\rho f(\alpha)} d\alpha$ with a large parameter ρ , where $f(\alpha)$ and $F(\alpha)$ are arbitrary analytic functions of the complex variable α and $C(\alpha)$ is the path of integration in the complex α -plane. For the integral in Eq. (17), one has $\rho = k_0 r$ and

$$f(\alpha) = i \cos(\alpha - \phi) = f_1(\alpha) + i f_2(\alpha), \quad (30)$$

where $\alpha = \alpha_r + i\alpha_i$, $f_1(\alpha) = \sin(\alpha_r - \phi) \sinh \alpha_i$ and $f_2(\alpha) = \cos(\alpha_r - \phi) \cosh \alpha_i$.

The path of integration is chosen such that f_1 has a maximum value at some point and decreases as rapidly as possible with distance from this point. The location of this point, $\alpha = \bar{\alpha} = \bar{\alpha}_r + i\bar{\alpha}_i$, is defined by the root of the equation

$$\frac{df(\alpha)}{d\alpha} \Big|_{\alpha=\bar{\alpha}} = -i \sin(\bar{\alpha} - \phi) = 0. \quad (31)$$

The solution to Eq. (31) is $\bar{\alpha} - \phi = n\pi$, for $n = 0, 1, 2, \dots$. The choice of $n = 0$ gives the saddle point in the range $-\pi/2 < \alpha < \pi/2$ at $\bar{\alpha}_r = \phi$ and $\bar{\alpha}_i = 0$, and the location of saddle point is mathematically equal to the observation angle.

Since $f(\alpha)$ is an analytic function and both f_1 and f_2 are harmonic functions, i.e., $\nabla^2 f_1 = 0$ and $\nabla^2 f_2 = 0$, $f(\alpha)$ cannot have maxima or minima in the entire α -plane. Hence, the point where Eq. (31) is satisfied is a stationary point. The topography near $\bar{\alpha}$ would be a surface that resembles a saddle, i.e., paths originating from the saddle point $\bar{\alpha}$ could either descend or ascend.

On the steepest path in the complex plane, the imaginary and real parts of the analytic function $f(\alpha)$, f_1 and f_2 , are such that the lines of most rapid change in f_1

correspond to those where f_2 is constant. Thus, the path of steepest change, either descent or ascent, is defined by the equation

$$f_2(\alpha) = f_2(\bar{\alpha}) = \text{constant}. \quad (32)$$

or

$$\cos(\alpha_r - \phi) \cosh \alpha_i = 1. \quad (33)$$

The steepest descent path (SDP), shown in Fig. 2, is then chosen such that $f_1(\alpha) - f_1(\bar{\alpha}) < 0$ and the integrand decays exponentially at the fastest rate as the point of interest moves away from the saddle point along the SDP. The orientations of the SDP at the saddle point can be shown to be $-\pi/4$ and $3\pi/4$. It is convenient to express the SDP as the locus of the points given by

$$s^2 = f(\phi) - f(\alpha) = i - f(\alpha), \quad -\infty < s < +\infty. \quad (34)$$

Since $f(\alpha)$ always contains a constant phase term i along the SDP, the transformation given in Eq. (34) makes the SDP coincide with the real axis of the complex s -plane and the saddle point $\bar{\alpha} \approx \phi$ correspond to $s = 0$. The choice of s^2 instead of s in Eq. (34) insures that the integrand decays exponentially with $k_{nr}s^2$ for the real variable s ranging from $-\infty$ to $+\infty$.

Using the notation

$$F(\alpha) \frac{d\alpha}{ds} = G(s), \quad (35)$$

the general integral then becomes

$$I = \int_{C(\alpha)} e^{\rho f(\alpha)} F(\alpha) d\alpha = e^{\rho f(\phi)} \int_{-\infty}^{+\infty} e^{-\rho s^2} G(s) ds. \quad (36)$$

Again, expanding $G(s)$ about the saddle point $s = 0$,

$$G(s) = G(0) + G'(0)s + \frac{1}{2!} G''(0)s^2 + \dots \quad (37)$$

and the integral can be expressed as

$$I = e^{\rho f(\phi)} \{ G(0) \int_{-\infty}^{+\infty} e^{-\rho s^2} ds + G'(0) \int_{-\infty}^{+\infty} e^{-\rho s^2} s ds + \dots \}. \quad (38)$$

For large ρ , i.e., $\rho \gg 1$, Eq. (38) can be approximated by keeping only the leading term as

$$I = e^{\rho f(\phi)} G(0) \sqrt{\frac{\pi}{\rho}}, \quad (39)$$

where $\rho = k_0 r$ and $f(\phi) = i$. Thus, the first order approximation of the integral is obtained as

$$I_{SDP} \approx \sqrt{\frac{2\pi}{k_0 r}} e^{i(k_0 r - \frac{\pi}{4})} F(\phi), \quad (40)$$

where

$$F(\phi) = \frac{(C_0 + C_2 k_0^2 \sin^2 \phi) \cos \phi}{(F_5 + F_3 \sin^2 \phi) + i \cos \phi (\sin^4 \phi - F_1 \sin^2 \phi + F_2)}. \quad (41)$$

The total radiated pressure field has the form

$$p(r, \phi) = \frac{\rho_0 F_0}{2\pi m \Omega^2} \{ I_{SDP} + 2\pi i \sum res \text{ (between } C(\alpha) \text{ and SDP)} \}, \quad (42)$$

and

$$res(\alpha_j) = \frac{\bar{N}(\alpha) e^{ik_0 r \cos(\alpha - \phi)}}{2F_3 \sin \alpha \cos \alpha + i \bar{D}(\alpha)}|_{\alpha=\alpha_j}, \quad (43)$$

where

$$\bar{N}(\alpha) = \cos \alpha (C_0 + C_2 k_0^2 \sin^2 \alpha)$$

and

$$\bar{D}(\alpha) = -\sin^5 \alpha + 4\sin^3 \alpha \cos^2 \alpha + F_1 \sin^3 \alpha - 2F_1 \sin \alpha \cos^2 \alpha - F_2 \sin \alpha.$$

Note that there are 10 poles in the complex α -plane, but only those located between the original integration path and the SDP would contribute to the radiated acoustic pressure. Figure 2 shows the original integration path and the SDP. The

typical locations and the frequency loci of the α -poles are given in Figures 3 and 4, respectively.

3.2 Modified Steepest Descent Method

In the standard steepest descent method, the integral for the acoustic pressure is approximated by taking only the leading term of the Taylor's series expansion about the saddle point. However, it is not an acceptable approximation if the poles approach the saddle point, because the Taylor's series expansion converges only in the region with a radius of convergence equal to the distance from the saddle point to the nearest singularity. Therefore, the standard steepest descent method must be modified so that all the singularities of the integrand are explicitly isolated. The asymptotic series solution obtained from this modified method is valid in the whole field, while the saddle point contribution leads to the farfield solution only.

The total pressure is the sum of the integration along the SDP and the pole contributions. Thus,

$$p(r, \phi) = \frac{\rho_0 F_0}{2\pi m \Omega^2} \left\{ \int_{SDP} \frac{(C_0 + C_2 k_0^2 \sin^2 \alpha) \cos \alpha e^{ik_0 r \cos(\alpha - \phi)}}{(F_5 + F_3 \sin^2 \alpha) + i \cos \alpha (\sin^4 \alpha - F_1 \sin^2 \alpha + F_2)} d\alpha \right. \\ \left. + 2\pi i \sum (\text{residues of poles crossed by SDP}) \right\}. \quad (44)$$

As mentioned earlier, the steepest descent path is the locus of points given by

$$\chi^2 = f(\phi) - f(\alpha) = i - f(\alpha), \quad \text{where } -\infty < \chi < \infty.$$

Thus,

$$\chi^2 = -i(\cos \alpha^* - 1) = 2i \sin^2 \frac{\alpha^*}{2}, \quad (45)$$

where $\alpha^* = \alpha - \phi$ and χ^2 is real-valued along the SDP. The following identities are obtained from Eq. (45):

$$\cos \alpha^* = 1 + i\chi^2, \quad \sin \alpha^* = \chi \sqrt{\chi^2 - 2i}, \quad \text{and} \quad d\alpha^* = \frac{\sqrt{2} e^{-i\pi/4}}{\sqrt{1 + \frac{i\chi^2}{2}}} d\chi. \quad (46)$$

Now, the integral along the SDP can be written as:

$$I_{SDP}(r, \phi) = \sqrt{2} e^{i(k_0 r - \frac{\pi}{4})} \int_{-\infty}^{+\infty} \frac{N(\chi)}{D(\chi)} \frac{e^{-k_0 r \chi^2}}{\sqrt{1 + \frac{i\chi^2}{2}}} d\chi, \quad (47)$$

where

$$D(\chi) = D_0 + iD_1(\chi) + i\chi\sqrt{\chi^2 - 2i\sin\phi}D_2(\chi),$$

$$D_0 = F_3 + F_5,$$

$$D_1 = q_5 i\chi^{10} + q_4 \chi^8 + q_3 i\chi^6 + q_2 \chi^4 + q_1 i\chi^2 + q_0,$$

$$q_5 = \cos^5 \phi + 5\sin^4 \phi \cos \phi - 10\sin^2 \phi \cos^3 \phi,$$

$$q_4 = 5\cos^5 \phi + 25\sin^4 \phi \cos \phi - 50\sin^2 \phi \cos^3 \phi,$$

$$\begin{aligned} q_3 = & -10\cos^5 \phi - 40\sin^4 \phi \cos \phi + 90\sin^2 \phi \cos^3 \phi + 3(F_1 - 2)\sin^2 \phi \cos \phi \\ & - (F_1 - 2)\cos^3 \phi, \end{aligned}$$

$$\begin{aligned} q_2 = & -10\cos^5 \phi - 20\sin^4 \phi \cos \phi + 70\sin^2 \phi \cos^3 \phi + 9(F_1 - 2)\sin^2 \phi \cos \phi \\ & - 3(F_1 - 2)\cos^3 \phi + i(-F_3 \cos^2 \phi + F_3 \sin^2 \phi), \end{aligned}$$

$$\begin{aligned} q_1 = & 5\cos^5 \phi - 20\sin^2 \phi \cos^3 \phi - 6(F_1 - 2)\sin^2 \phi \cos \phi \\ & + 3(F_1 - 2)\cos^3 \phi (1 + F_2 - F_1) \cos \phi - i2(-F_3 \cos^2 \phi + F_3 \sin^2 \phi), \end{aligned}$$

$$q_0 = \cos^5 \phi + (F_1 - 2)\cos^3 \phi + (1 + F_2 - F_1)\cos \phi + i(F_3 \cos^2 \phi).$$

$$D_2(\chi) = p_4 \chi^8 + p_3 i\chi^6 + p_2 \chi^4 + p_1 i\chi^2 + p_0,$$

and

$$p_4 = -\sin^4 \phi - 5\cos^4 \phi + 10\sin^2 \phi \cos^2 \phi,$$

$$p_3 = 4\sin^4 \phi + 20\cos^4 \phi - 40\sin^2 \phi \cos^2 \phi,$$

$$p_2 = 4\sin^4 \phi + 30\cos^4 \phi - 50\sin^2 \phi \cos^2 \phi + 3(F_1 - 2)\cos^2 \phi - (F_1 - 2)\sin^2 \phi,$$

$$p_1 = -20\cos^4 \phi + 20\sin^2 \phi \cos^2 \phi - 6(F_1 - 2)\cos^2 \phi - 2(F_1 - 2)\sin^2 \phi - i2F_3 \cos \phi,$$

$$p_0 = -5\cos^4 \phi - 3(F_1 - 2)\sin^2 \phi - (1 + F_2 - F_1) - i2F_3 \cos \phi.$$

$$N(\chi) = n_3 i\chi^6 + n_2 \chi^4 + n_1 i\chi^2 + n_0 + \chi \sqrt{\chi^2 - 2i} (m_2 \chi^4 + m_1 i\chi^2 + m_0),$$

and

$$n_3 = C_2 k_0^2 (-3 \sin^2 \phi \cos \phi + \cos^3 \phi),$$

$$n_2 = 3C_2 k_0^2 (-3 \sin^2 \phi \cos \phi + 3 \cos^3 \phi),$$

$$n_1 = C_0 \cos \phi + C_2 k_0^2 (7 \sin^2 \phi \cos \phi - 2 \cos^3 \phi),$$

$$n_0 = C_2 k_0^2 \sin^2 \phi \cos \phi + C_0 \cos \phi,$$

$$m_2 = C_2 k_0^2 (-3 \cos^2 \phi \sin \phi + \sin^3 \phi),$$

$$m_1 = C_2 k_0^2 (6 \cos^2 \phi \sin \phi - 2 \sin^3 \phi),$$

$$m_0 = -C_0 \sin \phi + C_2 k_0^2 (2 \cos^2 \phi \sin \phi - \sin^3 \phi).$$

In Eq. (47), the poles can be isolated by expanding the integrand into partial fractions. The χ -poles can be found directly from the α -poles through the transformation given in Eq. (45). However, it is not easy to expand the integrand, since the denominator contains the square-root term, $\sqrt{\chi^2 - 2i}$. To eliminate the square-root term and to expand the denominator into a polynomial of χ , it is necessary to multiply both the numerator and the denominator by $D^*(\chi)$ given as

$$D^*(\chi) = D_0 + iD_1(\chi) - i\chi\sqrt{\chi^2 - 2i}\sin\phi D_2(\chi). \quad (48)$$

Eq. (47) then becomes

$$I_{SDP}(r, \phi) = \sqrt{2}e^{i(k_0 r - \frac{\pi}{4})} \int_{-\infty}^{\infty} \frac{N(\chi)D^*(\chi)e^{-k_0 r \chi^2}}{D(\chi)D^*(\chi)\sqrt{1 + \frac{i\chi^2}{2}}} d\chi, \quad (49)$$

where

$$D(\chi)D^*(\chi) = \sum_{n=1}^{10} b_n (\chi^2)^n.$$

$$N(\chi)D^*(\chi) = A(\chi, \phi) - \chi\sqrt{\chi^2 - 2i}B(\chi, \phi),$$

$$A(\chi, \phi) = A_s(\chi, \phi) + (1 + \frac{i\chi^2}{2})A_r(\chi, \phi),$$

$$A_s(\chi, \phi) = [C_0 \cos \phi (1 + i\chi^2) + C_2 k_0^2 \sin^2 \phi \cos \phi (1 + i\chi^2)^3] \\ \cdot [(F_3 + F_5) + i(q_5 i\chi^{10} + q_4 \chi^8 + q_3 i\chi^6 + q_2 \chi^4 + q_1 i\chi^2 + q_0)],$$

and

$$\begin{aligned}
 A_r(\chi, \phi) = & -2i\chi^2 [C_2 k_0^2 \cos^3 \phi (1 + i\chi^2) - 2C_2 k_0^2 \sin^2 \phi \cos \phi (1 + i\chi^2)] \\
 & \cdot [(F_3 + F_5) + i(q_5 i\chi^{10} + q_4 \chi^8 + q_3 i\chi^6 + q_2 \chi^4 + q_1 i\chi^2 + q_0)] \\
 & + 2\chi^2 \sin \phi [C_0 \sin \phi + C_2 k_0^2 \cos^2 \phi \sin \phi (\chi^4 - 2i\chi^2) \\
 & + C_2 k_0^2 \sin^3 \phi (1 + i\chi^2)^2 - 2C_2 k_0^2 \cos^2 \phi \sin \phi (1 + i\chi^2)^2] \\
 & \cdot [p_4 \chi^8 + p_3 i\chi^6 + p_2 \chi^4 + p_1 i\chi^2 + p_0].
 \end{aligned}$$

It can be shown that, on further examination of Eq. (49), the integral with the term $\chi \sqrt{\chi^2 - 2i} B(\chi, \phi)$ in the numerator vanishes because it has an odd integrand. As can be seen from Eq. (49), the denominator $D(\chi)D^*(\chi)$ is a polynomial in χ^2 and can be expanded into partial fractions with roots χ_n^2 as follows:

$$D(\chi)D^*(\chi) = b_{10}(\phi) \prod_{n=1}^{10} (\chi^2 - \chi_n^2), \text{ where } b_{10}(\phi) = q_5^2 + p_4^2 \sin^2 \phi = 1.$$

Thus, $I_{SDP}(r, \phi)$ can be expressed as

$$\begin{aligned}
 I_{SDP}(r, \phi) = & 2\sqrt{2} e^{i(k_0 r - \frac{\pi}{4})} \sum_{n=1}^{10} [a_n^s \int_0^\infty \frac{e^{-k_0 r \chi^2}}{(\chi^2 - \chi_n^2) \sqrt{1 + \frac{i\chi^2}{2}}} d\chi \\
 & + a_n^r \int_0^\infty \frac{\sqrt{1 + \frac{i\chi^2}{2}} e^{-k_0 r \chi^2}}{\chi^2 - \chi_n^2} d\chi],
 \end{aligned} \tag{50}$$

where

$$a_n^s = \lim_{x \rightarrow \chi_n} \frac{A_s(\chi, \phi)(\chi^2 - \chi_n^2)}{\prod_{j=1}^{10} (\chi^2 - \chi_j^2)}$$

$$a_n^r = \lim_{x \rightarrow \chi_n} \frac{A_r(\chi, \phi)(\chi^2 - \chi_n^2)}{\prod_{j=1}^{10} (\chi^2 - \chi_j^2)}$$

Although the pressure has been expressed as a summation of the ten integrals, the term $\sqrt{1 + \frac{i\chi^2}{2}}$ is still in the integrand and consequently one is not able to

perform the integration in a closed form. To treat these integrals, let $b = -i\chi_n$ and $\mu = \sqrt{k_0 r}$, then the integrals become

$$P_b^s(\mu, \chi) = \int_0^\infty \frac{e^{-\mu^2 \chi^2}}{(x^2 + b^2) \sqrt{1 + \frac{i\chi^2}{2}}} d\chi, \quad (51)$$

and

$$P_b^r(\mu, \chi) = \int_0^\infty \frac{\sqrt{1 + \frac{i\chi^2}{2}} e^{-\mu^2 \chi^2}}{(x^2 + b^2)} d\chi. \quad (52)$$

The square-root term can be expanded into Taylor's series about the saddle point $\chi = 0$, and expressed as

$$\frac{1}{\sqrt{1 + \frac{i\chi^2}{2}}} = 1 + \sum_{k=1}^{\infty} \frac{\frac{-1}{2} \cdot \frac{-3}{2} \cdots (\frac{1}{2} - k)}{k!} \left(\frac{i}{2}\right)^k \chi^{2k}, \quad (53)$$

and

$$\sqrt{1 + \frac{i\chi^2}{2}} = 1 + \sum_{k=1}^{\infty} \frac{\frac{1}{2} \cdot \frac{-1}{2} \cdot \frac{-3}{2} \cdots (\frac{3}{2} - k)}{k!} \left(\frac{i}{2}\right)^k \chi^{2k}. \quad (54)$$

Thus, $P_b^s(\mu, b)$ and $P_b^r(\mu, b)$ can be written as

$$P_b^s(\mu, b) = \int_0^\infty \frac{e^{-\mu^2 b^2}}{x^2 + b^2} d\chi + \sum_{k=1}^{\infty} \frac{\frac{-1}{2} \cdot \frac{-3}{2} \cdot \frac{-5}{2} \cdots (\frac{1}{2} - k)}{k!} \left(\frac{i}{2}\right)^k \int_0^\infty \frac{x^{2k} e^{-\mu^2 b^2}}{x^2 + b^2} d\chi \quad (55)$$

and

$$P_b^r(\mu, b) = \int_0^\infty \frac{e^{-\mu^2 b^2}}{x^2 + b^2} d\chi + \sum_{k=1}^{\infty} \frac{\frac{1}{2} \cdot \frac{-1}{2} \cdot \frac{-3}{2} \cdots (\frac{3}{2} - k)}{k!} \left(\frac{i}{2}\right)^k \int_0^\infty \frac{x^{2k} e^{-\mu^2 b^2}}{x^2 + b^2} d\chi. \quad (56)$$

It can be shown that, by the method of integration by parts, the second integral in Eq. (55) and (56) is equal to

$$\int_0^\infty \frac{x^{2k} e^{-\mu^2 b^2}}{x^2 + b^2} d\chi = (-1)^k b^{2k} \int_0^\infty \frac{e^{-\mu^2 b^2}}{x^2 + b^2} d\chi - \sum_{j=1}^k (-1)^{j+1} b^{2(j-1)} \frac{\Gamma(k-j+\frac{1}{2})}{2\mu^{2(k-j+\frac{1}{2})}}. \quad (57)$$

As can be seen from Eqs. (55–57), only one type of integral is left and of the form [16]

$$\int_0^\infty \frac{e^{-\mu^2 b^2}}{\chi^2 + b^2} d\chi = \frac{\pi}{2b} \operatorname{erfc}(b\mu) e^{\mu^2 b^2} \quad \text{for } \Re\{b\} > 0. \quad (58)$$

Finally, the integral for the radiated acoustic pressure along the steepest descent path becomes

$$\begin{aligned}
I_{SDP}(r, \phi) = & \sqrt{2} e^{i(k_0 r - \frac{\pi}{4})} \\
& \sum_{n=1}^{10} \left\{ \left[(a_n^s + a_n^r) + \sum_{k=1}^{\infty} \frac{\frac{1}{2} \cdot \frac{3}{2} \cdots (k - \frac{1}{2})}{k!} \right. \right. \\
& \quad \left(a_n^s + \frac{-1}{2k-1} a_n^r \right) \left(\frac{-i \chi_n^2}{2} \right)^k \\
& \quad \left. \left(\frac{i\pi}{\chi_n} \right) \operatorname{erfc}(-i \chi_n \sqrt{k_0 r}) \right] e^{-k_0 r \chi_n^2} \\
& + \sum_{m=0}^{\infty} \left[\sum_{j=m}^{\infty} \frac{\frac{1}{2} \cdot \frac{3}{2} \cdots (\frac{1}{2} + j)}{(j+1)!} \right. \\
& \quad \left. \left(a_n^s + \frac{-1}{2j+1} a_n^r \right) \left(\frac{-i}{2} \right)^{j+1} \chi_n^{2(j-m)} \right] \frac{\Gamma(m + \frac{1}{2})}{(k_0 r)^{(m + \frac{1}{2})}} \quad \right\}, \tag{59}
\end{aligned}$$

and the total pressure field can be expressed as

$$p(r, \phi) = \frac{\rho_0 F_0}{2\pi m \Omega^2} \{ I_{SDP}(r, \phi) + 2\pi i \sum \text{res} [\text{between } C(\alpha) \text{ and } SDP] \}, \quad (60)$$

where the residue contributions are given by Eq. (43).

Instead of calculating the complementary error function in Eq. (59), the computer algorithm takes advantage of expanding the w -function into an asymptotic series. The following two equations [16] have been used:

$$w(z) = e^{-z^2} \operatorname{erfc}(-iz) = \sum_{n=0}^{\infty} \frac{(iz)^n}{\Gamma(\frac{n}{2} + 1)}, \text{ for all } z, \quad (61)$$

and

$$w(iz) = e^{z^2} \operatorname{erfc}(z) = \frac{1}{\sqrt{\pi}} \frac{1}{z + \frac{1}{z + \frac{1}{z + \frac{1}{z + \dots}}}}, \text{ for } \Re\{z\} > 0. \quad (62)$$

For an argument of the w -function greater than 1.0, continued fraction representation, Eq. (62), is used while the Taylor's series expansion, Eq. (61), is used for the argument less than 1.0. Thus, if the argument of the w -function is of the value near 1.0, then the series converges very slowly. Consequently, many more terms have to be considered in order to obtain a better solution. It should be noted that, in general, this uniformly asymptotic solution obtained from the modified steepest descent method runs much less computer CPU time than that for the numerical integration to be discussed later.

For the farfield solution, Eq. (59) can be simplified to a more compact form. The asymptotic expansion for the w -function with a large argument can be expressed as

$$w(z) \approx \frac{1}{\sqrt{\pi}z} [1 + \sum_{m=1}^{\infty} (-1)^m \frac{1 \cdot 3 \cdot 5 \cdots (2m-1)}{(2z^2)^m}], \text{ for } z \rightarrow \infty. \quad (63)$$

Thus, Eq. (59) becomes

$$I_{SDP}(r, \phi) = -\sqrt{2} e^{i(k_0 r - \frac{\pi}{4})} \sum_{n=1}^{10} \left\{ \sum_{m=0}^{\infty} \left[\frac{a_n^s + a_n^r}{\chi_n^{2(m+1)}} + \sum_{k=1}^m \frac{1 \cdot 3 \cdot 5 \cdots (2k-1)}{k!} (-i)^k \frac{a_n^s - \frac{a_n^r}{2k-1}}{\chi_n^{2(m-k+1)}} \right] \frac{\Gamma(m + \frac{1}{2})}{(k_0 r)^{m+\frac{1}{2}}} \right\}. \quad (64)$$

For large $k_0 r$, the solution can be obtained by keeping only the leading term ($m = 0$) and expressed as

$$p_{SDP}(r, \phi) = \frac{\rho_0 F_0}{2\pi m \Omega^2} \sqrt{\frac{2\pi}{k_0 r}} e^{i(k_0 r - \frac{\pi}{4})} \sum_{n=1}^{10} \frac{a_n^s + a_n^r}{(\chi^2 - \chi_n^2)|_{\chi=0}}. \quad (65)$$

It can be shown that Eq. (65) is essentially an alternate version of the pressure field contributed at the saddle point, $\chi = 0$.

3.3 Numerical Integration

The numerical integration method is discussed in this section and the results are compared with those obtained from the previous two methods. It can be

seen from Eq. (15) that the numerical integration in the complex K -plane is very complicated due to the branch cuts. However, one can alternately perform the numerical integration along the steepest descent path without loss of accuracy.

As discussed in the modified steepest descent method, with the transformation $\chi^2 = -i[\cos(\alpha - \phi) - 1]$, the steepest descent path is then transformed to the real axis of the complex χ -plane. The integrand is given in Eq. (49). Since the SDP has the characteristics that the phases are stationary, the integrand now becomes an exponentially-decaying, non-oscillating function.

It should be noted that the computer CPU time for the integration along the steepest descent path is much less than that needed in the complex K -plane which requires integrations on the branch cuts.

CHAPTER 4

SOLUTION FOR POINT FORCE EXCITATION

4.1 Standard Steepest Descent Method

The integral, as shown in Eq. (29), can be evaluated asymptotically by the saddle point integration. The asymptotic representation of Hankel function is given by

$$H_0^{(1)}(z) \approx \sqrt{\frac{2}{\pi z}} e^{i(z-\pi/4)} \left[1 + \frac{1}{8iz} + \frac{9}{128(iz)^2} + \dots \right]. \quad (66)$$

For the farfield solution, taking only the leading in Eq. (66) and substituting into Eq. (29) results in the following equation which is ready for standard steepest descent method:

$$p(R, \phi) = \frac{\rho_0 F_0}{4\pi m \Omega^2} \sqrt{\frac{2}{\pi k_0 R \sin \phi}} e^{-i\pi/4} \cdot \int_{C(\alpha)} \frac{(C_1 + C_3 k_0^2 \sin^2 \alpha) k_0 \sin \alpha \cos \alpha e^{i k_0 R \cos(\alpha - \phi)}}{[(F_5 + F_3 \sin^2 \alpha) + i \cos \alpha (\sin^4 \alpha - F_1 \sin^2 \alpha + F_2)] \sqrt{\sin \phi}} d\alpha, \quad (67)$$

where $R^2 = r^2 + z^2$. As was done in the line force excitation, the saddle point is found mathematically equal to the observation angle. The first order approximation to the integral in Eq. (67) can be obtained as

$$ISDP \approx \sqrt{\frac{2\pi}{k_0 R}} e^{i(k_0 R - \frac{\pi}{4})} F(\phi), \quad (40)$$

where

$$F(\phi) = \frac{(C_1 + C_3 k_0^2 \sin^2 \phi) k_0 \sin \phi \cos \phi}{[(F_5 + F_3 \sin^2 \phi) + i \cos \phi (\sin^4 \phi - F_1 \sin^2 \phi + F_2)] \sqrt{\sin \phi}}. \quad (68)$$

Thus, the total pressure field becomes

$$p(R, \phi) = \frac{\rho_0 F_0}{4\pi m \Omega^2} \left\{ \frac{-2ie^{ik_0 R}}{k_0 R \sin \phi} \frac{(C_1 + C_3 k_0^2 \sin^2 \phi) k_0 \sin \phi \cos \phi}{(F_5 + F_3 \sin^2 \phi) + i \cos \phi (\sin^4 \phi - F_1 \sin^2 \phi + F_2)} \right. \\ \left. + 2\pi i \sum \text{residues of poles between SDP and } C(\alpha) \right\}, \quad (69)$$

where

$$res(\alpha_j) = \frac{\bar{N}(\alpha)e^{ik_0 R \cos\phi \cos\alpha}}{2F_3 \sin\alpha \cos\alpha + i\bar{D}(\alpha)}|_{\alpha=\alpha_j}, \quad (70)$$

$$\bar{N}(\alpha) = k_0 \sin\alpha \cos\alpha (C_1 + C_3 k_0^2 \sin^2\alpha) H_0^{(1)}(k_0 R \sin\phi \sin\alpha),$$

and $\bar{D}(\alpha)$ is shown in Eq. (43).

4.2 Modified Steepest Descent Method

The integral along the steepest descent path in complex α -plane can be expressed as

$$I_{SDP} = \int_{SDP} \frac{(C_1 + C_3 k_0^2 \sin^2\alpha) H_0^{(1)}(k_0 R \sin\phi \sin\alpha) k_0 \sin\alpha \cos\alpha e^{ik_0 R \cos\phi \cos\alpha}}{(F_5 + F_3 \sin^2\alpha) + i\cos\alpha (\sin^4\alpha - F_1 \sin^2\alpha + F_2)} d\alpha. \quad (71)$$

To proceed with the solution, it is convenient to use the integral representation of the Hankel function given as

$$H_0^{(1)}(z) = \frac{4}{\pi} e^{iz} \int_0^\infty \frac{e^{-y^2/2}}{\sqrt{4iz - y^2}} dy. \quad (72)$$

Thus,

$$I_{SDP} = \int_{SDP} \frac{(C_1 + C_3 k_0^2 \sin^2\alpha) k_0 \sin\alpha \cos\alpha e^{ik_0 R \cos(\alpha-\phi)}}{(F_5 + F_3 \sin^2\alpha) + i\cos\alpha (\sin^4\alpha - F_1 \sin^2\alpha + F_2)} \cdot \int_0^\infty \frac{e^{-\frac{y^2}{2}}}{\sqrt{4iu - y^2}} dy d\alpha, \quad (73)$$

where $u = k_0 R \sin\phi \sin\alpha$. Substituting the transformation and the identities, Eqs. (34) and (46), into Eq. (73) results in

$$I_{SDP} = \frac{4\sqrt{2}}{\pi} e^{i(k_0 R - \pi/4)} \int_{-\infty}^\infty \frac{N(\chi) e^{-k_0 R \chi^2}}{D(\chi) \sqrt{1 - \frac{i\chi^2}{2}}} \int_0^\infty \frac{e^{-k_0 R y^2}}{g(\chi, y)} dy d\chi, \quad (74)$$

where

$$\begin{aligned}
 g(\chi, y) &= \sqrt{2i\sin\phi|\chi\sqrt{\chi^2 - 2i\cos\phi + (1 + i\chi^2)\sin\phi|} - y^2}, \\
 N(\chi) &= N_1(\chi) + \chi\sqrt{\chi^2 - 2i}N_2(\chi), \\
 N_1(\chi) &= n_4\chi^8 + n_3i\chi^6 + n_2\chi^4 + n_1i\chi^2 + n_0, \\
 N_2(\chi) &= m_3i\chi^6 + m_2\chi^4 + m_1i\chi^2 + m_0, \\
 n_4 &= 4C_3k_0^3\sin\phi\cos\phi(\sin^2\phi - \cos^2\phi), \\
 n_3 &= 16C_3k_0^3\sin\phi\cos\phi(\cos^2\phi - \sin^2\phi), \\
 n_2 &= \sin\phi\cos\phi[C_3k_0^3(19\cos^2\phi - 21\sin^2\phi) - 2C_1k_0], \\
 n_1 &= \sin\phi\cos\phi[C_3k_0^3(10\sin^2\phi - 6\cos^2\phi) + 4C_1k_0], \\
 n_0 &= \sin\phi\cos\phi(C_3k_0^3\sin^2\phi + C_1k_0), \\
 m_3 &= C_3k_0^3(\cos^4\phi - 6\cos^2\phi\sin^2\phi + \sin^4\phi), \\
 m_2 &= C_3k_0^3(3\cos^4\phi - 18\cos^2\phi\sin^2\phi + 3\sin^4\phi), \\
 m_1 &= C_3k_0^3(-2\cos^4\phi + 15\cos^2\phi\sin^2\phi - 3\sin^4\phi) + C_1k_0(\cos^2\phi - \sin^2\phi), \\
 m_0 &= C_3k_0^3(3\cos^2\phi\sin^2\phi - \sin^4\phi) + C_1k_0(\cos^2\phi - \sin^2\phi),
 \end{aligned}$$

and $D(\chi)$ is given in Eq. (47).

Again, to eliminate the square-root term in the denominator, it is necessary to multiply both the numerator and the denominator by $D^*(\chi)$ given in Eq. (48). Thus,

$$N(\chi)D^*(\chi) = A_s(\chi, \phi) + (1 + \frac{i\chi^2}{2})A_r(\chi, \phi) + \sqrt{2}e^{-i\pi/4}\sqrt{1 + \frac{i\chi^2}{2}}\chi A_t(\chi, \phi), \quad (75)$$

where

$$\begin{aligned}
 A_s(\chi, \phi) &= [C_1k_0\cos\phi\sin\phi(1 + i\chi^2)^2 + C_3k_0^3\sin^3\phi\cos\phi(1 + i\chi^2)^4] \\
 &\cdot [(F_3 + F_5) + i(q_5i\chi^{10} + q_4\chi^8 + q_3i\chi^6 + q_2\chi^4 + q_1i\chi^2 + q_0)],
 \end{aligned}$$

and

$$\begin{aligned}
 A_r(\chi, \phi) = & -2i\chi^2 \{-C_1 k_0 \sin\phi \cos\phi \\
 & + C_3 k_0^3 [3(\sin\phi \cos^3\phi - \sin^3\phi \cos\phi)(1+i\chi^2)^2 - \sin\phi \cos^3\phi \chi^2 (\chi^2 - 2i)]\} \\
 & \cdot [(F_3 + F_5) + i(q_5 i\chi^{10} + q_4 \chi^8 + q_3 i\chi^6 + q_2 \chi^4 + q_1 i\chi^2 + q_0)] \\
 & - 2\chi^2 \sin\phi \{C_1 k_0 (\cos^2\phi - \sin^2\phi)(1+i\chi^2) \\
 & + C_3 k_0^3 [(3\sin^2\phi \cos^2\phi - \sin^4\phi)(1+i\chi^2)^3 \\
 & + (\cos^4\phi - 3\sin^2\phi \cos^2\phi)(1+i\chi^2)\chi^2 (\chi^2 - 2i)]\} \\
 & \cdot [p_4 \chi^8 + p_3 i\chi^6 + p_2 \chi^4 + p_1 i\chi^2 + p_0],
 \end{aligned}$$

and

$$\begin{aligned}
 A_t(\chi, \phi) = & [C_1 k_0 (\cos^2\phi - \sin^2\phi)(1+i\chi^2) \\
 & + C_3 k_0^3 (3\sin^2\phi \cos^2\phi - \sin^4\phi)(1+i\chi^2)^3 \\
 & + C_3 k_0^3 (\cos^4\phi - 3\sin^2\phi \cos^2\phi)(1+i\chi^2)\chi^2 (\chi^2 - 2i)] \\
 & \cdot [(F_3 + F_5) + i(q_5 i\chi^{10} + q_4 \chi^8 + q_3 i\chi^6 + q_2 \chi^4 + q_1 i\chi^2 + q_0)] \\
 & + C_3 k_0^3 [3(\sin\phi \cos^3\phi - \sin^3\phi \cos\phi)(1+i\chi^2)^2 - \sin\phi \cos^3\phi \chi^2 (\chi^2 - 2i)] \\
 & \cdot [(F_3 + F_5) + i(q_5 i\chi^{10} + q_4 \chi^8 + q_3 i\chi^6 + q_2 \chi^4 + q_1 i\chi^2 + q_0)] \\
 & + \{C_1 k_0 \sin\phi \cos\phi [(1+i\chi^2)^2 - \chi^2 (\chi^2 - 2i)] \\
 & + C_3 k_0^3 (3\sin\phi \cos^3\phi - 3\sin^3\phi \cos\phi)(1+i\chi^2)^2 \chi^2 (\chi^2 - 2i) \\
 & + C_3 k_0^3 \sin^3\phi \cos\phi (1+i\chi^2)^4 - C_3 k_0^3 \sin\phi \cos^3\phi \chi^4 (\chi^2 - 2i)^2\} \\
 & \cdot [-i\sin\phi (p_4 \chi^8 + p_3 i\chi^6 + p_2 \chi^4 + p_1 i\chi^2 + p_0)].
 \end{aligned}$$

The pressure integral along the SDP becomes

$$p_{SDP}(R, \phi) = \frac{\sqrt{2} F_0 \rho_0}{\pi^2 m \Omega^2} e^{i(k_0 R - \frac{\pi}{4})} (p_1 + p_2 + p_3), \quad (76)$$

where

$$p_1 = \sum_{n=1}^{10} a_n^3 \int_{-\infty}^{\infty} \frac{e^{-k_0 R \chi^2}}{(\chi^2 - \chi_n^2)} \int_0^{\infty} \frac{e^{-k_0 R y^2}}{g(\chi, y) \sqrt{1 + \frac{i\chi^2}{2}}} dy d\chi, \quad (77)$$

and

$$a_n^s = \lim_{x \rightarrow x_n} \frac{A_s(\chi, \phi)(\chi^2 - \chi_n^2)}{\prod_{j=1}^{10} (\chi^2 - \chi_j^2)}.$$

Similarly, p_2 and p_3 are expressed as

$$p_2 = \sum_{n=1}^{10} a_n^r \int_{-\infty}^{\infty} \frac{e^{-k_n R \chi^2}}{(\chi^2 - \chi_n^2)} \int_0^{\infty} \frac{\sqrt{1 + \frac{1}{2} \chi^2} e^{-k_n R y^2}}{g(\chi, y)} dy d\chi, \quad (78)$$

$$p_3 = \sqrt{2} e^{-i\pi/4} \sum_{n=1}^{10} a_n^t \int_{-\infty}^{\infty} \frac{e^{-k_n R \chi^2}}{(\chi^2 - \chi_n^2)} \int_0^{\infty} \frac{\chi e^{-k_n R y^2}}{g(\chi, y)} dy d\chi, \quad (79)$$

where

$$a_n^r = \lim_{x \rightarrow x_n} \frac{A_r(\chi, \phi)(\chi^2 - \chi_n^2)}{\prod_{j=1}^{10} (\chi^2 - \chi_j^2)},$$

$$a_n^t = \lim_{x \rightarrow x_n} \frac{A_t(\chi, \phi)(\chi^2 - \chi_n^2)}{\prod_{j=1}^{10} (\chi^2 - \chi_j^2)}.$$

By expanding the second integrand, but not the exponential term, in Eqs. (77-79) into Taylor's series in χ and y about $(0, 0)$, the integral with odd power term in χ will vanish because of its odd integrand. Thus,

$$p_1 = -\sqrt{2} e^{-i\frac{\pi}{4}} \sum_{n=1}^{10} a_n^s \int_{-\infty}^{\infty} \frac{e^{-k_n R \chi^2}}{\chi^2 - \chi_n^2} \left[\sum_{k=0}^{\infty} \sum_{l=0}^{\infty} f_{kl} \int_0^{\infty} \chi^{2k} y^{2l} e^{-k_n R y^2} dy \right] d\chi, \quad (80)$$

$$p_2 = -\sqrt{2} e^{-i\frac{\pi}{4}} \sum_{n=1}^{10} a_n^r \int_{-\infty}^{\infty} \frac{e^{-k_n R \chi^2}}{\chi^2 - \chi_n^2} \left[\sum_{k=0}^{\infty} \sum_{l=0}^{\infty} g_{kl} \int_0^{\infty} \chi^{2k} y^{2l} e^{-k_n R y^2} dy \right] d\chi, \quad (81)$$

and

$$p_3 = -\sqrt{2} e^{-i\frac{\pi}{4}} \sum_{n=1}^{10} a_n^t \int_{-\infty}^{\infty} \frac{e^{-k_n R \chi^2}}{\chi^2 - \chi_n^2} \left[\sum_{k=0}^{\infty} \sum_{l=0}^{\infty} h_{kl} \int_0^{\infty} \chi^{2k} y^{2l} e^{-k_n R y^2} dy \right] d\chi, \quad (82)$$

where f_{kl} , g_{kl} and h_{kl} are the Taylor's series coefficients, as listed in Appendix A.

The following two equations are used to perform the integrals:

$$\int_0^{\infty} \chi^m e^{-a\chi^2} d\chi = \frac{\Gamma(\frac{m+1}{2})}{2a^{(\frac{m+1}{2})}}, \quad (83)$$

and

$$\int_0^\infty \frac{e^{-\mu^2 b^2}}{\chi^2 + b^2} d\chi = \frac{\pi}{2b} \operatorname{erfc}(b\mu) e^{\mu^2 b^2} \quad \text{for } \Re\{b\} > 0. \quad (58)$$

Summing Eqs. (80) and (81) for the $k = 0$ terms results in

$$\begin{aligned} p_0 = & \sum_{n=1}^{10} (a_n^s + a_n^r) \frac{\sqrt{2\pi} e^{-i\pi/4}}{4 \sin \phi \sqrt{k_0 R}} \\ & \cdot \frac{i\pi}{\chi_n} \operatorname{erfc}(-i\chi_n \sqrt{k_0 R}) e^{-k_0 R \chi_n^2} \\ & \cdot [1 + \frac{1}{8ik_0 R \sin^2 \phi} + \frac{9}{128(ik_0 R \sin^2 \phi)^2} + \frac{75}{1024(ik_0 R \sin^2 \phi)^3} + \dots]. \end{aligned}$$

By using the asymptotic expansion of Hankel function given in Eq. (66), p_0 is then of the form

$$\begin{aligned} p_0 = & \sum_{n=1}^{10} (a_n^s + a_n^r) \frac{\pi e^{-ik_0 R \sin^2 \phi}}{4} \\ & \cdot H_0^{(1)}(k_0 R \sin^2 \phi) \left(\frac{i\pi}{\chi_n}\right) \operatorname{erfc}(-i\chi_n \sqrt{k_0 R}) e^{-k_0 R \chi_n^2}. \end{aligned} \quad (84)$$

For integers $k \geq 1$, substituting Eqs. (57), (58) and (83) into Eq. (80), then p_1 can be expressed as:

$$\begin{aligned} p_1 = & \frac{-e^{-i\pi/4}}{\sqrt{2}} \sum_{n=1}^{10} a_n^s \left\{ \sum_{k=1}^{\infty} \left[\sum_{l=0}^{\infty} f_{kl} \frac{\Gamma(l + \frac{1}{2})}{(k_0 R)^{l+\frac{1}{2}}} \right] \chi_n^{2k} \right. \\ & \cdot \left(\frac{i\pi}{\chi_n} \right) \operatorname{erfc}(-i\chi_n \sqrt{k_0 R}) e^{-k_0 R \chi_n^2} \\ & + \sum_{m=0}^{\infty} \left[\sum_{j=m}^{\infty} \chi_n^{2(j-m)} \left(\sum_{l=0}^{\infty} f_{(j+1)l} \frac{\Gamma(l + \frac{1}{2})}{(k_0 R)^{l+\frac{1}{2}}} \right) \right] \frac{\Gamma(m + \frac{1}{2})}{(k_0 R)^{m+\frac{1}{2}}} \}. \end{aligned} \quad (85)$$

Similarly, p_2 and p_3 can be obtained and the total pressure field is expressed as:

$$\begin{aligned}
 p(R, \phi) = & \frac{\sqrt{2}\rho_0 F_0}{\pi^2 m \Omega^2} e^{i(k_0 R - \frac{\pi}{4})} \\
 & \sum_{n=1}^{10} \{ [(a_n^s + a_n^r) \frac{\pi e^{-ik_0 R \sin^2 \phi}}{4} H_0^{(1)}(k_0 R \sin^2 \phi) \\
 & + (\frac{-e^{-i\frac{\pi}{4}}}{\sqrt{2}}) \sum_{k=1}^{\infty} (\sum_{l=0}^{\infty} (a_n^s f_{kl} + a_n^r g_{kl} + a_n^t h_{kl}) \frac{\Gamma(l + \frac{1}{2})}{(k_0 R)^{l+\frac{1}{2}}}) \chi_n^{2k_1} \\
 & \cdot (\frac{i\pi}{\chi_n}) \operatorname{erfc}(-i\chi_n \sqrt{k_0 R}) e^{-k_0 R \chi_n^2} \\
 & + (\frac{-e^{-i\frac{\pi}{4}}}{\sqrt{2}}) \sum_{m=0}^{\infty} [\sum_{j=m}^{\infty} (\sum_{l=0}^{\infty} (a_n^s f_{(j+1)l} + a_n^r g_{(j+1)l} + a_n^t h_{(j+1)l}) \\
 & \frac{\Gamma(l + \frac{1}{2})}{(k_0 R)^{l+\frac{1}{2}}}) \chi_n^{2(j-m)}] \frac{\Gamma(m + \frac{1}{2})}{(k_0 R)^{m+\frac{1}{2}}} \} \\
 & + (\frac{\rho_0 F_0}{4\pi m \Omega^2}) 2\pi i \sum \text{res (between } C(\alpha) \text{ and SDP } \text{).}
 \end{aligned} \tag{86}$$

By substituting the asymptotic expression for w -function, given in Eq. (63), into Eq. (86), it can be shown that the two asymptotic series cancel out each other and the farfield solution becomes

$$\begin{aligned}
 p_{SDP}(R, \phi) = & \frac{\sqrt{2}\rho_0 F_0}{\pi^2 m \Omega^2} e^{i(k_0 R - \frac{\pi}{4})} \\
 & \sum_{n=1}^{10} \{ (a_n^s + a_n^r) \frac{\pi e^{-ik_0 R \sin^2 \phi}}{4} H_0^{(1)}(k_0 R \sin^2 \phi) \\
 & (\frac{i\sqrt{\pi}}{-i\chi_n^2 \sqrt{k_0 R}}) [1 + \sum_{m=1}^{\infty} \frac{1 \cdot 3 \cdot 5 \cdots (2m-1)}{(2k_0 R \chi_n^2)^m}] \}.
 \end{aligned} \tag{87}$$

For very large $k_0 R$, replacing the Hankel function by its asymptotic form and taking only the leading term into account, Eq. (87) is simplified to the saddle point contribution and expressed as

$$p_{SDP}(R, \phi) = \frac{\rho_0 F_0}{2\pi m \Omega^2} \frac{-ie^{ik_0 R}}{k_0 R \sin \phi} \sum_{n=1}^{10} \frac{a_n^s + a_n^r}{(\chi_n^2 - \chi_n^2)_{s=0}}. \tag{88}$$

To obtain an exact solution for an observation point at the direction normal to the plate, one may have to start with the integral representation of the pressure field which contains the Bessel function. Thus,

$$p_{SDP}(R, \phi) = \frac{\sqrt{2}\rho_0 F_0 e^{-i\pi/4}}{2\pi m \Omega^2} \int_0^\infty \frac{N(\chi) D^*(\chi) J_0(u) e^{ik_n R \cos \phi \cos \alpha}}{\prod_{n=1}^{10} (\chi^2 - \chi_n^2) \sqrt{1 + \frac{u^2}{2}}} d\chi, \quad (89)$$

where $u = k_0 R \sin \phi [\cos \phi \chi \sqrt{\chi^2 - 2i} + \sin \phi (1 + i\chi^2)]$.

As the observation angle ϕ approaches zero, $A_r(\chi, \phi)$ and $A_s(\chi, \phi)$ in Eq. (76) will vanish, and Eq. (89) is reduced to

$$p_{SDP}(R, 0) = \frac{-i\rho_0 F_0}{\pi m \Omega^2} e^{ik_n R} \int_0^\infty \frac{\chi A_t(\chi, 0) e^{-k_n R \chi^2}}{\prod_{n=1}^{10} (\chi^2 - \chi_n^2)} d\chi. \quad (90)$$

From the transformation in Eq. (45), it can be seen that the ten simple poles χ_n^2 are now reduced to five poles of second order when $\phi = 0^\circ$. Thus, the partial fractions for the integrand becomes:

$$\frac{A_t(\chi, 0)}{\prod_{n=1}^5 (\chi^2 - \chi_n^2)^2} = \sum_{k=1}^5 \left[\frac{a_k}{\chi^2 - \chi_k^2} + \frac{b_k}{(\chi^2 - \chi_k^2)^2} \right], \quad (91)$$

where

$$a_k = \frac{A'_t(\chi_k^2) \cdot b_k w'_k(\chi_k^2)}{w_k(\chi_k^2)},$$

$$b_k = \frac{A_t(\chi_k^2)}{w_k(\chi_k^2)},$$

and

$$w_k(\chi^2) = \frac{\prod_{n=1}^5 (\chi^2 - \chi_n^2)}{(\chi^2 - \chi_k^2)}.$$

Substituting Eq. (91) into Eq. (90) and changing the integration variable yields

$$p_{SDP}(R, 0) = \frac{-i\rho_0 F_0 e^{ik_n R}}{2\pi m \Omega^2} \sum_{n=1}^5 [a_n \int_0^\infty \frac{e^{-k_n R y}}{y - \chi_n^2} dy + b_n \int_{\infty}^0 \frac{e^{-k_n R y}}{(y - \chi_n^2)^2} dy]. \quad (92)$$

The remaining two integral can be found in [16] and expressed as

$$\int_0^\infty \frac{e^{-k_n R y}}{y - \chi_n^2} dy = -e^{-k_n R \chi_n^2} E_i(k_n R \chi_n^2), \quad (93)$$

and

$$\int_0^\infty \frac{e^{-k_n R y}}{(y - \chi_n^2)^2} dy = k_n R e^{-k_n R \chi_n^2} E_i(k_n R \chi_n^2) - \frac{1}{\chi_n^2}, \quad (94)$$

where E_i is the exponential integral function defined as

$$E_i(z) = \int_{-\infty}^z \frac{e^x}{x} dx. \quad (95)$$

Since there is no pole located between the original integration path and the SDP when the observation angle equals zero, the total pressure can be written as

$$p(R, 0) = \frac{-i\rho_0 F_0 e^{ik_n R}}{2\pi m \Omega^2} \sum_{n=1}^5 [(b_n k_n R - a_n) E_i(k_n R \chi_n^2) e^{-k_n R \chi_n^2} - \frac{b_n}{\chi_n^2}]. \quad (96)$$

For very large $k_n R$, the asymptotic expansion for the exponential integral function is of the form

$$E_i(z) \approx \frac{e^z}{z} \sum_{n=0}^{\infty} \frac{n!}{z^n}, \quad |\arg(-z)| < 3\pi/2. \quad (97)$$

The farfield solution for the radiated pressure at the direction normal to the plate becomes

$$p(R, 0) = \frac{-i\rho_0 F_0 e^{ik_n R}}{2\pi m \Omega^2} \sum_{n=1}^5 \frac{-a_n}{k_n R \chi_n^2}, \quad (98)$$

where a_n is expressed in Eq. (91).

Notice that in order to obtain the numerical results from Eq. (96), it is convenient to calculate the exponential integral function by using the Taylor series for small arguments and the asymptotic series for large arguments. The Taylor series is given as

$$E_i(z) = \gamma + \log(-z) - \sum_{n=1}^{\infty} \frac{z^n}{n! n}. \quad (99)$$

where $\gamma = 0.5772156649 \dots$ is the Euler constant.

4.3 Numerical Integration

There are two ways to perform the numerical integration. One is to use Eq. (71) which contains the double integration and consequently runs considerable computer CPU time. To save the CPU time, Eq. (71) is written as

$$p(R, \phi) = \frac{\sqrt{2\rho_0 F_0}}{4\pi m \Omega^2} e^{i(k_0 R \cos^2 \phi - \pi/4)} \int_{-\infty}^{\infty} \frac{N(\chi) D^*(\chi) H_0^{(1)}(u) e^{-k_0 R (\cos^2 \phi \chi^2 - i \cos \phi \sin \phi \chi \sqrt{\chi^2 - 2z})}}{\prod_{n=1}^{10} (\chi^2 - \chi_n^2) \sqrt{1 + \frac{z}{2}}} d\chi, \quad (100)$$

where u is given in Eq. (89). The Hankel function has a Taylor series expansion

$$H_0^{(1)}(z) = J_0(z) + iY_0(z), \quad (101)$$

where

$$J_0(z) = 1 - \frac{z^2/4}{(1!)^2} + \frac{(z^2/4)^2}{(2!)^2} - \frac{(z^2/4)^3}{(3!)^2} + \dots = \sum_{n=0}^{\infty} \frac{(-z^2/4)^n}{(n!)^2},$$

$$Y_0(z) = \frac{2}{\pi} \left(\log \frac{z}{2} + \gamma \right) J_0(z) - \frac{2}{\pi} \sum_{n=1}^{\infty} \left[\sum_{k=1}^n \frac{1}{k} \right] \frac{(-z^2/4)^n}{(n!)^2},$$

and γ is the Euler constant, and the asymptotic expansion for large arguments

$$H_0^{(1)}(z) \approx \sqrt{\frac{2}{\pi z}} [P(0, z) + iQ(0, z)] e^{i(z - \frac{\pi}{4})}, \quad -\pi < \arg z < 2\pi, \quad (102)$$

where

$$P(0, z) = 1 + \sum_{n=1}^{\infty} \frac{(-1)^n \cdot 1^2 \cdot 3^2 \cdot 5^2 \cdots (4n-3)^2 (4n-1)^2}{(2n)! (8z)^{2n}},$$

and

$$Q(0, z) = \frac{-1}{8z} + \sum_{n=1}^{\infty} \frac{(-1)^{n+1} \cdot 1^2 \cdot 3^2 \cdot 5^2 \cdots (4n-1)^2 (4n+1)^2}{(2n-1)! (8z)^{2n+1}}.$$

It should be noted that computing the Hankel function with either the Taylor or the asymptotic series and then performing the single integration have saved the CPU run time by the order of 2 as compared with those for the double integration.

CHAPTER 5

NUMERICAL RESULTS AND DISCUSSIONS

5.1 Introduction

In this chapter, numerical results are presented for the acoustic radiated pressure obtained by the standard steepest descent method, the modified steepest descent method and by the numerical integration for both line- and point-force excitations. To illustrate the influence of poles, the numerical results of the asymptotic series, the leading term approximation or the numerical integration are compared to the additional contribution due to the poles which lie between the SDP and the original path of integration. Comparison is also made for plate with and without structural damping. Some additional results, such as behavior of integrand along the SDP, surface wave pole contribution, grazing and nearfield pressures, velocity field, and acoustic intensity, are also presented.

5.2 Pole Contribution

For the Timoshenko-Mindlin plate theory, the poles can be found by solving the following equation derived from the denominator of the integrand in Eq. (15):

$$\begin{aligned} \Gamma^5 - \Gamma^3[2 - k_c^2(S + I)] + \Gamma^2 \frac{\rho_0 S k_c}{m\Omega} \\ + \Gamma[1 - k_c^2(S - I) + k_c^4 SI - \frac{1}{\Omega^2}] + \frac{\rho_0}{mk_c\Omega^3}[1 + Sk_c^2\Omega^2(1 - k_c^2I)] = 0, \end{aligned} \quad (103)$$

where $\Gamma^2 = K^2 - 1$ and $K = k/k_0$.

Extensive discussions on the poles have been given by Stuart [17], Crighton [18–19], Pierucci and Graham [20–21], and by Strawderman, Ko and Nuttall [22]. There are ten simple poles, six of them are located in the top Riemann sheet and four in the lower Riemann sheet. The typical locations of poles in the complex Γ - and K -plane were computed numerically and are shown in Fig. 5. The locations of

poles depend on the frequency only and Fig. 6 shows the frequency loci of poles in the complex K -plane. It should be noted that if the plate is lossy, i.e., its Young's modulus is complex-valued, the locations of poles are also dependent upon the loss factor of the plate material.

There are only three poles that could fall between the SDP and the original integration path, as shown in Fig. 4. Two frequencies are of importance, which are for steel plate and water $\Omega_c = 1.23$ and $\Omega_{co} = 6.79$. The pole α_3 , known as the leaky wave pole due to the flexural waves, is included when $\Omega > \Omega_c$. The pole α_4 , which is the leaky wave pole due to the thickness shear mode, is included when $\Omega > \Omega_{co}$. The third one is $-\alpha_0$, which is a surface wave pole, is included because of the addition of small amount of damping.

The poles affect the radiated pressure in two ways. The proximity of a pole to the saddle point generates a peak in the directivity function due to that pole. In the SDP solutions, Eqs. (41) and (68), the denominator is minimized when $\Omega > \Omega_c$ which generates a peak in the directivity function at the coincidence angle $\phi = \phi_c$ and a second peak at $\phi = \phi_{co}$ when the frequency $\Omega > \Omega_{co}$. In the asymptotic series solutions, Eqs. (59) and (86), the complementary error function becomes large when the argument χ_n is of small value. The argument χ_n represents the distance of the pole χ_n from the origin at $\chi = 0$, which represents the saddle point. Similar arguments can be advanced for the numerical integration scheme, Eqs. (50) and (77-79), where the integrand becomes large as the variable of integration χ comes close to one of the poles χ_n . Thus, all three solutions generate one or two peaks in the directivity function when one or two poles approach the saddle point. As mentioned earlier, the pole location depends on the frequency only and the saddle point is located at the observation angle ϕ . Thus, the distance between the pole and the saddle point depends on both the forcing frequency and the observation angle. To examine the distance between the poles $-\alpha_0$, α_3 and α_4 from the saddle point,

the distance $|\alpha_n - \phi|$ is plotted vs. the observer angle ϕ for $\Omega = 1, 5$ and 10 in Figs. 7–9, respectively.

In Fig. 7, $\Omega = 1$ is below the first coincidence frequency Ω_c . α_n 's distance is large for all observer angle. For $\Omega = 5 > \Omega_c$ in Fig. 8, α_3 's distance becomes smallest at $\phi = \phi_c = 39^\circ$, while α_4 and $-\alpha_0$'s distances are large for $0^\circ < \phi < 90^\circ$. At the frequency $\Omega = 10 > \Omega_{co}$, Fig. 9, α_3 's distance is minimal near $\phi_c = 34^\circ$ and α_4 's distance is smallest near $\phi_{co} = 11^\circ$. It should be noted that the higher the frequency, the smaller the distances of α_3 and α_4 are from the saddle point. This means that the peaks in the directivity function become sharper and sharper with increasing frequency. Since the poles α_3 and α_4 have limiting values when $\Omega \rightarrow \infty$, the coincidence angles have high frequency limits $\phi_c \rightarrow 30^\circ$ and $\phi_{co} \rightarrow 17^\circ$ as $\Omega \rightarrow \infty$ for steel plate and water.

The second way a pole influences the radiated pressure is through the residues of the poles located between the SDP and the original integration path. These contributions are the same for all three types of solutions. As can be seen in Eqs. (43) and (70), an exponential decay would occur for a complex-valued α_n . In Eq. (43), the residue decays with the imaginary part of $\cos(\alpha_n - \phi)$. It can also be shown that, by introducing the integral representation of Hankel function expressed in Eq. (72), the residue for point force excitation decays with $Im[\cos(\alpha_n - \phi)]$. To exhibit the decay rates due to the poles, the $Im[\cos(\alpha_n - \phi)]$ is plotted for $n = 0, 3$ and 4 vs. the observer angle ϕ for $\Omega = 1, 5$ and 10 in Figs. 10–12, respectively. If the exponent is small, then the residue contributes significantly to the total acoustic radiated pressure. For $\Omega < 6.79$, only α_3 is seen to have a small exponent near the first coincidence angle ϕ_c , while the exponents for the other two poles, α_0 and α_4 , remain relatively large, see Figs. 10–11. For $\Omega = 6.79$, α_0 still gives a small exponent near the first coincidence angle, but now α_4 also has a small exponent near the second coincidence angle, ϕ_{co} , see Fig. 12. Thus, unless the multiplier of

$Im[\cos(\alpha_n - \phi)]$, $k_0 r$, is very large, the pole may contribute significantly to the total pressure, especially near the two coincidence angles ϕ_c and ϕ_{co} .

5.3 Line Force Excitation

5.3.1 Integral Along the Steepest Descent Path

The integral along the steepest descent path is given in Eq. (49). The integrand has an exponential term $e^{-k_0 r x^2}$ that decays faster with larger value of $k_0 r$. Thus, the integral converges faster the greater the observer distance from the origin and the integrand resembles a Dirac-delta function at the origin $x = 0$ for increasing $k_0 r$. This indicates that the major contribution to the integral results from the region near the origin which corresponds to the saddle point. However, when a pole is located near the saddle point or on the SDP, the integrand will show another peak. Consequently, the presence of these poles requires the use of the modified saddle point method which would account for the significant contributions from the neighborhood of these poles.

Since the location of poles in relation to the saddle point depends on the observation angle and the frequency, one expects these two parameters to influence the rate of decay of the integrand along the SDP. For frequencies below the coincidence, e.g., at $\Omega = 1.0$ and $\phi = 0^\circ$, the decay rate is seen to depend on the value $k_0 r$ in Fig. 13. When a pole comes near the SDP, such as the case when $\Omega = 1$ and $\phi = 60^\circ$ in Fig. 14, one must account for the contribution of the pole to the integral. At the grazing angle $\phi = 90^\circ$, the integrand vanishes at the saddle point, Fig. 15. However, the integral itself does not vanish and thus requiring the evaluation by an asymptotic series instead of the first order SDP approximation. The most important pole is the leaky wave pole α_l which comes closest to the saddle point near the coincidence angle ϕ_c . Thus, the integrand becomes more like a Dirac-delta function at the coincidence angle, as can be observed at $\phi = \phi_c = 34^\circ$ with

$\Omega = 10$ in Fig. 16. When the thickness shear pole α_4 comes close to the saddle point, a similar but sharper peak occurs. Fig. 17 for $\phi = \phi_{co} = 11^\circ$ and $\Omega = 10$.

5.3.2 Influence of Range ($k_0 r$) on the Solution

The uniformly asymptotic series solution, Eq. (59), shows the dependence of the solution in terms of the non-dimensional parameter $k_0 r$. The first part of the solution depends upon the complementary error function of argument $-i\chi_n \sqrt{k_0 r}$ which is not negligible as $\chi_n \sqrt{k_0 r}$ becomes small. However, for $k_0 r$ become large, these terms generate an asymptotic series of $(k_0 r)^{-(m+1/2)}$, which is similar to the second part of the solution. Thus, when $k_0 r$ is not large, the dependence on $k_0 r$ is due to the complementary error function and the second part's $1/\sqrt{k_0 r}$. However, for $k_0 r > 1$ or when χ_n is not small, the leading term of both parts is $1/\sqrt{k_0 r}$.

5.3.3 Radiated Acoustic Pressure

The radiated acoustic pressure was computed by the saddle point method (SPM), Eq. (42), the uniformly asymptotic series solution (UAS), Eq. (60), and by the numerical integration (NI), Eq. (47). The numerical results were obtained for frequencies $\Omega = 1, 5$ and 10 and $k_0 r$ ranges from 10 to 10^5 . In this section, the numerical results and discussions will be focused in three different frequency ranges.

To delete the range dependence of the radiated acoustic pressure, the directivity function (DF) is defined as

$$DF(dB) = 20 \log(p(r, \phi)/p(r, 0^\circ)). \quad (104)$$

5.3.3.1 Frequency Range Below First Coincidence $\Omega_c = 1.23$

In this frequency range, the radiated acoustic pressure has no peak in the directivity function, since the poles are not in the immediate proximity of the saddle point. Figs. 18a and 19a show the directivity functions for $\Omega = 1$ and $k_0 r = 10$ and 100 , respectively. The solutions obtained from the three methods are numerically very close over most angles, and the difference becomes indistinguishable for $k_0 r =$

1000 (not shown). The contributions of the poles are significant only when k_0r is small (nearfield). Furthermore, the surface wave pole $-\alpha_0$ gives non-negligible contributions near grazing angles $\phi = 90^\circ$. Thus the surface pressure due to the solutions without the residues, Figs. 18b and 19b, the SPM solution always vanishes, while the UAS and NI solutions predict non-negligible but small-valued acoustic pressure at $\phi = 90^\circ$. As k_0r increases, the surface pressure decreases even for the UAS and NI solutions, as can be seen from Fig. 19b. In general, the residue contribution to the total pressure seems to be most important near the surface of the plate, as shown in Figs. 18c and 19c for $\Omega = 1$ and $k_0r = 10$ and 100, respectively.

5.3.3.2 Frequency Range $1.23 < \Omega < 6.79$

For frequencies between the first coincidence $\Omega_c = 1.23$ and the second coincidence frequency $\Omega_{co} = 6.79$, there is only one peak occurring at ϕ_c in the directivity pattern. This peak is attributed to the closeness of the leaky wave pole α_3 to the saddle point, and occurs when the trace acoustic wavenumber is equal to the flexural wavenumber. Computations were performed for $\Omega = 5$ and $k_0r = 10$ to 10^4 as shown in Figs. 20–23. For $k_0r = 10$, 100 and $\Omega = 5$, Fig. 20a and 21a, the approximate SPM solutions predict considerably higher acoustic pressures than the more accurate UAS and NI solutions. The differences in the directivity functions between the predicted SPM, UAS and NI solutions narrow down for $k_0r = 10^3$ in Fig. 22, but the SPM solution is markedly different from the other two near the coincidence angle. The differences become negligible for $k_0r = 10^4$, as shown in Fig. 23.

The role played by the residue terms (surface and nearfield effects) are significant when one compares the integral along the SDP in Fig. 20a with the total solution in Fig. 20b. The influence of the poles persists even for $k_0r = 100$, shown in Fig. 21a and 21b, and produces constructive and destructive interference near the

plate surface. The contribution of poles is still significant over the angles range from 40° to 90° , Fig. 22, for $k_0r = 10^3$. It can be seen that, in general, the higher the frequency and the lower the value of k_0r , the more influential the poles' contributions become. Figs. 20c and 21c show the poles' contribution, mainly due to the leaky wave pole α_3 for $\Omega = 5$ and $k_0r = 10$ and 100, respectively.

5.3.3.3 Frequency Range Above Second Coincidence $\Omega_{co} = 6.79$

For frequencies above the second coincidence frequency Ω_{co} , a second peak appears in the directivity function. This particular peak is attributed to the thickness shear pole α_4 being close to the saddle point, i.e., when the acoustic wavenumber is equal to the structural wavenumber of the second branch of the plate frequency spectrum.

Computations were performed for $\Omega = 10$ and $k_0r = 10$ to 10^5 . For low ranges, $k_0r = 10$ and 10^2 in Figs. 24 and 25, the SPM solution generates two peaks while the UAS and NI solutions have none. The coincidence peak near $\phi_c = 34^\circ$ for $k_0r = 10^3$ in Fig. 26 is reasonably modeled by the SPM solution, but the second peak at $\phi_{co} = 11^\circ$ does not appear yet. Again, the pole contributions influence the directivity function throughout the angular range, as seen from the constructive maxima and destructive minima. The three solutions converge at $k_0r = 10^5$, as shown in Fig. 27.

5.3.3.4 Radiated Pressure at $\phi = 0^\circ$

In the previous section, the directivity function is computed in such a way that the pressure at any aspect angle ϕ is normalized by the pressure at $\phi = 0^\circ$. In order that one can obtain the absolute value of the radiated pressure due to the line-force excitation, the radiated pressure at $\phi = 0^\circ$, normalized to $\frac{\rho_0 F_0}{m}$, is plotted in Fig. 28 for $\Omega = 0.5, 1, 5$ and 10 . Thus, the directivity functions in Figs. 18–27 can be corrected by the addition of the radiated pressure at $\phi = 0^\circ$ shown in Fig. 28.

5.3.3.5 Grazing and Nearfield Radiated Pressures

The radiated acoustic pressure at the surface of the plate can be obtained by setting the observer angle ϕ equal to 90° . The first order approximation from the standard steepest descent method vanishes at the plate surface, as can be seen in Eq. (41). This means that the solution depends only on the residues of the poles located between the SDP and the original integration path, Eq. (43). For the asymptotic series solution, the leading term in the series, $m = 0$ in Eq. (59), does not vanish in general and contributes a term of the order $1/\sqrt{k_0 r}$ to the radiated acoustic pressure. However, the leading term tends to be zero at $\phi = 90^\circ$ as $k_0 r$ becomes very large. This means that the remaining terms of the series, $m \geq 1$, contribute a term of the order $(k_0 r)^{-3/2}$ for $k_0 r \gg 1$. Thus, the pole contribution is seen to be very important to the solution of the radiated pressure near and at grazing angles.

5.3.3.5.1 Surface Wave Pole and Surface Pressure

For an observer on the surface of the plate, i.e., at the grazing angle $\phi = 90^\circ$, the surface wave pole $-\alpha_0$ plays an important role. This surface wave pole corresponds to $-K_0$ and is real in the complex wavenumber K -plane. As can be seen from Fig. 6, the pole $-K_0$ is always greater than 1 and it approaches 1 for $\Omega \rightarrow \infty$. This means that $-\alpha_0 = \pi/2 - i\epsilon(\Omega)$, where $\epsilon(\Omega) > 0$ is a real positive number that depends on the frequency only. The pole contribution, expressed in the form of a residue, has an exponential term in its expression

$$\begin{aligned} e^{ik_0 r \cos(\alpha_0, -\phi)} &= e^{ik_0 r \cos(\frac{\pi}{2} - \sigma) \cosh \epsilon} e^{-k_0 r \sin(\frac{\pi}{2} - \sigma) \sinh \epsilon} \Big|_{\phi=90^\circ} \\ &= e^{ik_0 z \cosh \epsilon} e^{-k_0 z \sinh \epsilon}. \end{aligned} \quad (105)$$

Thus, when the observer is at grazing, i.e., at the surface of the plate $\phi = \pi/2$ or $z = 0$, the exponential term in Eq. (105) becomes $e^{ik_0 z \cosh \epsilon}$, which indicates an unattenuated wave traveling along the surface of the plate. Furthermore, the

surface wave pole $-\alpha_0$ is not dependent on the acoustic medium and it seems to be numerically close to the flexural wave propagating-mode pole of a plate without acoustic loading. This fact can be gleaned from the computation of the surface wave pole for both air and water loadings, as shown in Table 1. It can be seen that $K_0(\Omega)$ or $\epsilon(\Omega)$ does not differ much between water and air loadings, despite the fact that the ratio of their characteristic impedances is as high as 3000.

The contribution of the pole $-\alpha_0$ in Eq. (105) clearly shows a surface wave's behavior, i.e., the pressure wave propagates unattenuatedly along the plate surface, $z = 0$, and decays exponentially away from the plate surface at a rate of $k_0 z \sinh \epsilon$. Since the poles α_3 and α_4 are complex-valued at all frequencies, these poles' contributions to the surface pressure generate exponentially decaying terms, as can be seen from the plots of $\text{Im}[\cos(\alpha - \phi)]$ in Fig. 10–12, and become negligible for large $k_0 r$. On the other hand, the pole $-\alpha_0$ generates a propagating, unattenuated wave traveling along the plate surface at all frequencies and becomes dominant for $k_0 r$ large.

To investigate the role played by the poles' contributions, mostly due to the surface wave, and the integral contribution to the total pressure, they were computed separately and plotted for $\Omega = 0.5, 5$, and 10 in Figs. 29–31, respectively. In these figures, one can see that the contribution from the UAS integral in Eq. (59) decays at a rate $(k_0 r)^{-\alpha}$ on the surface, where $k_0 r = k_0 z$. The decaying rate, which depends on the frequency and $k_0 r$, is found to be $0.5 < \alpha < 1.5$, and the upper limit of 1.5 is reached for $k_0 r \gg 1$ and $\Omega \gg 1$. In general, since the integral along the SDP and the contributions of poles α_3 and α_4 decay at some rate with $k_0 r$, the total field would also decay for low $k_0 r$ and then become constant due to the surface wave at some distance $k_0 r$ away from the line force.

5.3.3.5.2 Nearfield Pressure

For observer located away from the surface of the plate, all the three poles generate exponentially decaying contributions, as can be seen in Eq. (105). The rate of exponential decay is a function of the observation angle and ϵ , and the latter is listed in Table 1. As the frequency Ω increases, the decay rate ϵ diminishes, which indicates that the surface wave nearfield extends out farther and farther. However, since k_0 also increase with Ω , the decay rate $k_0 z \sin \epsilon$ reaches a constant limit of $0.05 k_c z$, k_c being the acoustic wavenumber at the coincidence frequency Ω_c .

As mentioned in the previous section, the contribution from the UAS integral decays at a rate $(k_0 r)^{-a}$, "a" being dependent on the frequency Ω and the range $k_0 r$, thus the total nearfield pressure would be dominated by the UAS integral. For low frequency, such as $\Omega = 0.5$, the total pressures at $\phi = 87^\circ$, 88° and 89° are shown in Fig. 32. It can be seen that the integral (UAS) becomes more dominant at closer ranges $k_0 r$ with decreasing observer angle ϕ . Similar behaviors were exhibited at higher frequencies, as shown in Figs. 33 and 34 for $\Omega = 5$ and 10 , respectively.

In order to obtain the radiated acoustic pressure near the surface of the plate, the radiated pressure at a distance 0.01λ away from the plate surface is plotted vs. $k_0 z$ ranging from 10 to 10^3 for $\Omega = 1$ in Fig. 35. Since the pressure is computed below coincidence, the contributions from both the leaky wave pole and the integral along the SDP are relatively small. Thus, the total pressure is due to the surface wave. As the observer moves away from the surface of the plate, the integral along the SDP becomes dominant for $k_0 z$ increases up to 10^2 , as shown in Fig. 36 for $z = \lambda$. For higher $k_0 z$, the integral and the leaky wave decay away and the total pressure could be attributed to the surface wave.

For frequencies above coincidence, the leaky wave pole contributes mostly to the radiated pressure for $k_0 z$ small, while the integral along the SDP and the surface wave are insignificant, as shown in Fig. 37 for $\Omega = 5$ and $z = 0.01\lambda$. However, the

surface wave becomes more important after the integral and the leaky wave decay away for $k_0x > 10^3$. Similar features of the radiated pressure can be observed in Fig. 38 for $\Omega = 5$ and $z = \lambda$.

5.3.3.6 Influence of Structural Damping

The Young's modulus encountered in the computation so far is considered real-valued, i.e., the plate material is purely elastic. In this section, the influence of the added structural damping on the locations of poles and the radiated acoustic pressure will be discussed. The absorption of the elastic energy can be taken into account by using the complex Young's modulus which is related to the real one by the following equation

$$\bar{E} = E(1 - i\eta), \quad (106)$$

where η is the plate material loss factor and $0.0 \leq \eta \leq 1.0$ for nearly all materials of interest. For small amount of damping, the sound speed is corrected by multiplying the sound speed by $(1 - i\eta)^{1/2} \approx (1 - \frac{1}{2}i\eta)$, and hence the coincidence frequency in Eq. (17) becomes $\omega_c(1 + \frac{1}{2}i\eta)$.

Taking into account the dissipation of elastic energy by introducing a complex-valued Young's modulus usually causes all the poles α_n to rotate clockwise in the complex wavenumber plane. It should be noted that the leaky wave poles are defined as those located on the bottom Riemann sheet of the complex K -plane and must appear near the saddle point at some frequencies. For given plate properties and dimensions, the leaky wave pole's distance from the real axis is a function of frequency and is dependent on the plate's absorption of the vibrational energy, i.e., on the magnitude of the loss factor.

Below coincidence, since the energy radiated into the surrounding medium is due only to the line force, the radiated acoustic pressure, shown in Fig. 39 for $k_{ur} = 10$ and $\Omega = 0.5$, displays no significant dependence on the structural damping in the

whole field. In the high-frequency range above coincidence, the radiation pattern is significantly affected by structural damping because, in addition to the external force, the whole plate also radiates energy. As can be seen in Fig. 40a for $\Omega = 5.0$ and $k_0r = 10^2$, the nearfield pressure attributed to the leaky wave pole is remarkably reduced, while the influence on the integral along the SDP near the coincidence angle is relatively small, as shown in Fig. 40b. The influence of structural damping on residue contributions and the integral along the SDP can be explained from Eqs. (42) and (59). For small k_0r , the w -function in Eq. (59) is evaluated by the power series expansion, Eq. (61), and has the approximate numerical value of 1. Thus, the contribution due to the integral is mostly proportional to $1/\chi_n$. Consequently, the influence of structural damping is not significant because of the slight change in χ_n . On the other hand, slight change of the pole's distance from the saddle point would result in a faster-decaying wave since the residue, Eq. (43), contains an exponential term $e^{-k_0rx^2}$.

For farfield pressure, $k_0r = 10^5$ at $\Omega = 5$, the contribution from the leaky wave pole becomes insignificant and the only influence of damping on the integral along SDP appears near the coincidence angle, as shown in Fig. 41. The radiated pressure is significantly reduced due to the fact that certain amounts of the plate's vibrational energy is dissipated through the damping mechanism. Similar phenomena can be observed at higher frequencies in Figs. 42 and 43 for $\Omega = 10$ and $k_0r = 10^2$ and 10^5 , respectively.

At grazing angle, the surface wave pole, K_n , is no longer located on the real axis and shifted away from the real axis in the K -wavenumber plane because of the added damping. Thus, the surface wave generates a decaying term, see Figs. 44 and 45. Figs. 46–47 show the influences of different amount of damping on the grazing field for $\Omega = 0.5$ and 5.0, respectively.

5.4 Point Force Excitation

5.4.1 Integral Along the Steepest Descent Path

For point force excitation, the pressure integral along the SDP is given in Eq. (100). The integrand also contains an exponential-decaying term $e^{-k_0 R \chi^2}$. Thus, as $k_0 R$ increases, the integral converges faster and resembles a Dirac-delta function at the origin $\chi = 0$ which corresponds to the saddle point. Since the numerator of the integrand consists of both even and odd functions in χ , and only the even part will contribute to the pressure integral, the integrand is evaluated as one half of the sum of the integrand with both χ and $-\chi$. As can be seen in Figs. 48–52, the same features as for the line force excitation are observed when the leaky wave pole appears near the saddle point. The notches that appear in these figures are due to the Hankel function's local minima.

5.4.2 Radiated Acoustic Pressure

The expression for radiated acoustic pressure for point force excitation, Eq. (86), is similar to Eq. (59), which is for line force excitation. Thus, most of discussions which are same for line force excitation will not be given in this section, but can be referred in detail in chapter 5.3. Since the results have shown that the directivity functions are exactly same as those for line force excitation, thus only the pressure at $\phi = 0^\circ$ is needed and shown in Fig. 53. The directivity functions shown in Figs. 18–27 can then be corrected by Fig. 53 to obtain the radiated acoustic pressure. It is observed that the decay rate for the radiated pressure at $\phi = 0^\circ$ is $(k_0 R)^{-2}$.

5.4.3 Grazing and Nearfield Radiated Pressure

At the surface of the plate, $\phi = 90^\circ$ and $k_0 R = k_{0r}$, the residue of the surface wave pole $-\alpha_0 = \pi/2 - i\epsilon(\Omega)$ contains a Hankel function as follows:

$$H_0^{(1)}[k_0 R \sin(-\alpha_0)] = H_0^{(1)}(k_0 R \cosh \epsilon). \quad (106)$$

where $\epsilon > 0$ is dependent on the frequency only. The poles' contributions and the integral contribution to the total pressure at the grazing angle are shown in Figs. 54–56 for $\Omega = 0.5, 5$ and 10 , respectively. As can be seen from these figures, the contribution from the integral along the SDP decays at a rate $(k_0 R)^{-2}$, and "a" is found to be $1.0 < a < 2.0$, and the upper limit is reached for $k_0 R \rightarrow 1$ and $\Omega \gg 1$. It should be noted that the radiated pressure due to the surface wave is no longer constant near the surface of the plate as was seen in Figs. 29–31 for line force excitation, but decays at a rate $(k_0 R)^{-1/2}$. Figs. 57–62 show the nearfield radiated pressures for $\Omega = 1, 5, 10$ and $z = 0.01\lambda$ and λ , respectively. Similar discussions, except for the decay rates of UAS integral and the surface wave, have been given in chapter 5.3 for line force excitation.

CHAPTER 6

CONCLUDING REMARKS

6.1 Summary and Conclusion

A new solution to the acoustic radiation from an infinite fluid-loaded, elastic plate excited by a line or a point force has been obtained, for the first time, in the form of a uniformly asymptotic series. It was shown that the uniformly asymptotic series solutions, derived from the modified steepest descent method, indicate clearly that the first order approximation obtained previously by other researchers using the standard saddle point method overpredicts the acoustic pressure in the nearfield. Furthermore, it was shown that the error in predicting the acoustic pressure using the saddle point method is especially pronounced at the coincidence and grazing angles when compared to that due to the uniformly asymptotic series.

It was also shown that, rather than performing the original integral with branch cuts, the transformed integration along the steepest descent path (SDP) is more efficient numerically. The excellent agreement between the two solutions, the uniformly asymptotic series solution and the numerical integration performed along the SDP, validates the use of the modified saddle point method for predicting the acoustic pressure in the nearfield and near the grazing angle. However, the widely used standard saddle point method agrees with the other two solutions only in the distant farfield (e.g., $k_0 r > 10^4$ for $\Omega = 5.0$).

The radiated nearfield acoustic pressure was accurately derived in this study and was shown to be dominated by the UAS (integral along the SDP) only, which decays at the rate $(k_0 r)^{-a}$, where "a" ranges from 0.5 to 1.5 for line force excitation, depending on the range $k_0 r$ and the frequency Ω . The surface pressure was shown

to be dominated by the surface wave pole, which represents a free flexural wave propagating along the surface of the plate without fluid loading.

The influence of the structural damping on the acoustic radiation has also been investigated. In general, below coincidence, where the radiated pressure is primarily due to the nearfield of the external force, the added damping has negligible effect. For frequencies above coincidence, the radiated pressure is significantly affected by the structural damping since the plate as well as the region near the external force radiate energy. In the nearfield and above the first coincidence frequency, where the leaky wave dominates, the inclusion of structural damping shifts the leaky wave pole farther away from the saddle point and hence generates more exponential decay. However, the integral along the SDP, which depends linearly on the pole location, is slightly reduced only near the coincidence angle. In the farfield, where the solution due to the leaky wave pole decays rapidly and the integral along the SDP becomes dominant, the effect of damping is significant only near the coincidence angle. The structural damping also shifts the real surface wave pole away from the real-axis in the complex wavenumber plane and hence generates a decaying surface acoustic pressure which depends on the amount of damping added.

In conclusion, the new solutions derived in this thesis in the form of a uniformly asymptotic series and a fast-convergent numerical integral were shown to predict the radiated acoustic pressure accurately in the nearfield and at the grazing angle in contrast to solutions obtained previously by first order approximations. Since the difference in the predictions persists for non-dimensional distance $k_0 r$ over 10^3 to 10^5 , the uniformly asymptotic series solution obtained in this thesis should be used in many instances of practical interest.

6.2 Future Work

The analysis in this thesis has been concentrated on the acoustic radiation from infinite homogeneous, isotropic elastic plates excited by a line and a point forces.

However, with the application of the Green's function theory, the analysis can be easily extended to handle the same problem but with arbitrary disturbance. It can also be applied to the nearfield acoustic radiation from a moment-excited plate.

Further work of interest remaining to be done are the analyses for finite plates with boundary effects, as well as non-isotropic or inhomogeneous plates.

Ω	K_0		$\epsilon(\Omega)$	
	Air	Water	Air	Water
0.1	3.1655	3.4707	1.8195	1.9161
0.5	1.4181	1.5557	0.8853	1.0107
1.0	1.0064	1.1511	0.1127	0.5431
3.0	1.0000	1.0004	$3.20 \cdot 10^{-5}$	$2.86 \cdot 10^{-2}$
5.0	1.0000	1.0001	$7.76 \cdot 10^{-6}$	$1.22 \cdot 10^{-2}$
10.0	1.0000	1.0000	$1.71 \cdot 10^{-6}$	$5.25 \cdot 10^{-3}$
13.0	1.0000	1.0000	$1.10 \cdot 10^{-6}$	$3.95 \cdot 10^{-3}$

Table 1 Surface wave pole K_0 and $\epsilon(\Omega)$.

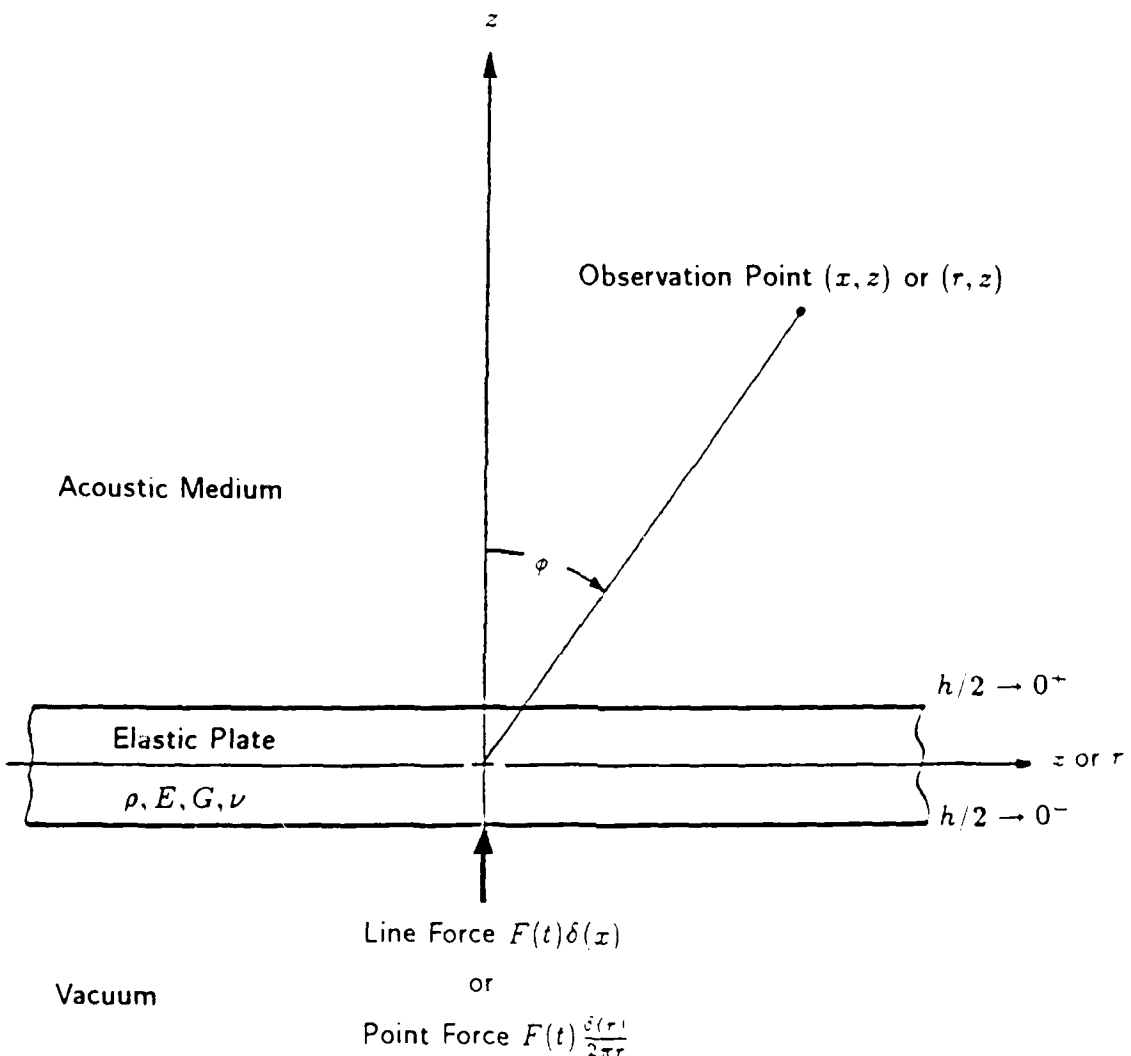


Figure 1 Geometry of a line- or point-excited fluid-loaded elastic plate and the coordinate system.

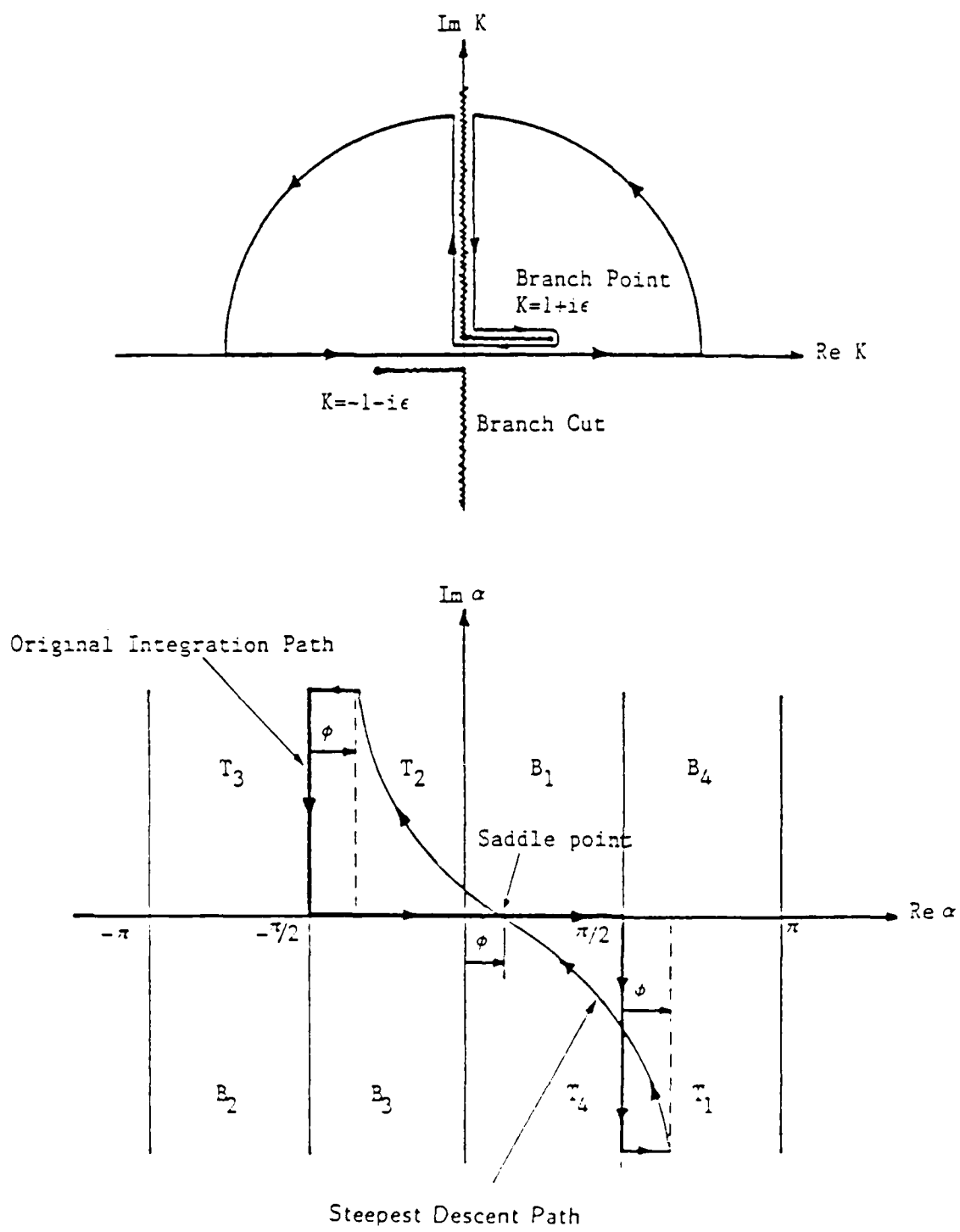
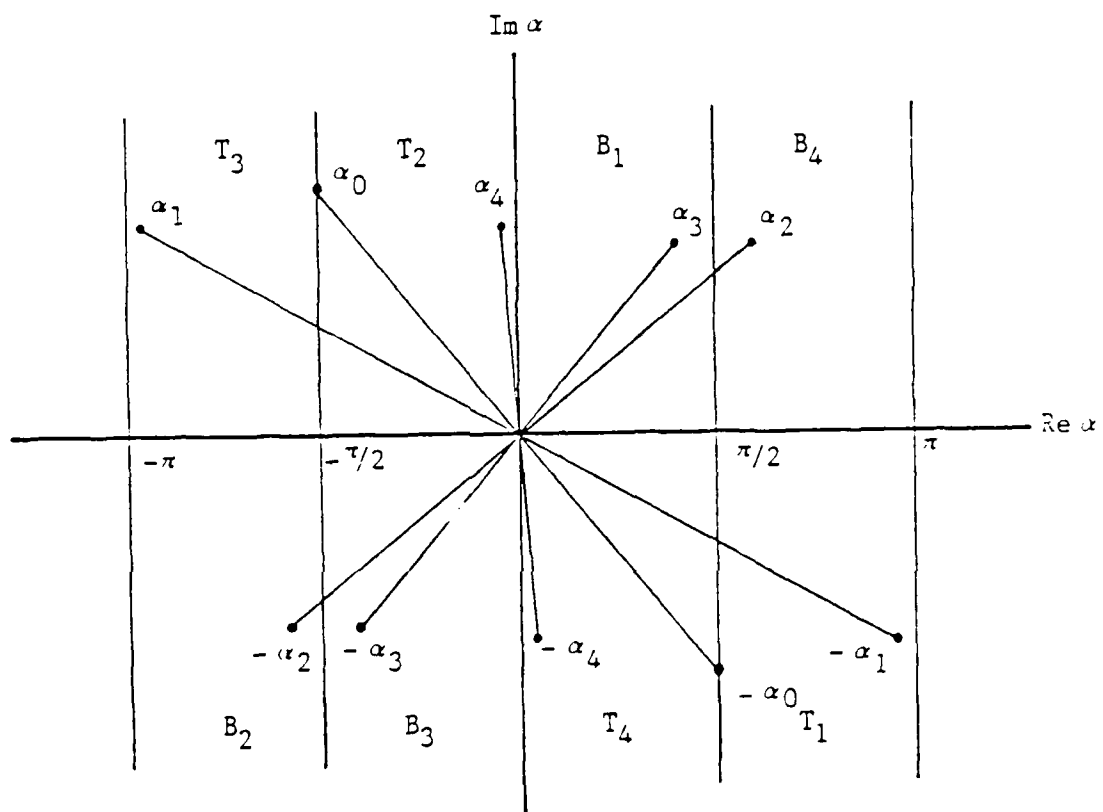


Figure 2 Integration paths and steepest descent path in the complex K - and α -plane.



$\pm\alpha_0$: true surface wave poles.

$\pm\alpha_{1,4}$: complex surface wave poles.

$\pm\alpha_{2,3}$: leaky wave poles (also $\pm\alpha_{1,4}$ if $\Omega > \Omega_m$).

Figure 3 Typical locations of poles in the complex α -plane.

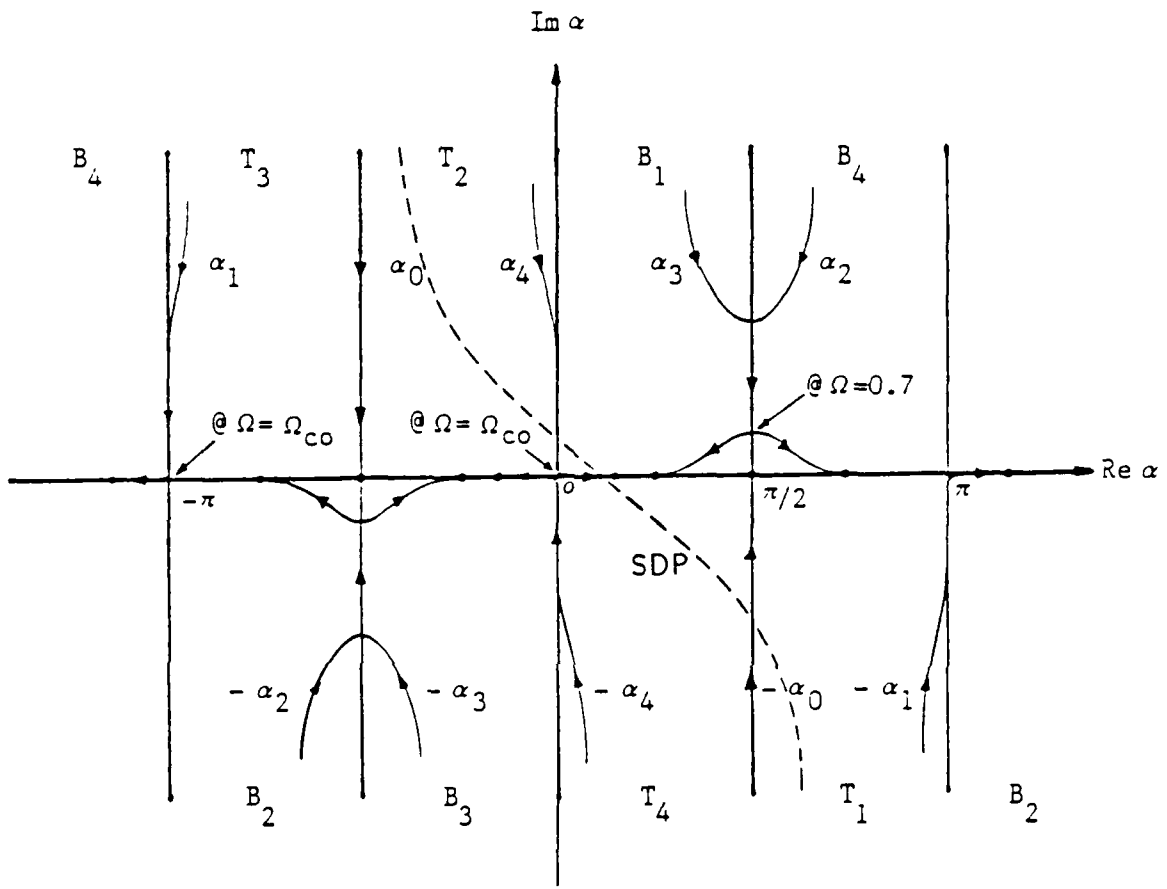


Figure 4 Frequency loci of poles in the complex α -plane.

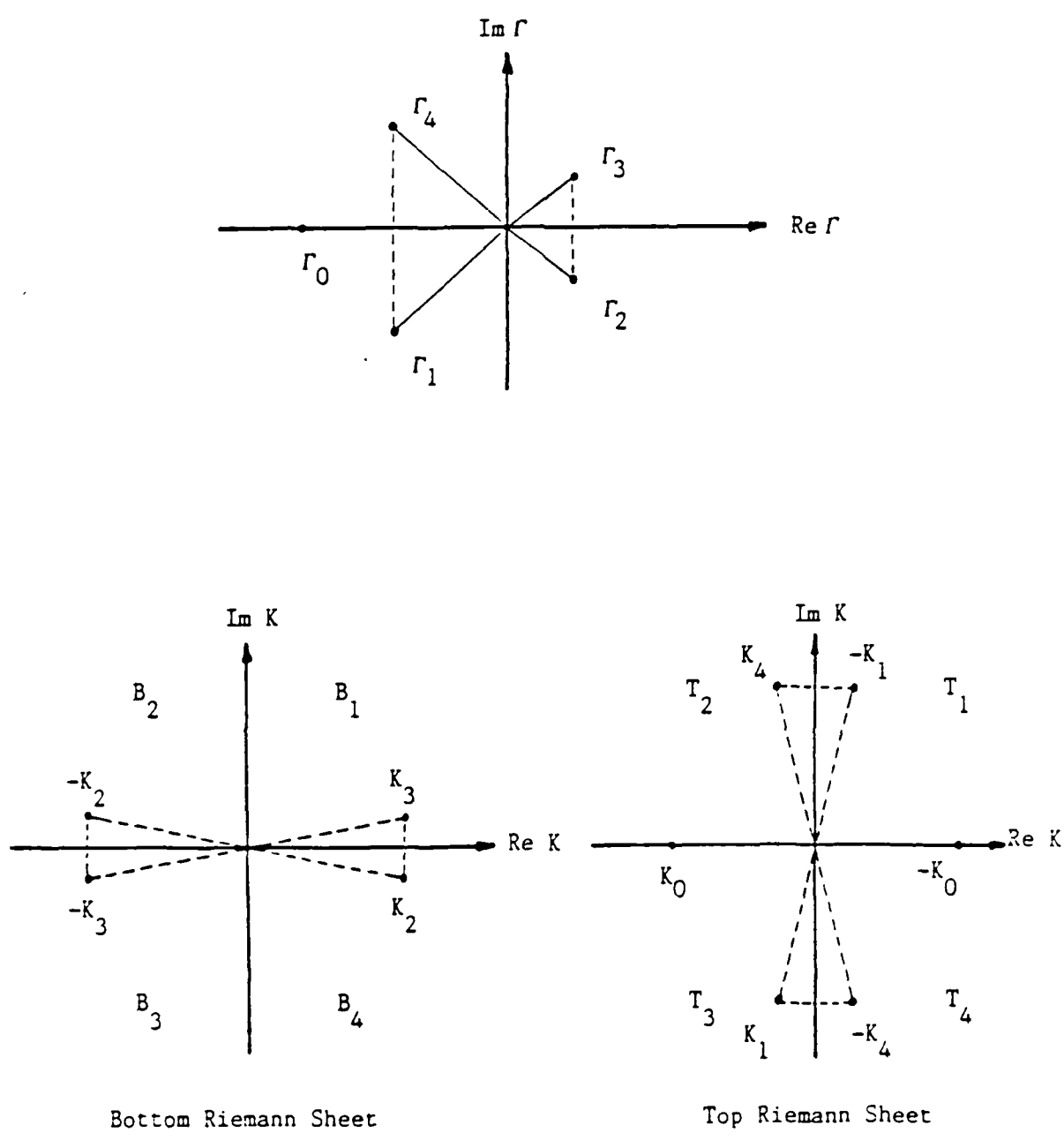


Figure 5 Typical locations of poles in the complex Γ - and K -plane.

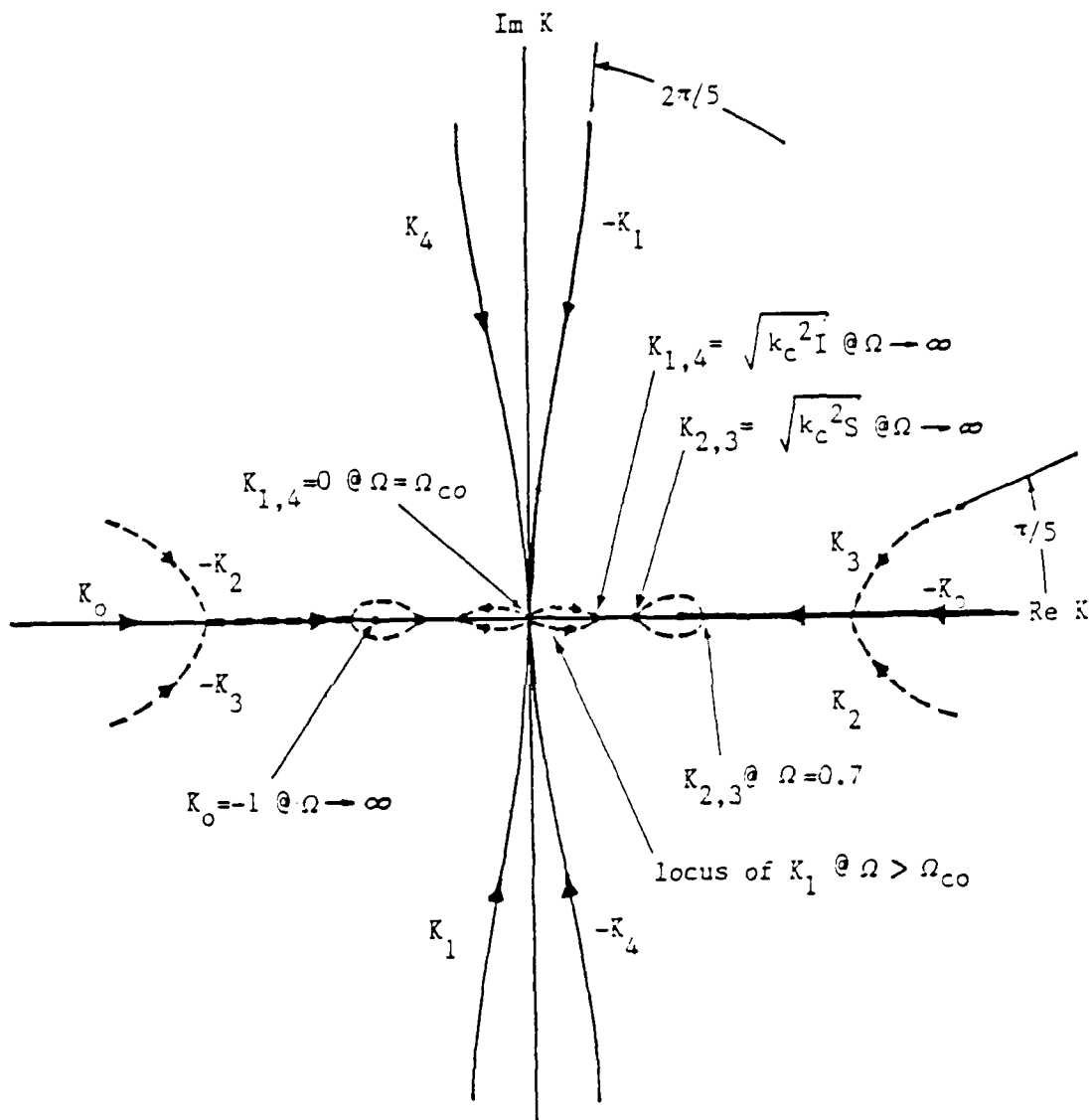


Figure 6 Frequency loci of poles in the complex K -plane.

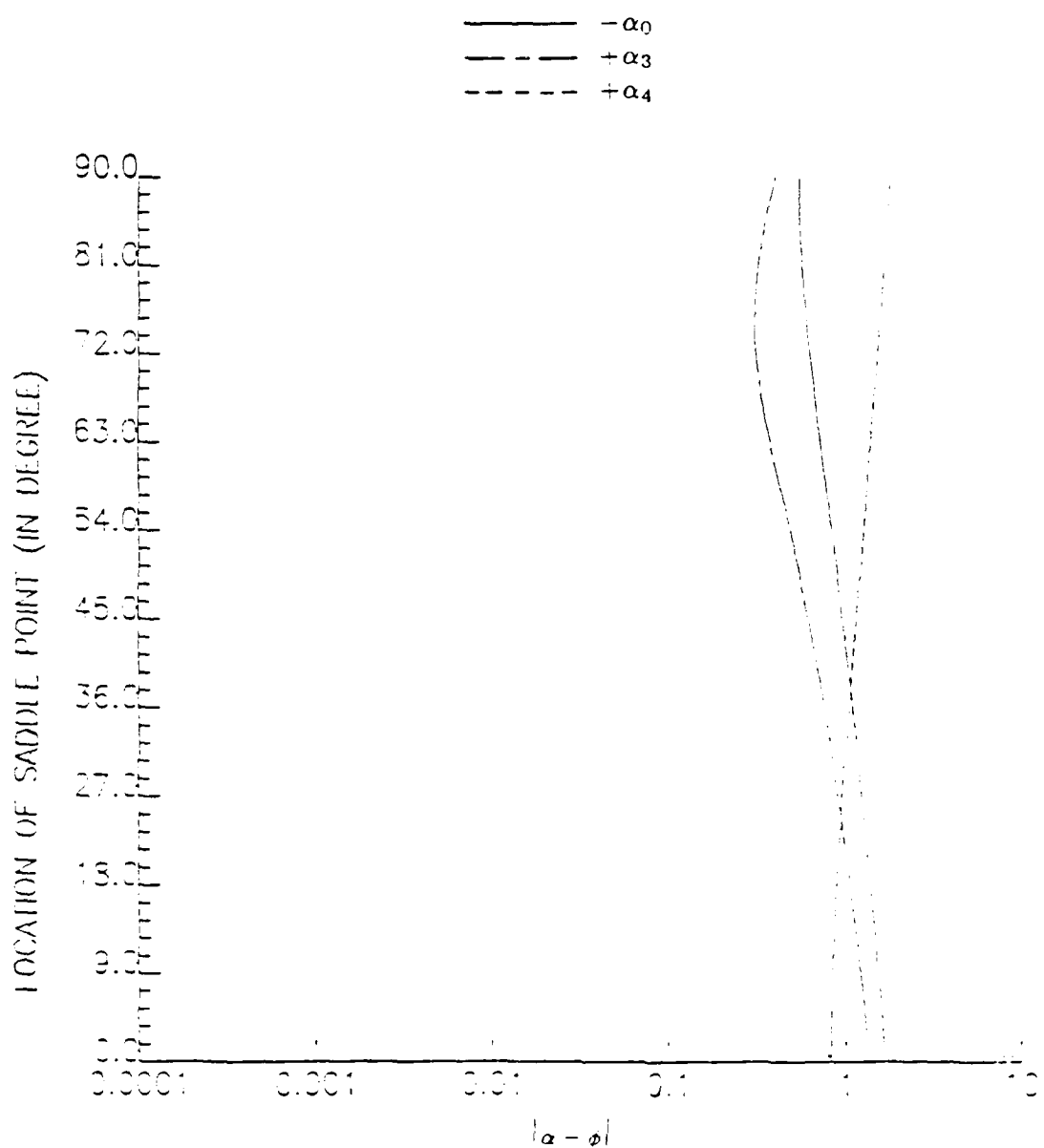


Figure 7 Distance between the saddle point and the poles in the complex α -plane. $\Omega = 1.0$.

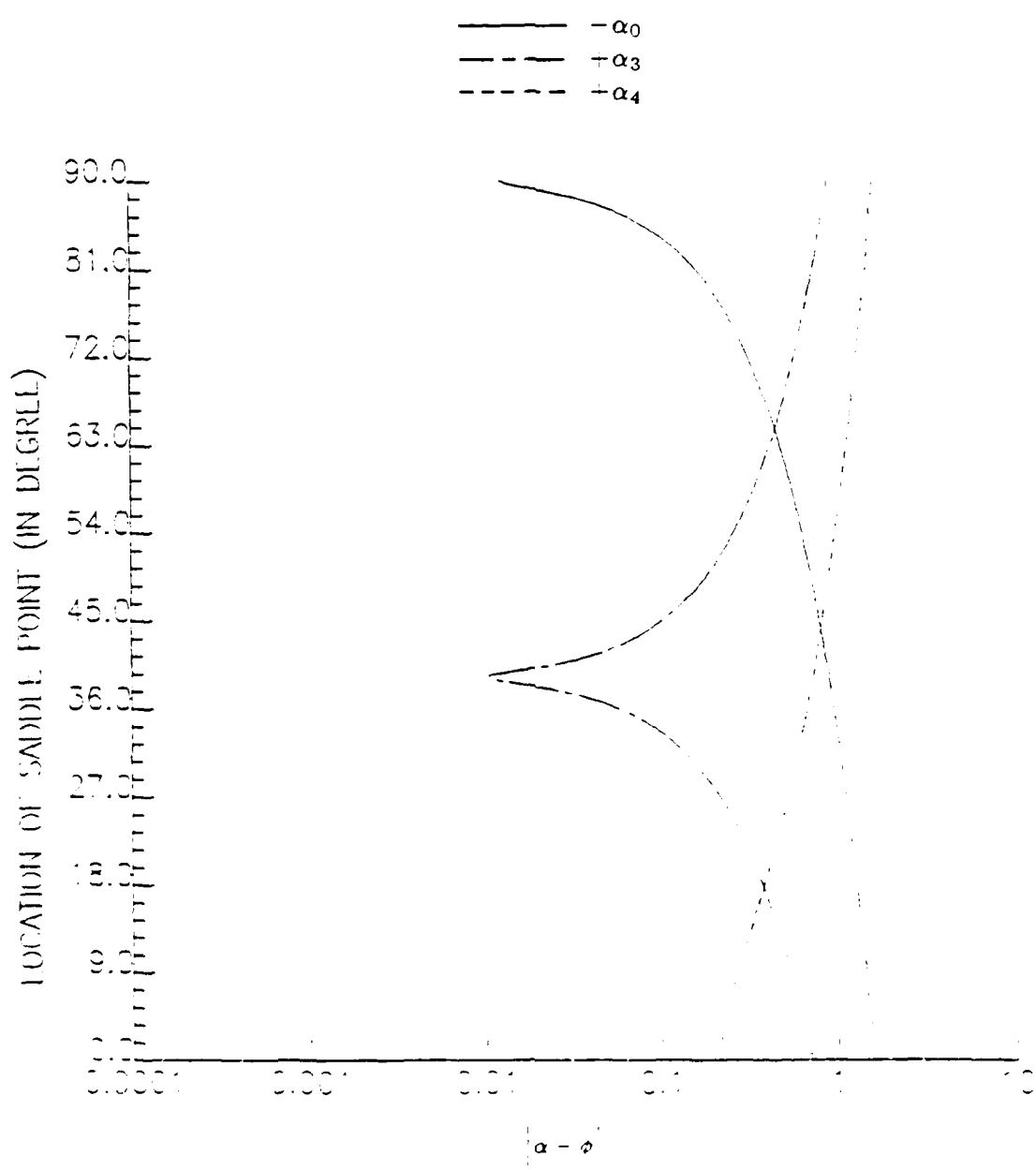


Figure 8 Distance between the saddle point and the poles in the complex α -plane. $\Omega = 5.0$.

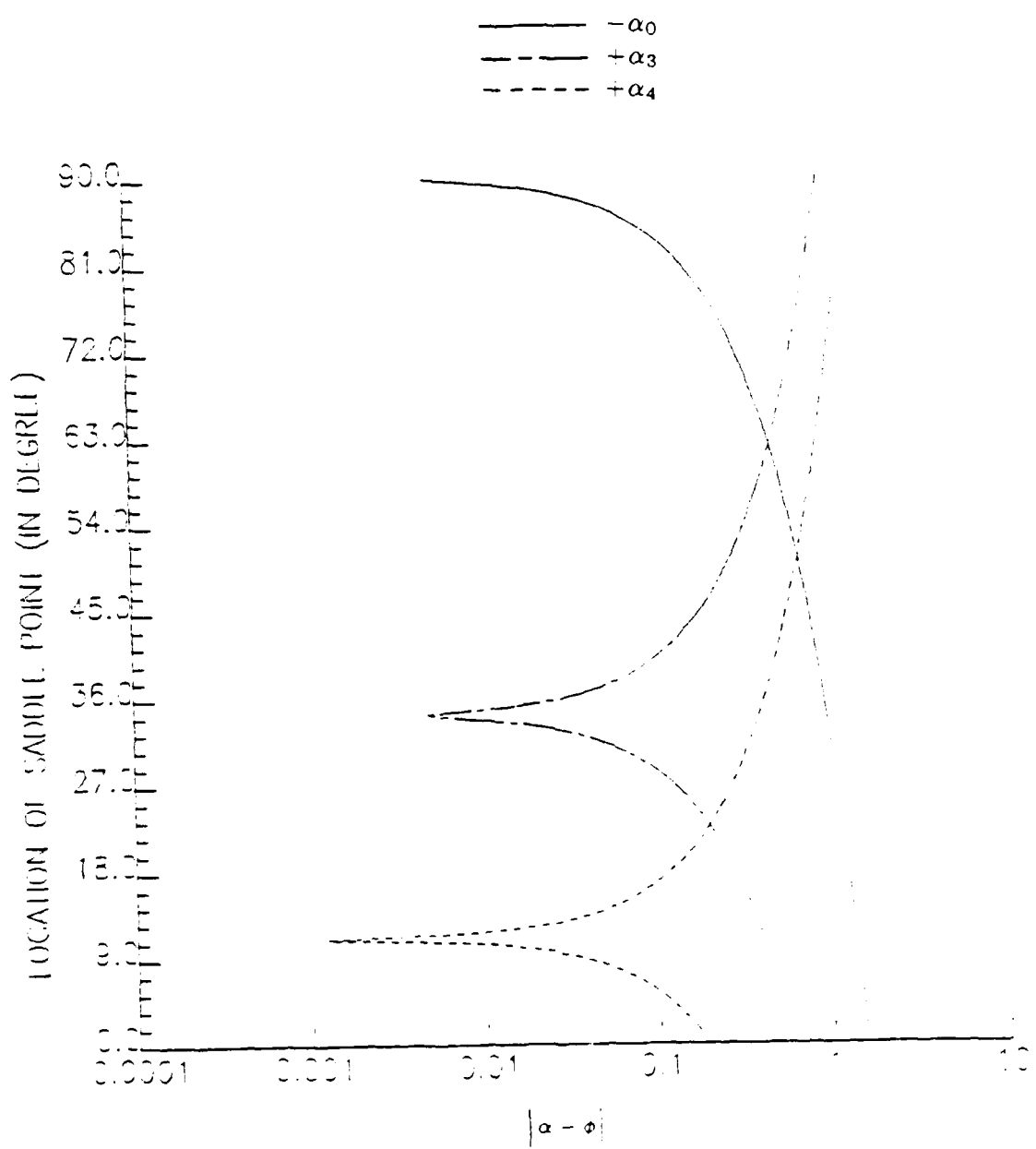


Figure 9 Distance between the saddle point and the poles in the complex α -plane. $\Omega = 10.0$.

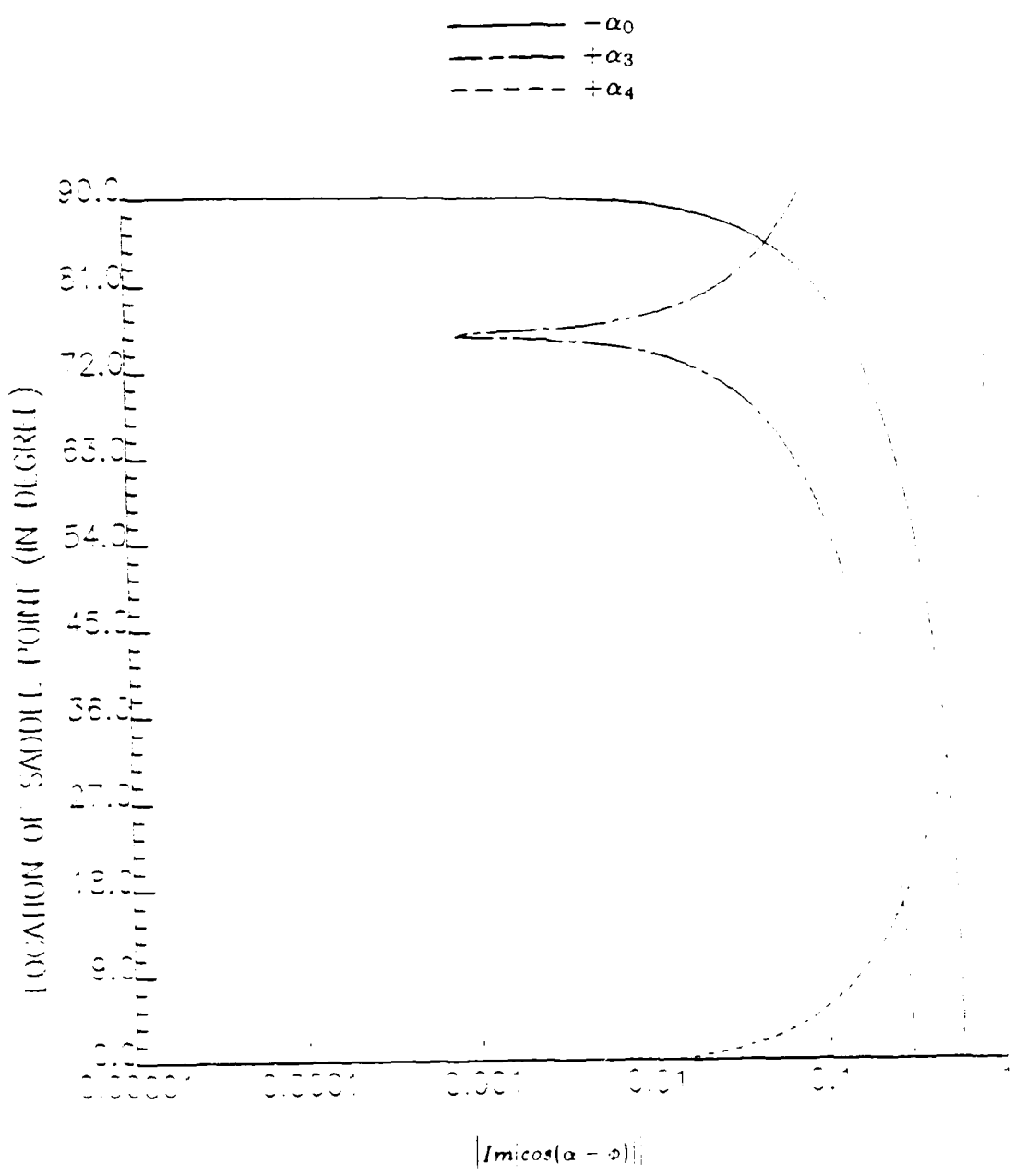


Figure 10 Absolute values of $Im[\cos(\alpha - \phi)]$, $\Omega = 1.0$.

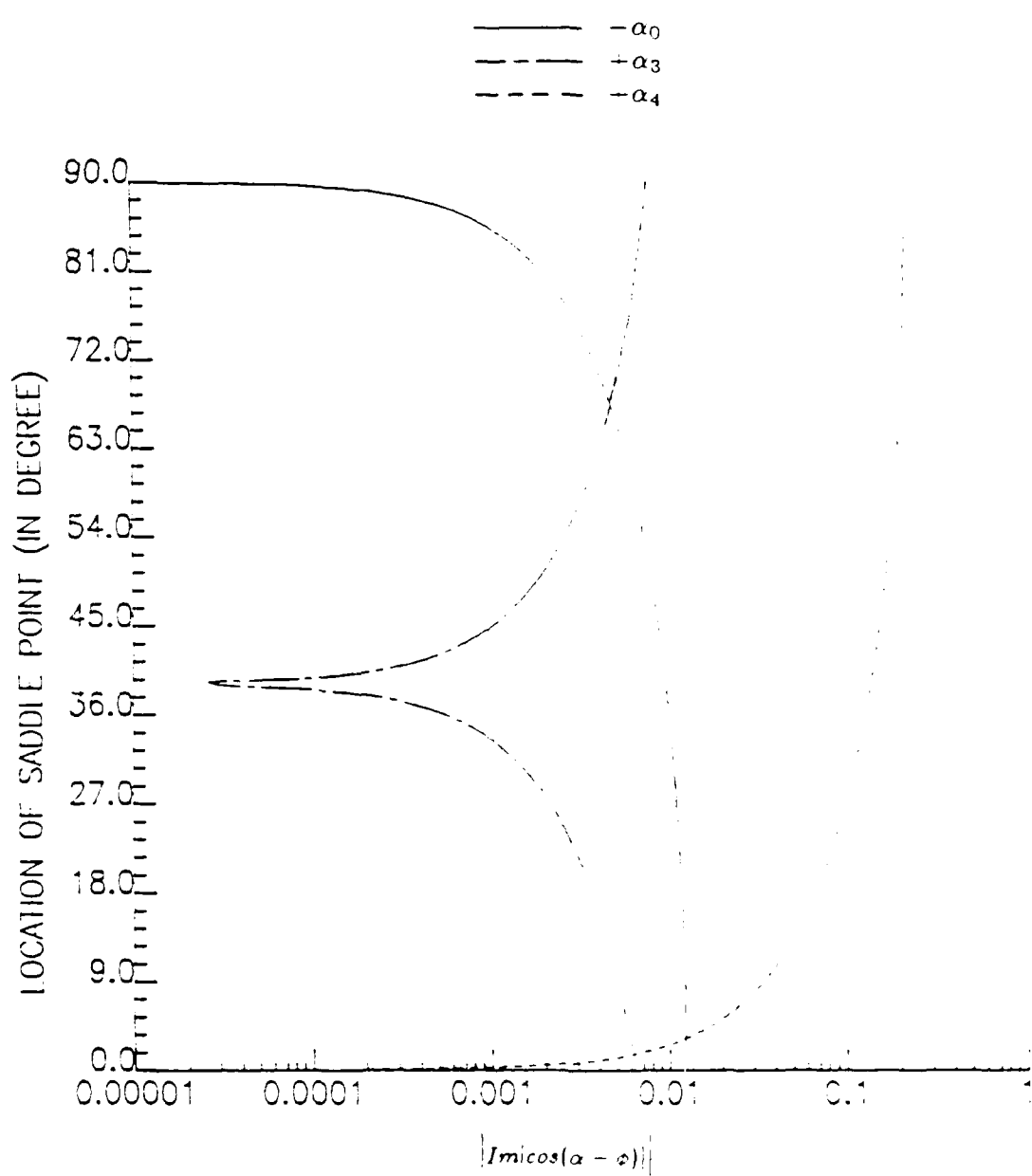


Figure 11 Absolute values of $Im[\cos(\alpha - \phi)]$. $\Omega = 5.0$.

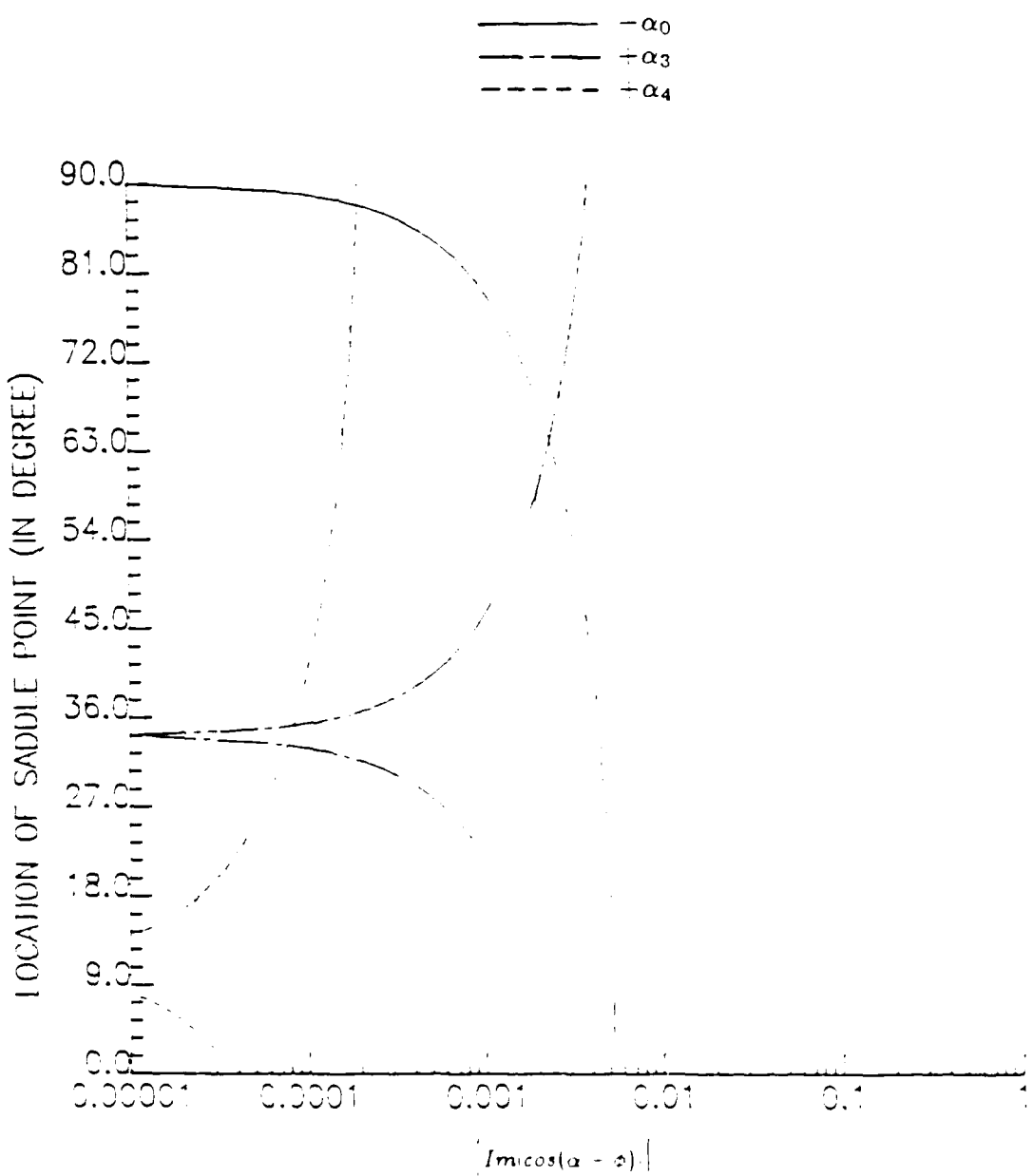


Figure 12 Absolute values of $|Im[\cos(\alpha - \phi)]|$, $\Omega = 10.0$.

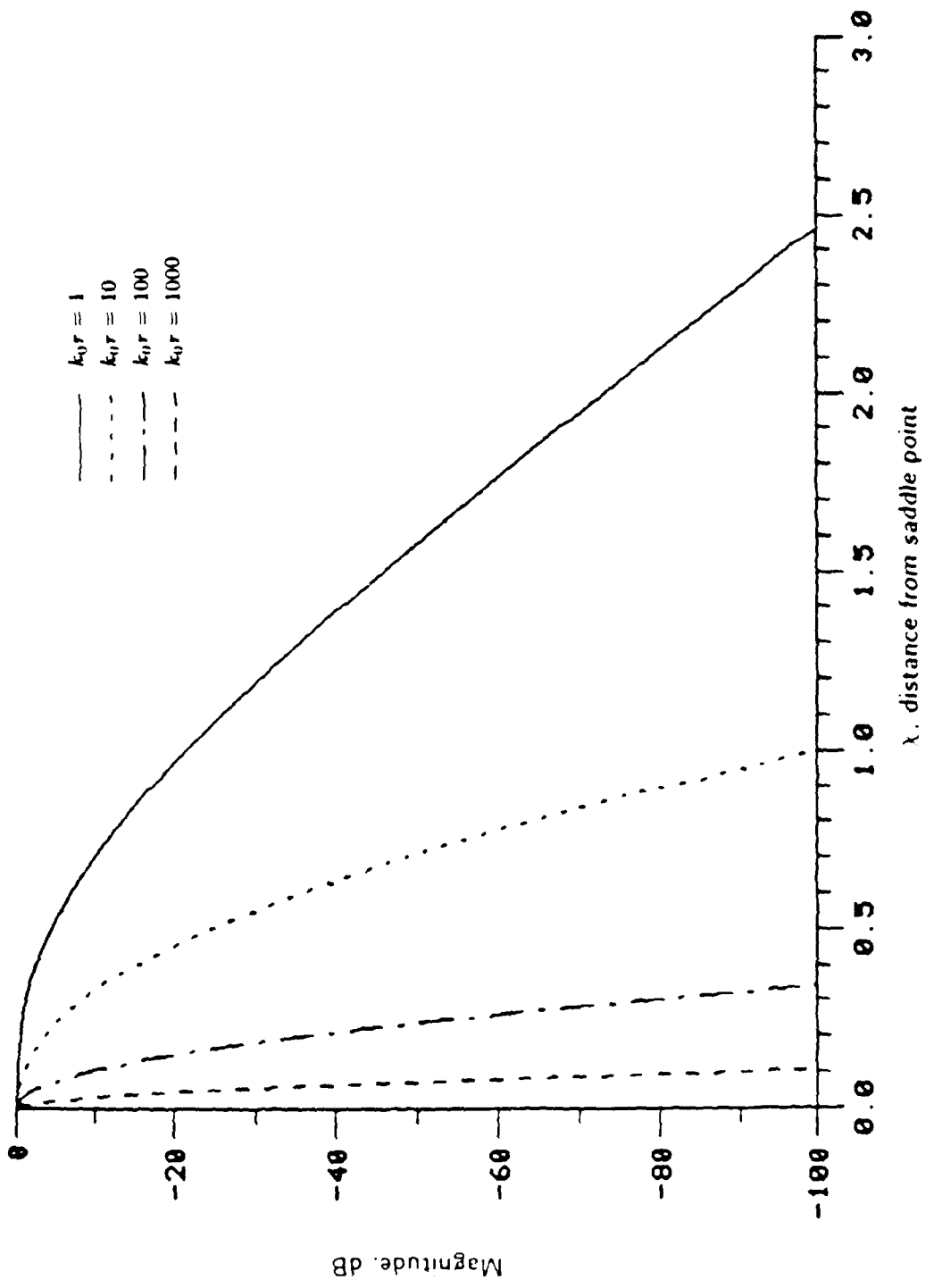


Figure 13 Magnitude of integrand along SDP- line-excited plate
at $\Omega = 1.0$ and $\phi = 0^\circ$.

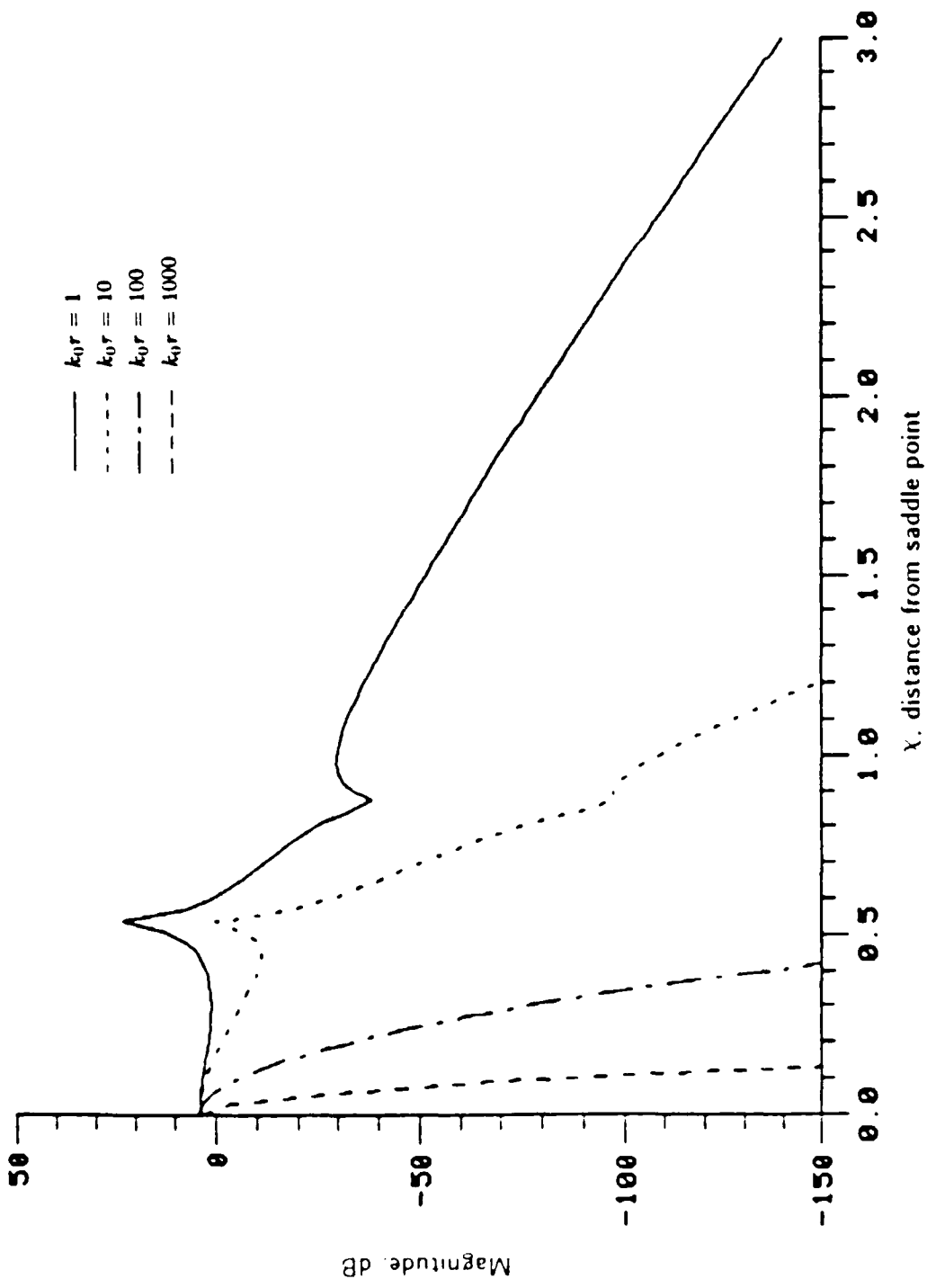


Figure 14 Magnitude of integrand along SDP-line-excited plate
at $\Omega = 1.0$ and $\phi = 60^\circ$.

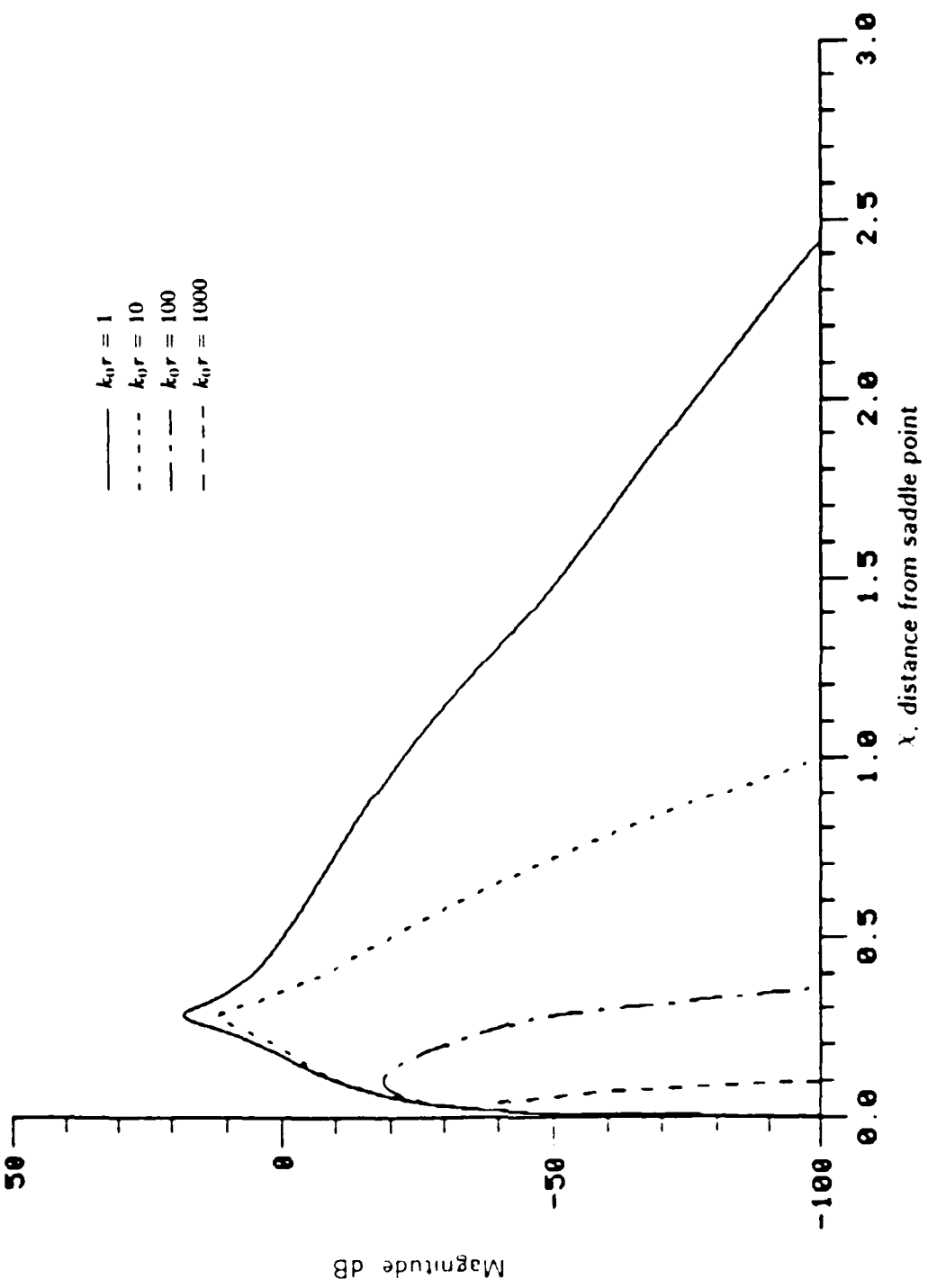


Figure 15 Magnitude of integrand along SDP- line-excited plate at $\Omega = 1.0$ and $\phi = 90^\circ$.

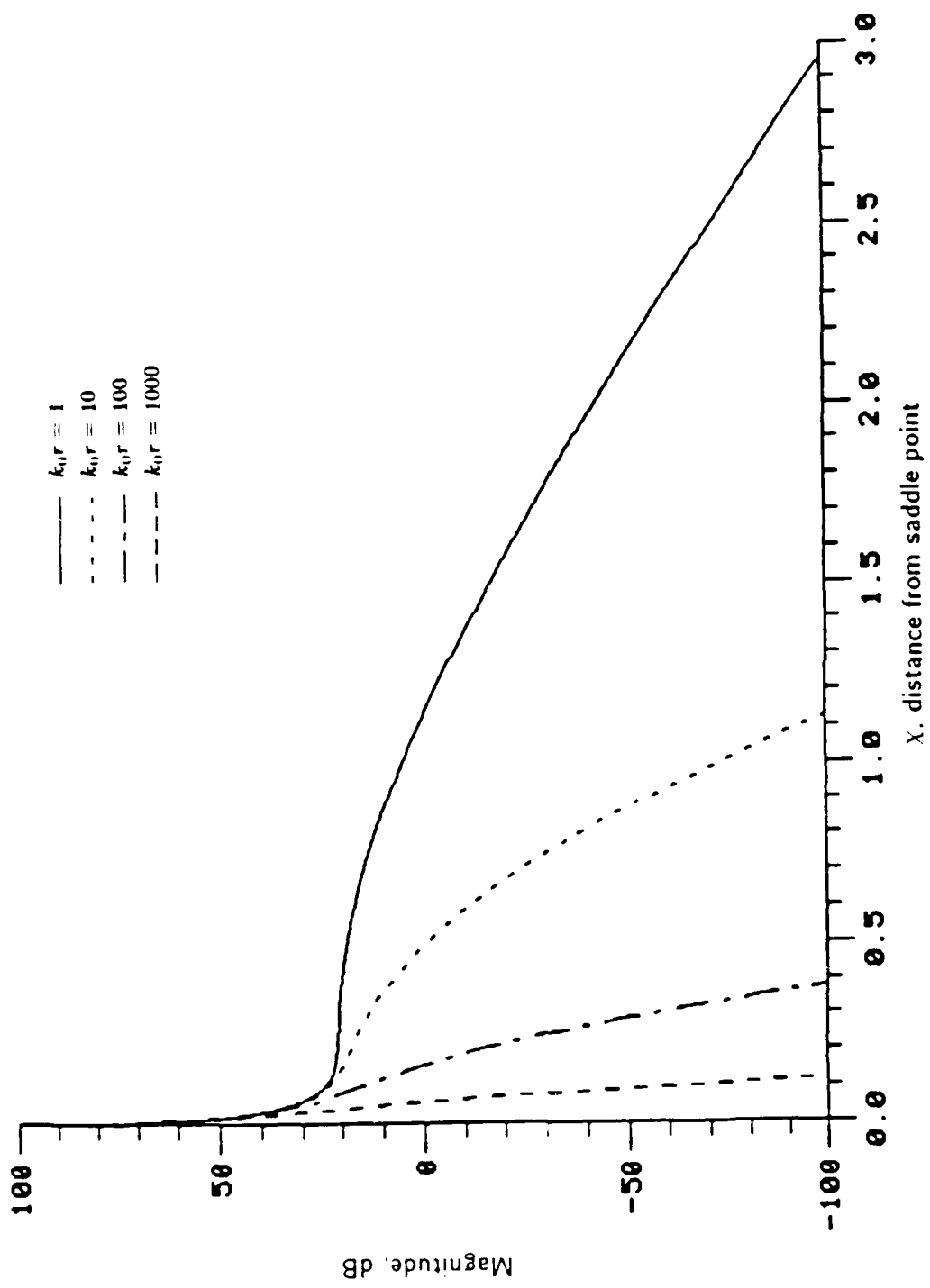


Figure 16 Magnitude of integrand along SDP-line-excited plate
at $\Omega = 10.0$ and $\phi = 34^\circ$.

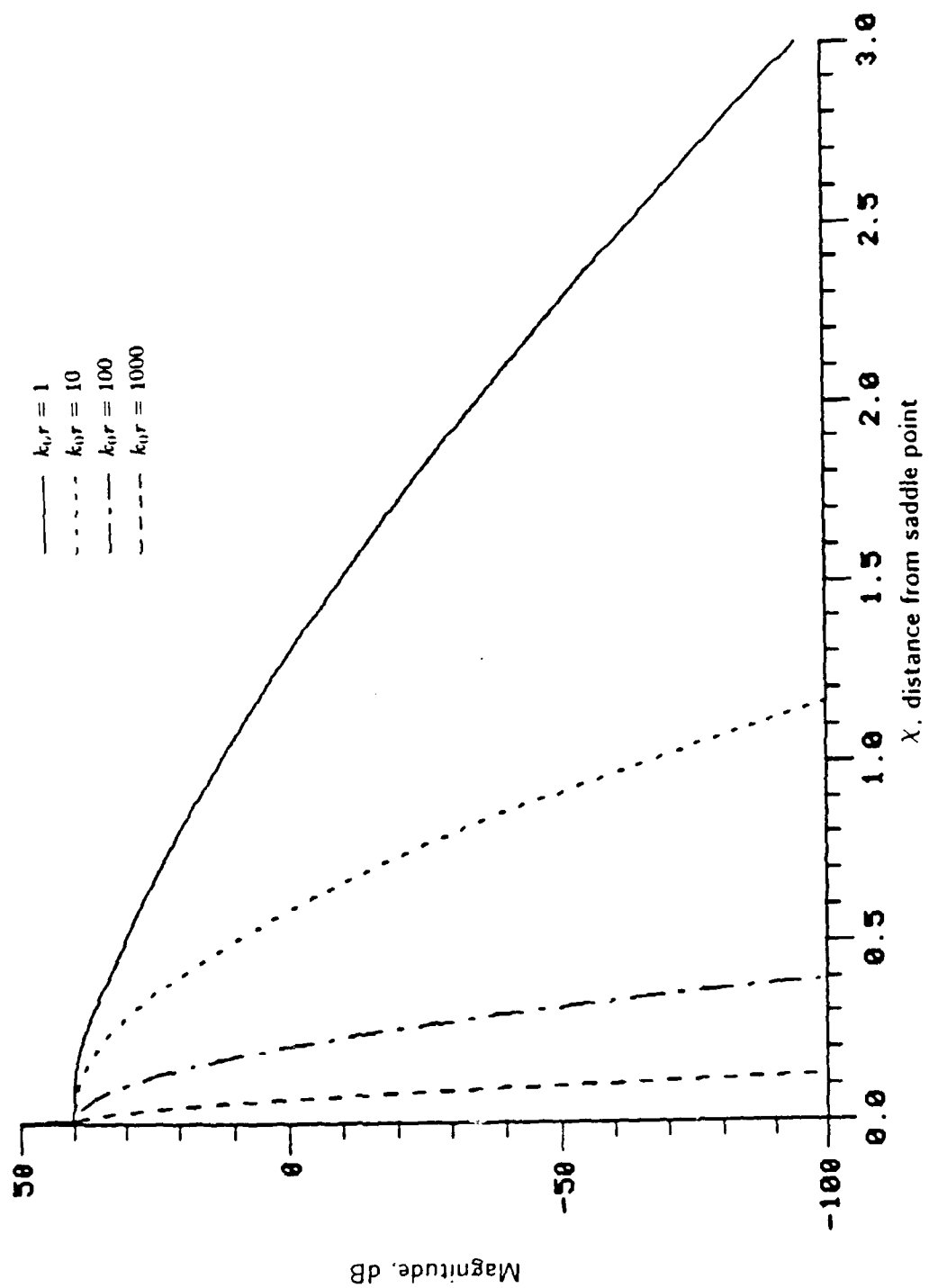
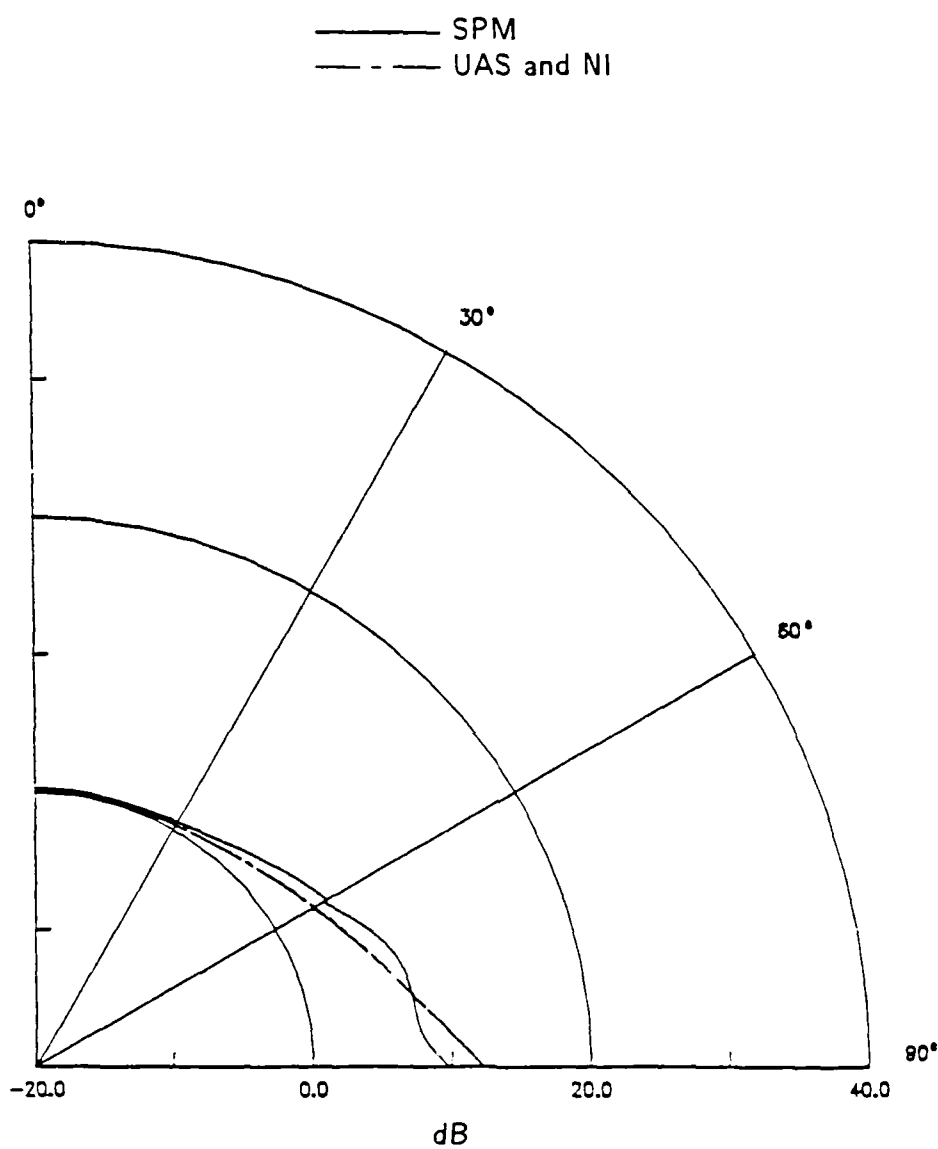
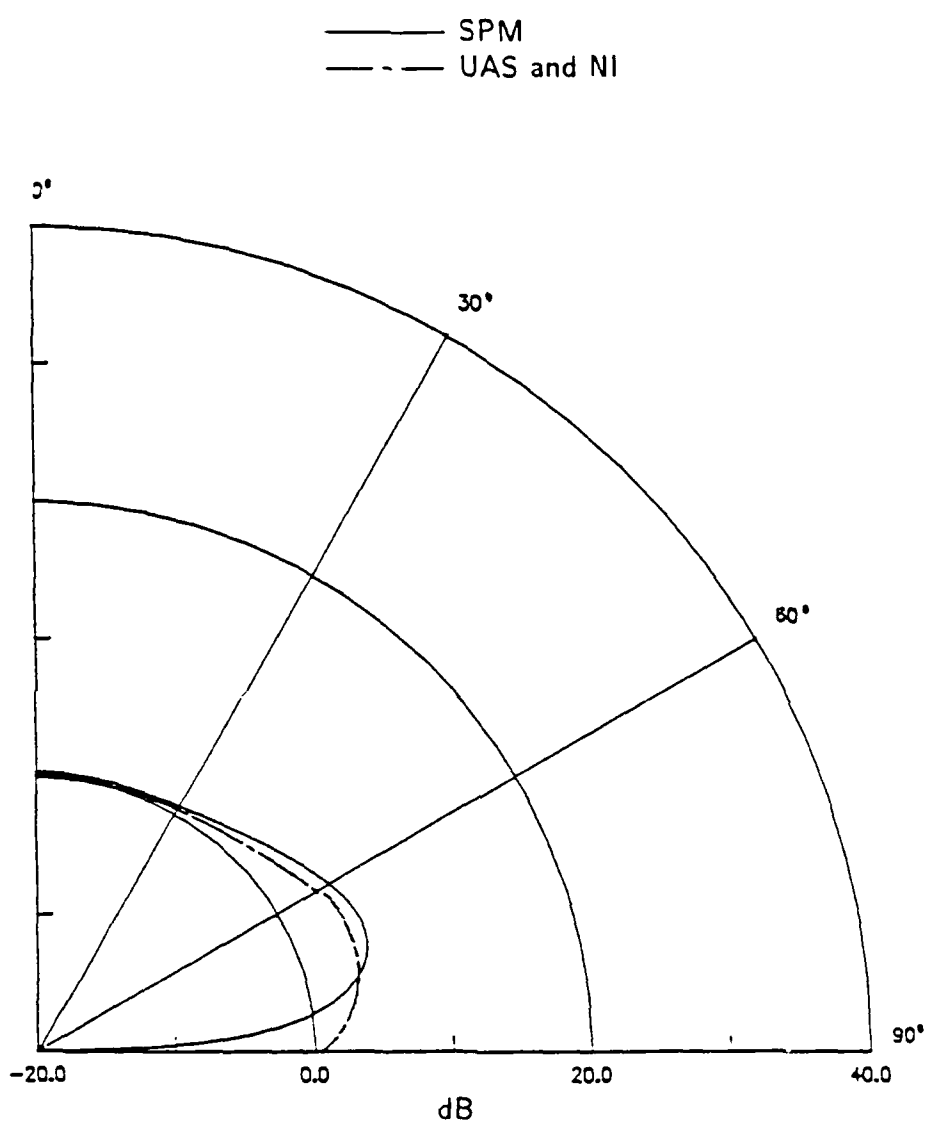


Figure 17 Magnitude of integrand along SDP-line-excited plate
at $\Omega = 10.0$ and $\phi = 11^\circ$.



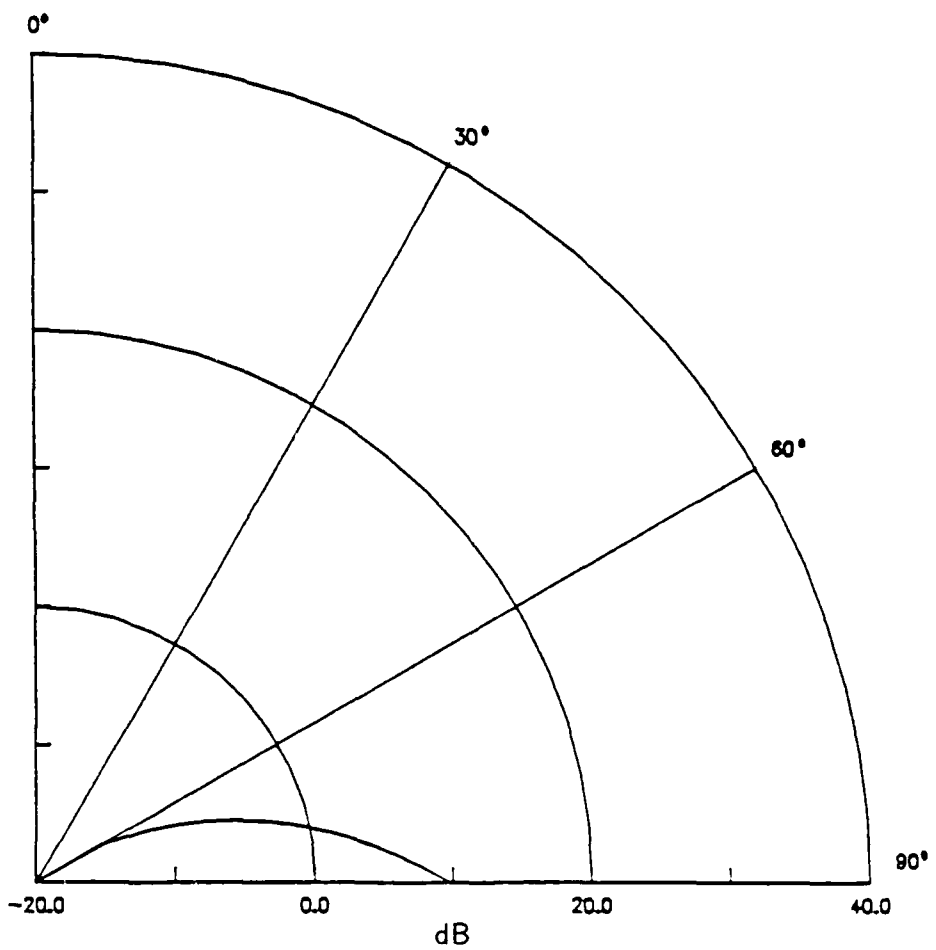
a. Total acoustic pressure.

Figure 18 Normalized directivity function for a line-excited fluid-loaded steel plate. $k_0r = 10$, $\Omega = 1.0$.



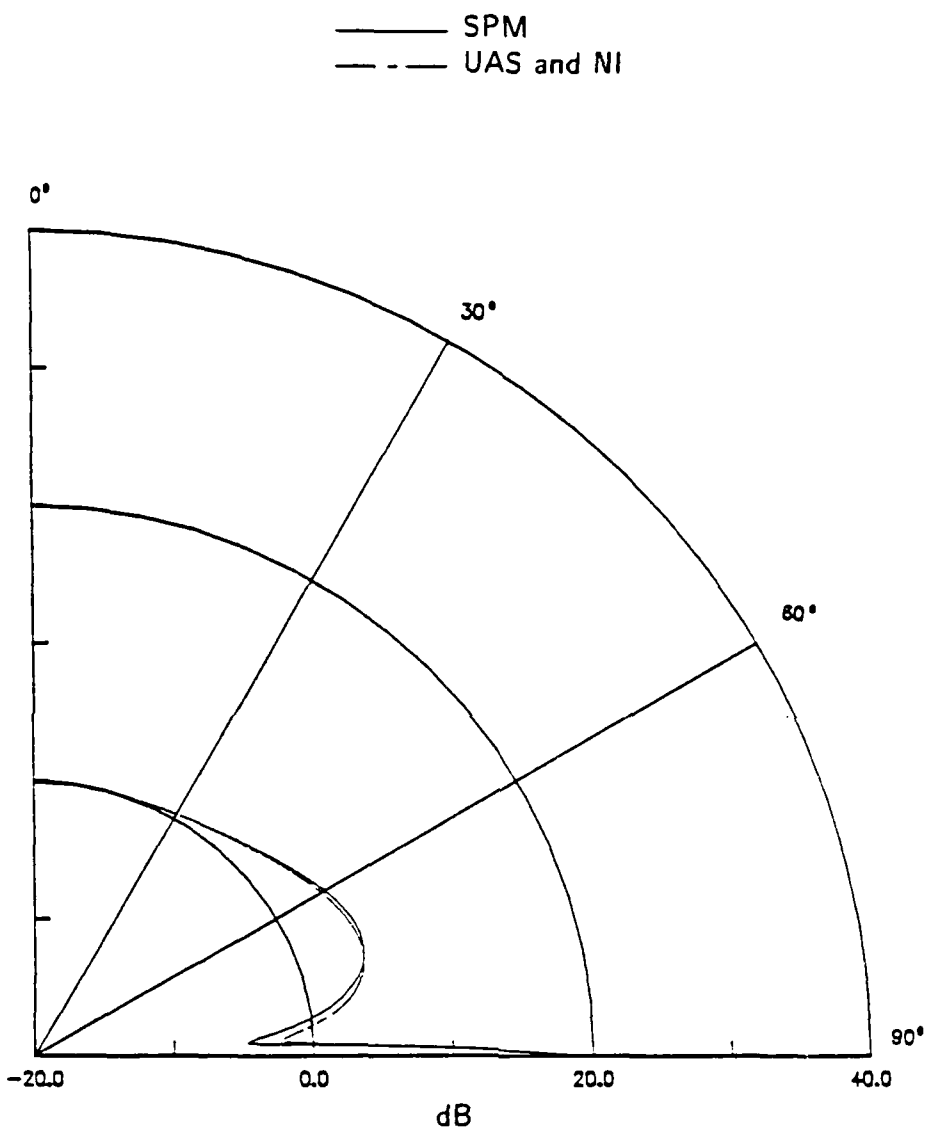
b. Integral along EDP only.

Figure 18 Continued



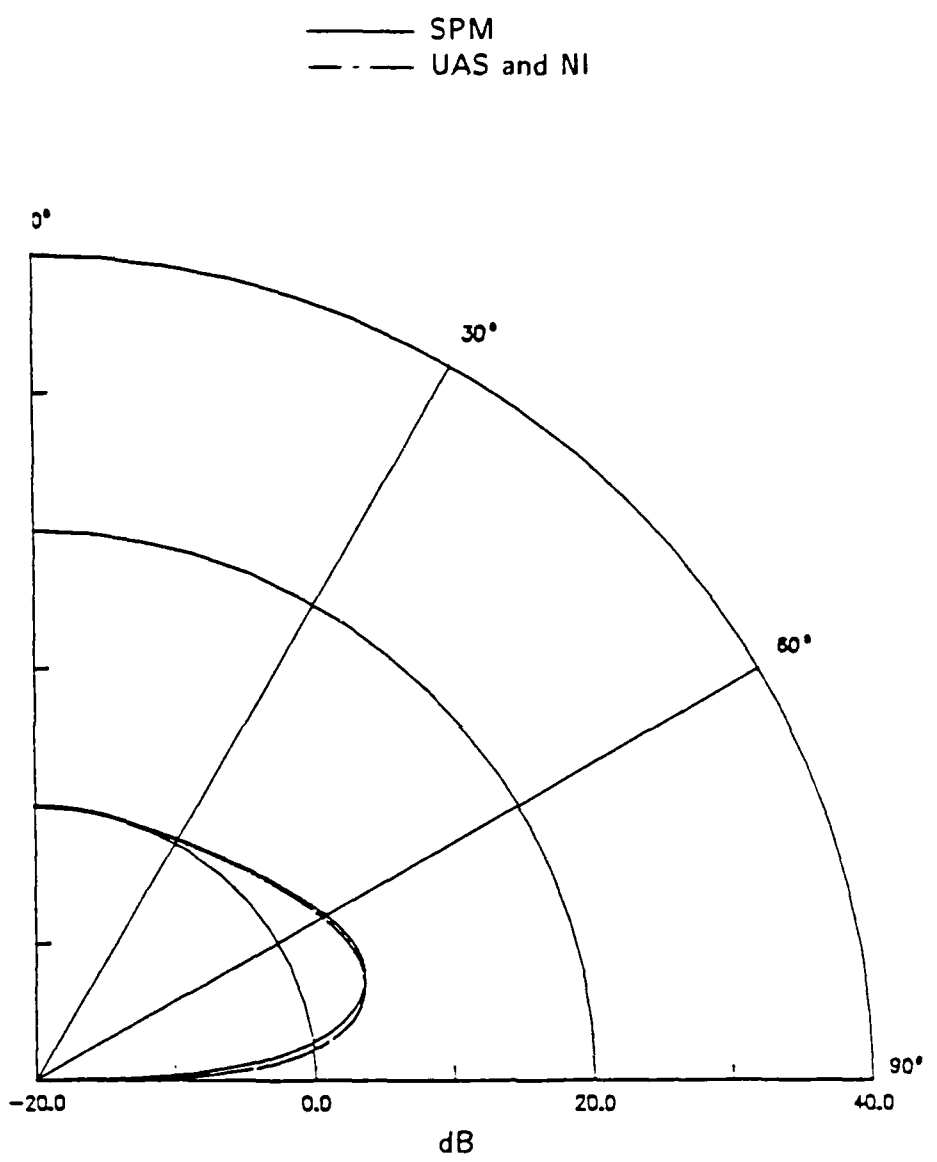
c. Residues of poles only.

Figure 18 Continued



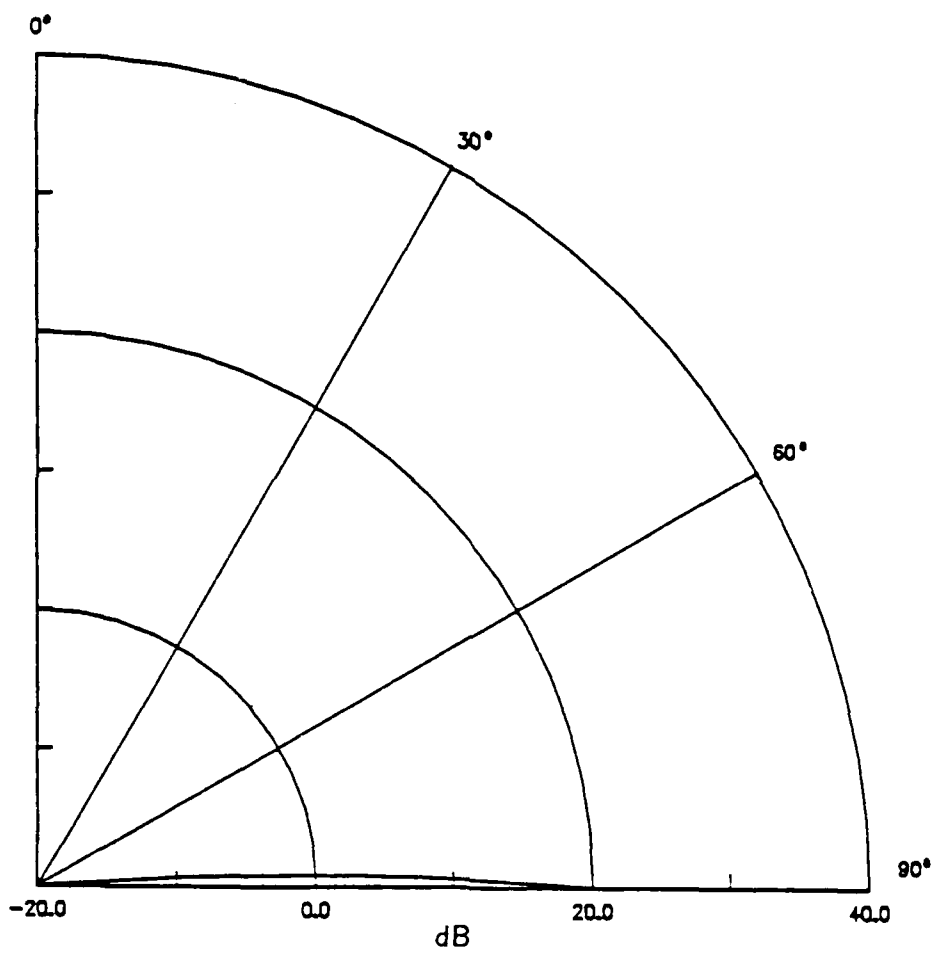
a. Total acoustic pressure.

Figure 19 Normalized directivity function for a line-excited fluid-loaded steel plate, $k_0 r = 10^2$, $\Omega = 1.0$.



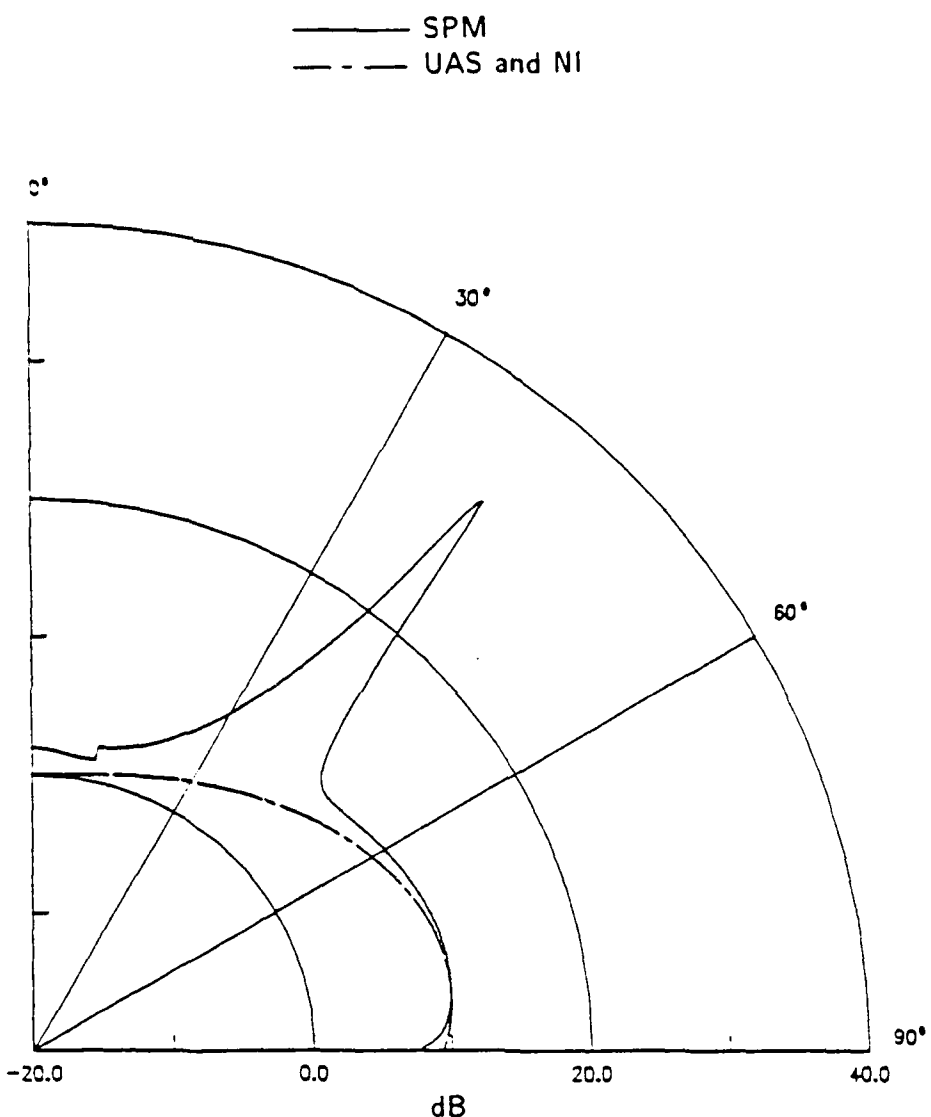
b. Integral along SDP only.

Figure 19 Continued



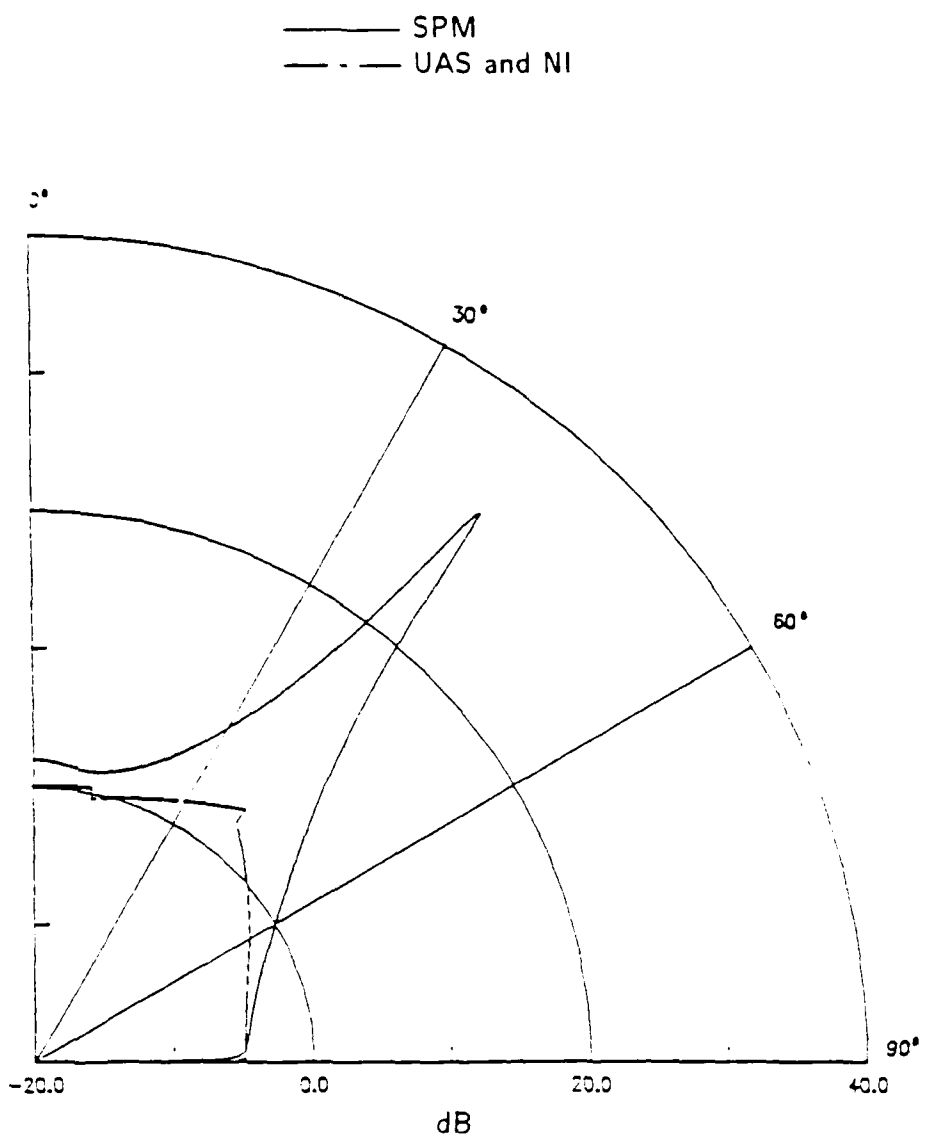
c. Residues of poles only.

Figure 19 Continued



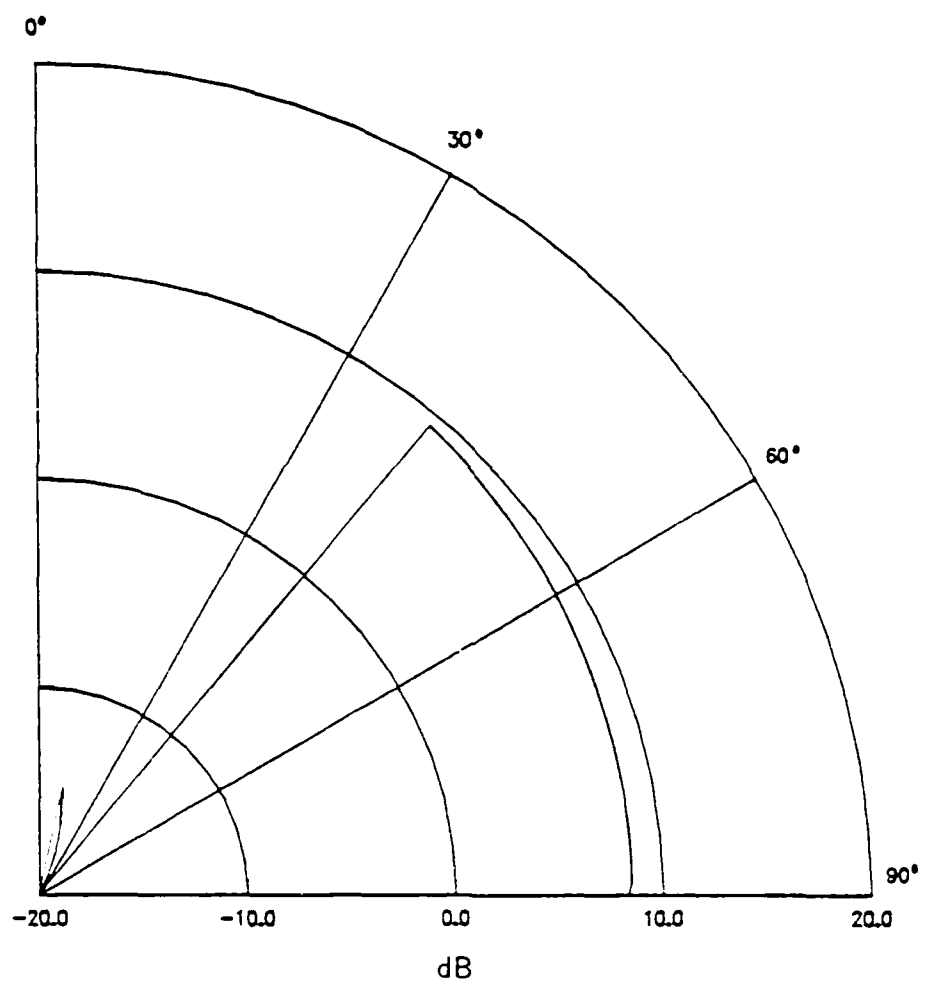
a. Total acoustic pressure.

Figure 20 Normalized directivity function for a line-excited fluid-loaded steel plate. $k_0 r = 10$. $\Omega = 5.0$.



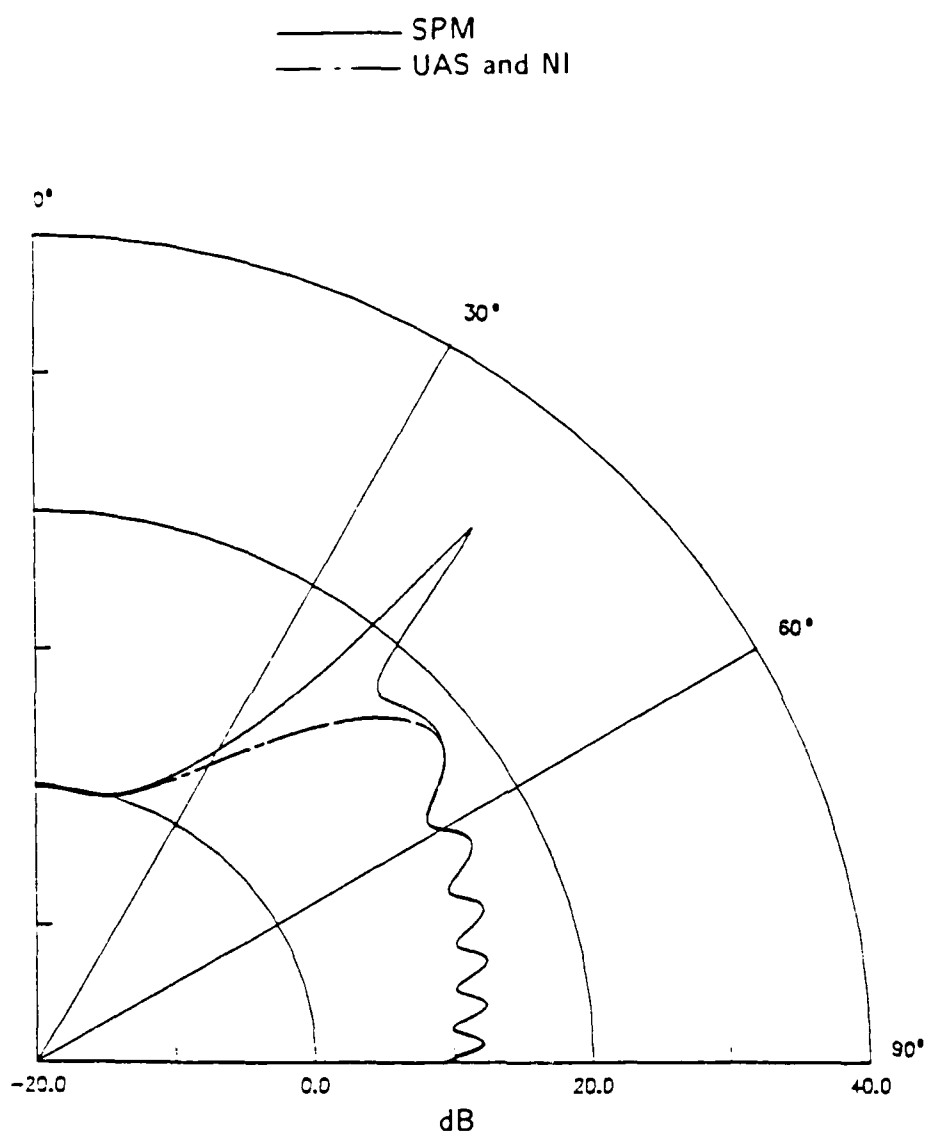
b. Integral along SDP only.

Figure 20 Continued



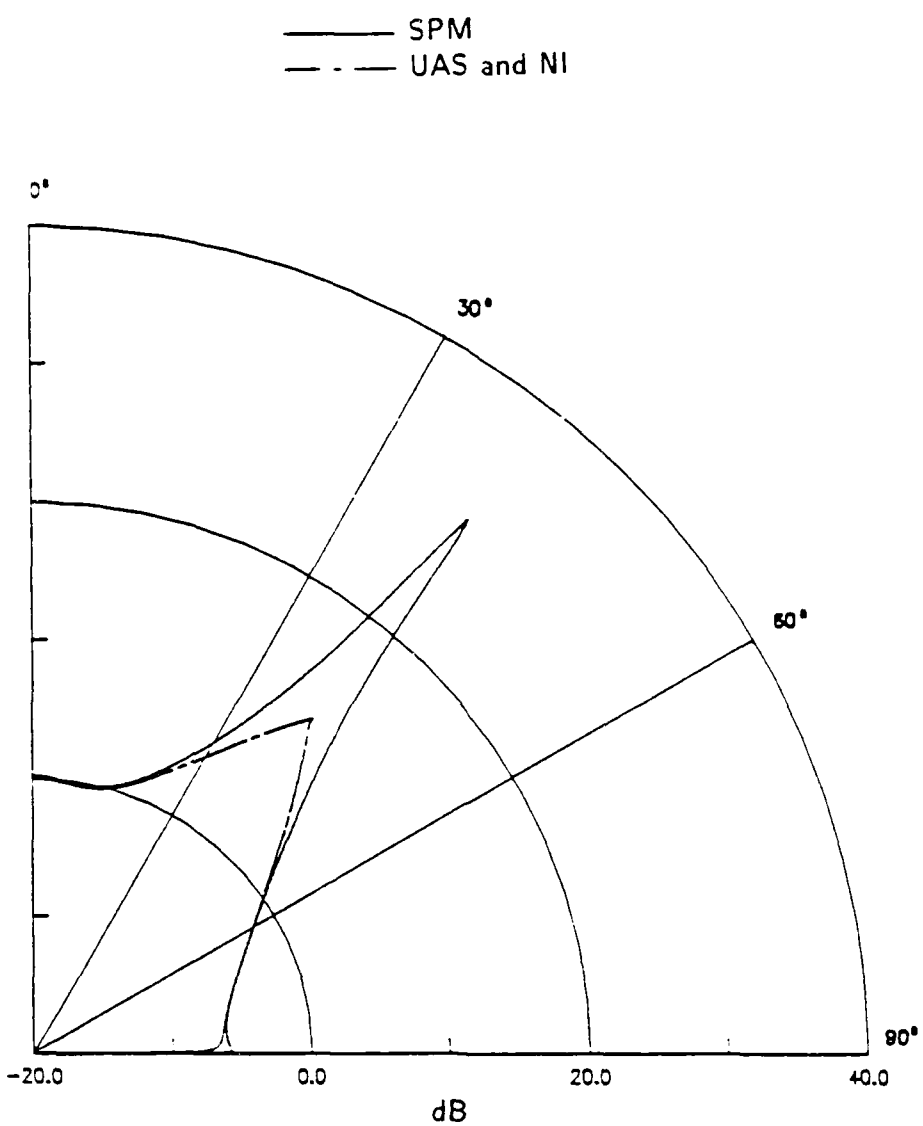
c. Residues of poles only.

Figure 20 Continued



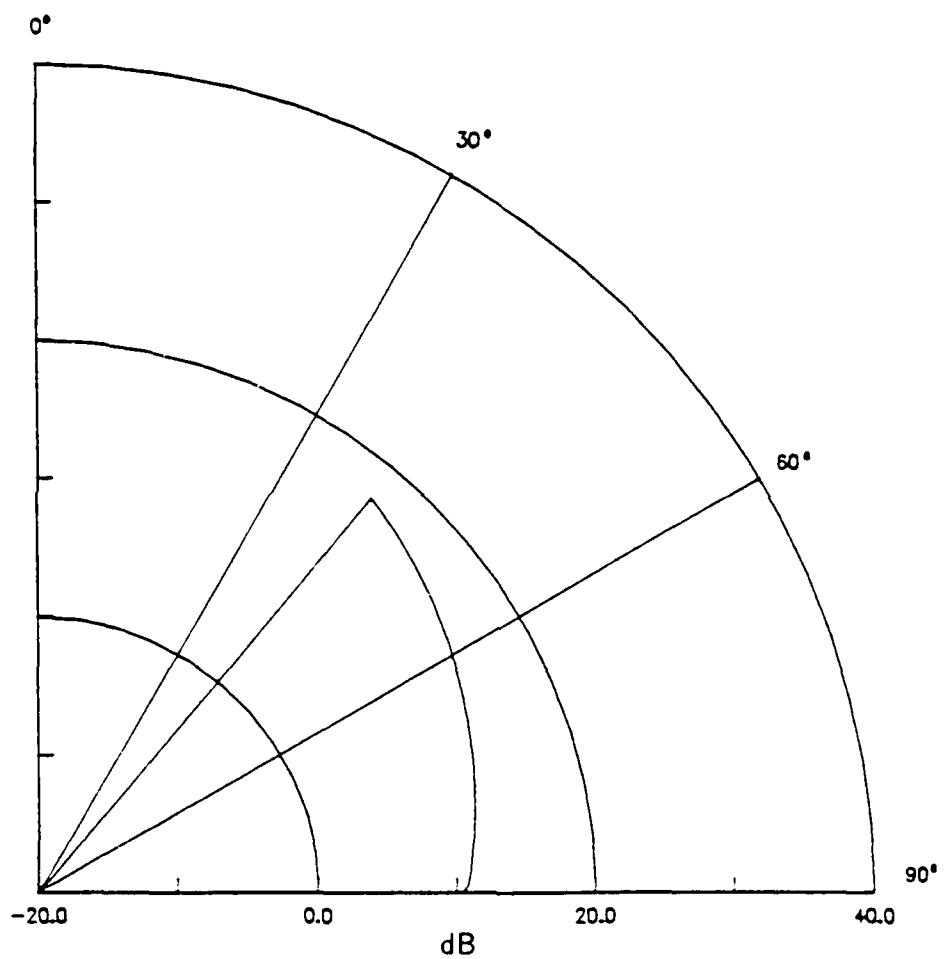
a. Total acoustic pressure.

Figure 21 Normalized directivity function for a line-excited fluid-loaded steel plate. $k_{nr} = 10^2$, $\Omega = 5.0$.



b. Integral along SDP only.

Figure 21 Continued



c. Residues of poles only.

Figure 21 Continued

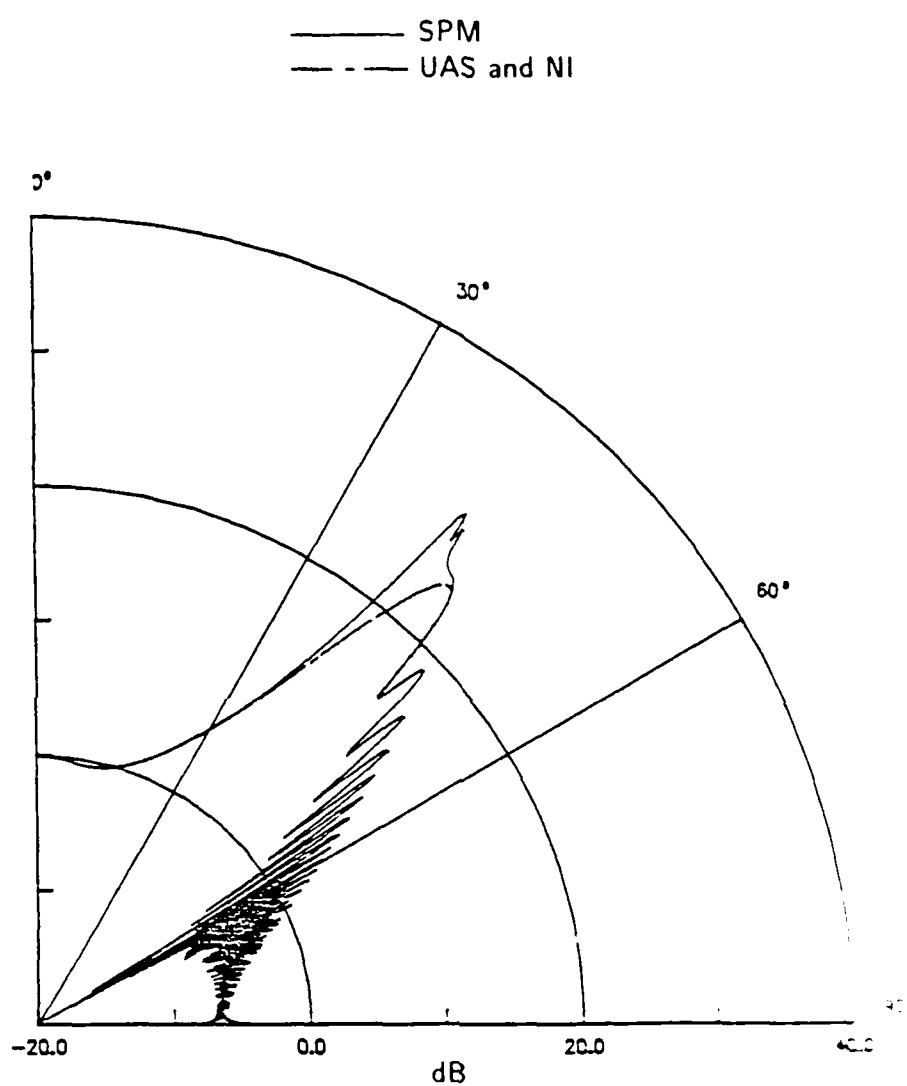


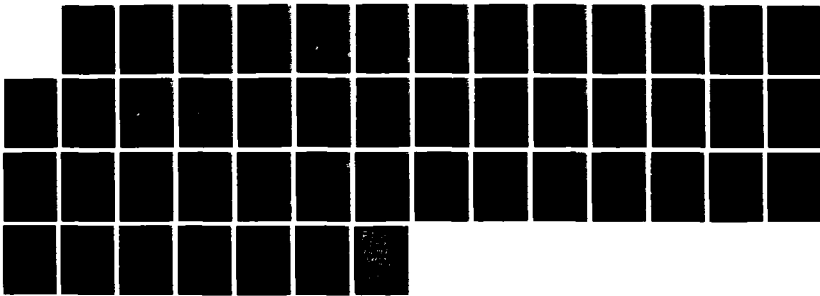
Figure 22 Normalized directivity function for a fluid-loaded steel plate. ($k \tau$)

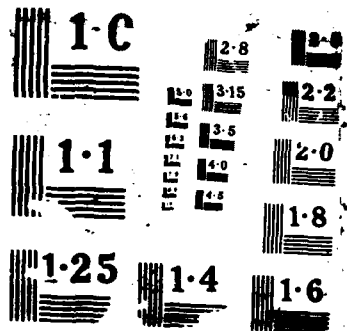
RD-A189 367

ACOUSTIC RADIATION FROM LINE- AND POINT-LOADED PLATES: 2/2
UNIFORMLY ASYMPTOT. (U) PENNSYLVANIA STATE UNIV
UNIVERSITY PARK APPLIED RESEARCH LAB. H Y HSU ET AL.

UNCLRSSIFIED NOV 87 ARL/PSU/TR-87-810 N60024-85-C-6841 F/G 20/1 NL

6





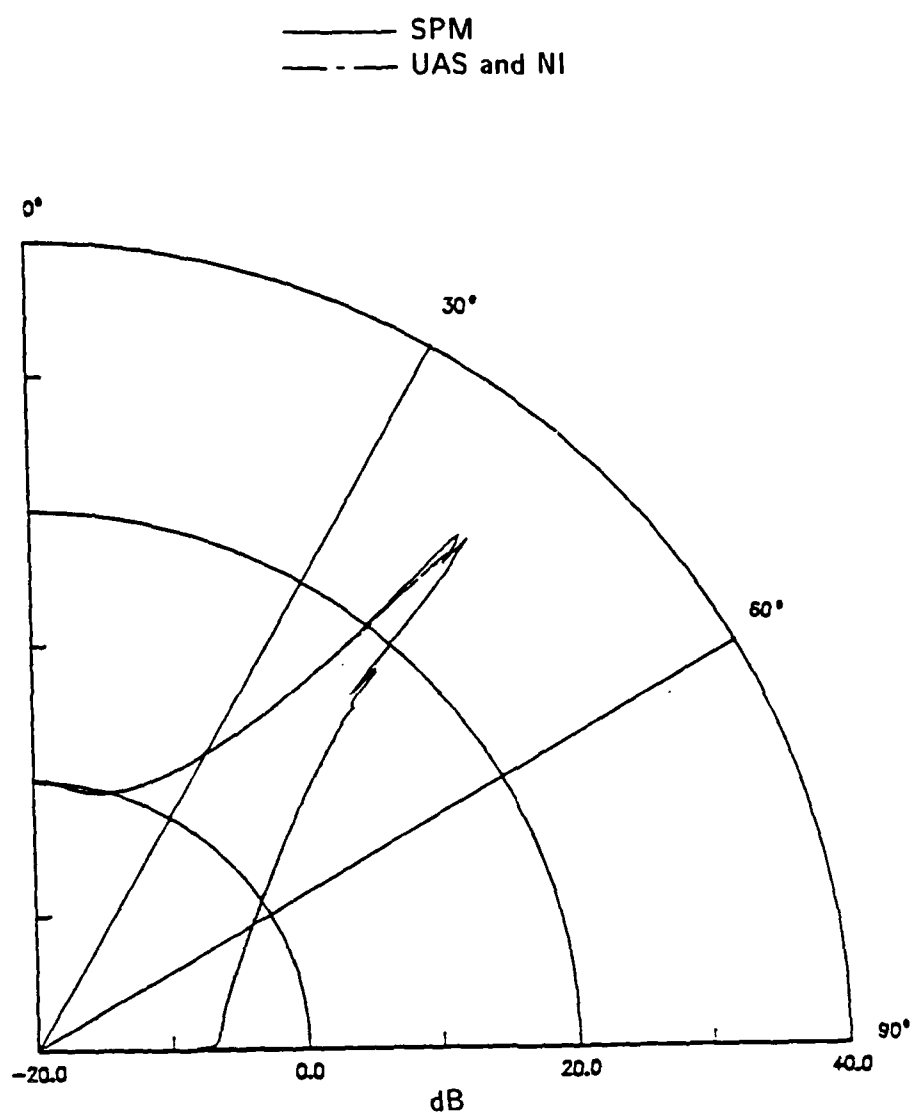


Figure 23 Normalized directivity function for a line-excited fluid-loaded steel plate. $k_0 r = 10^4$, $\Omega = 5.0$.

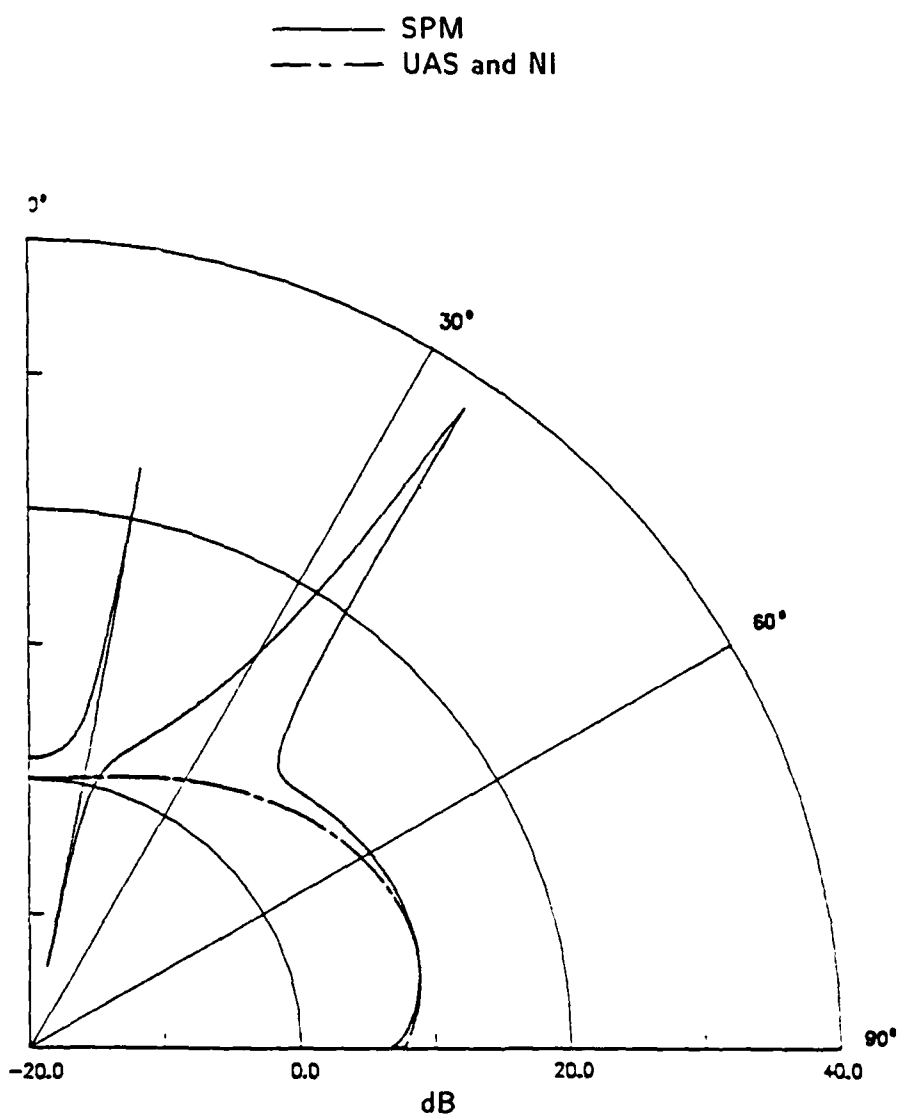


Figure 24 Normalized directivity function for a line-excited fluid-loaded steel plate. $k_0 r = 10$. $\Omega = 10.0$.

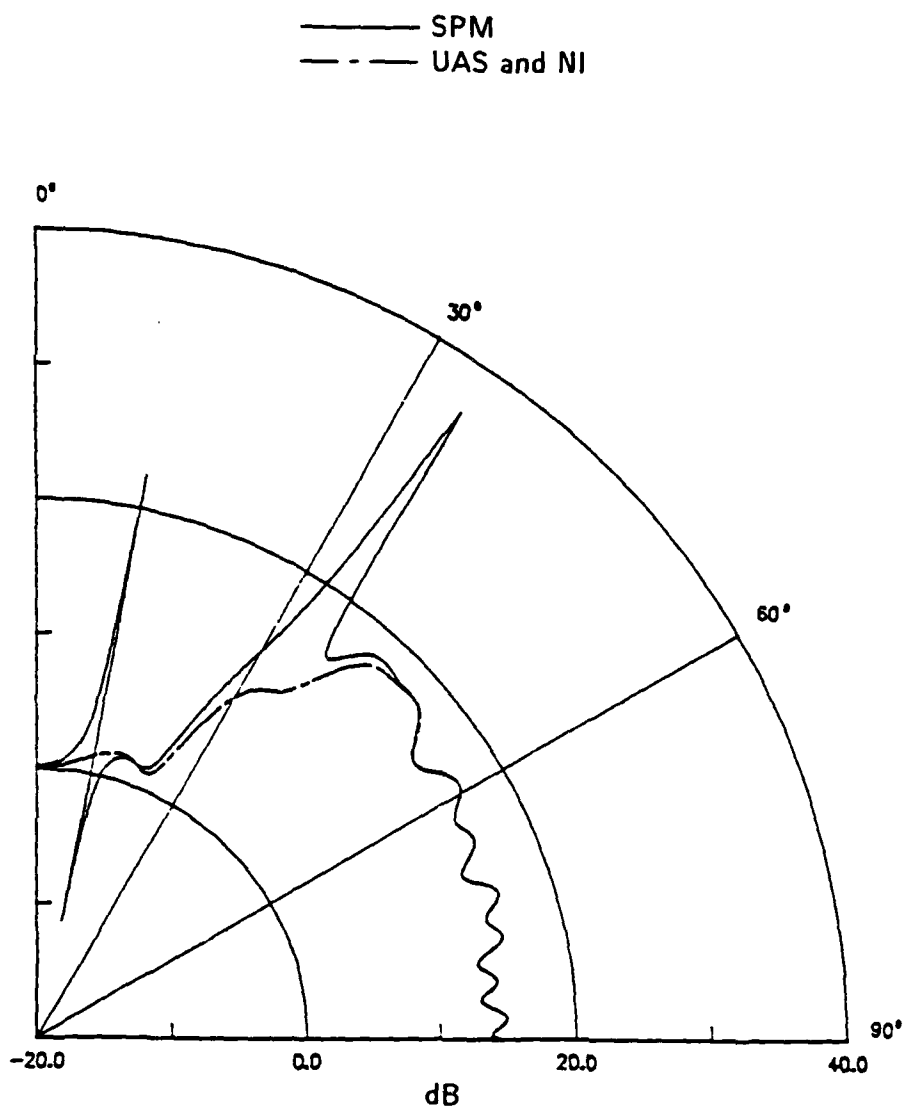


Figure 25 Normalized directivity function for a line-excited fluid-loaded steel plate. $k_0 r = 10^2$, $\Omega = 10.0$.

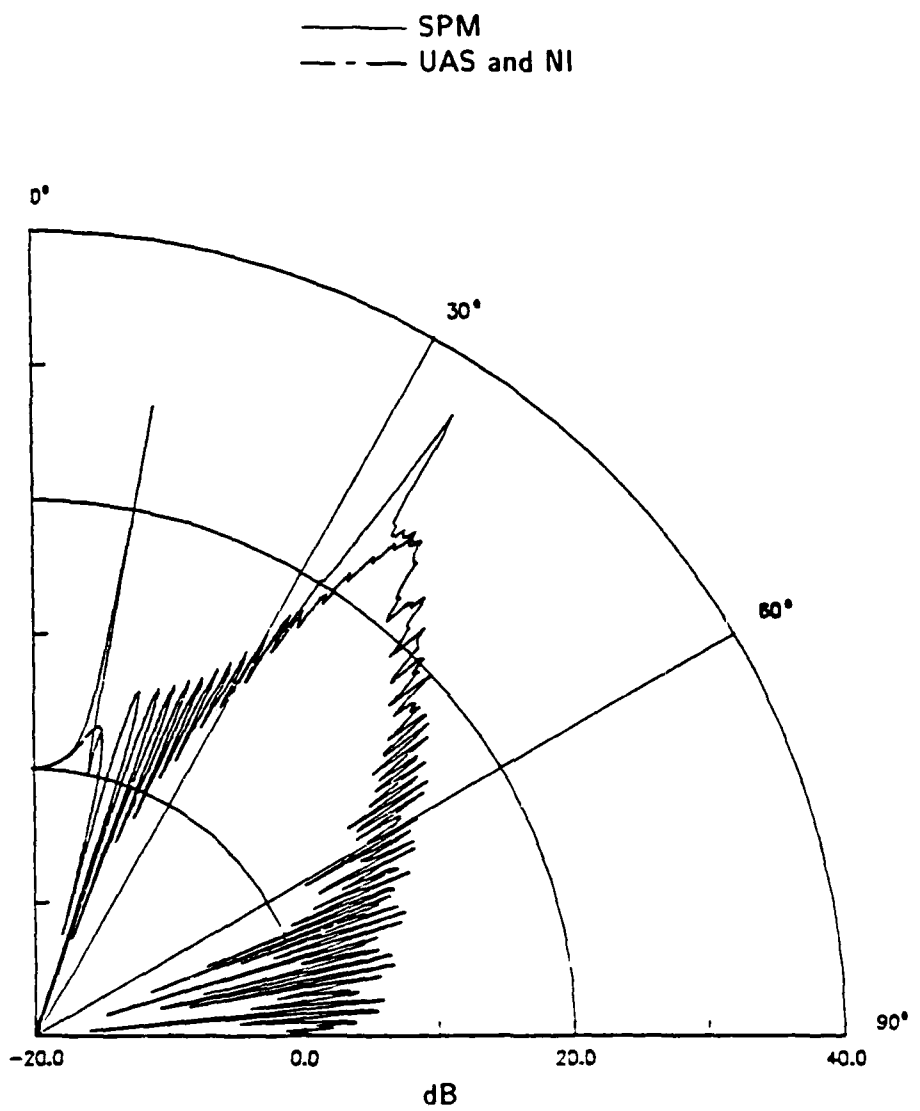


Figure 26 Normalized directivity function for a line-excited fluid-loaded steel plate. $k_0 r = 10^3$, $\Omega = 10.0$.

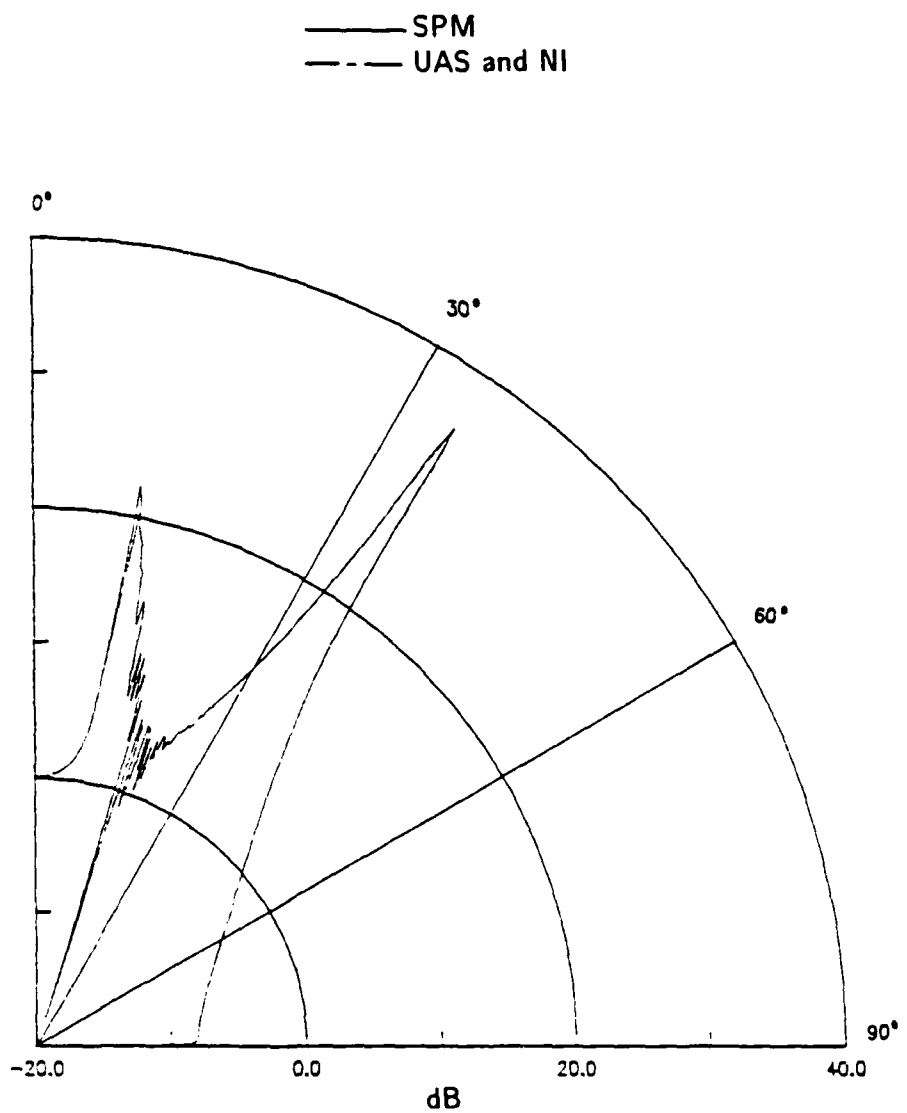


Figure 27 Normalized directivity function for a line-excited fluid-loaded steel plate. $k_0 r = 10^5$. $\Omega = 10.0$.

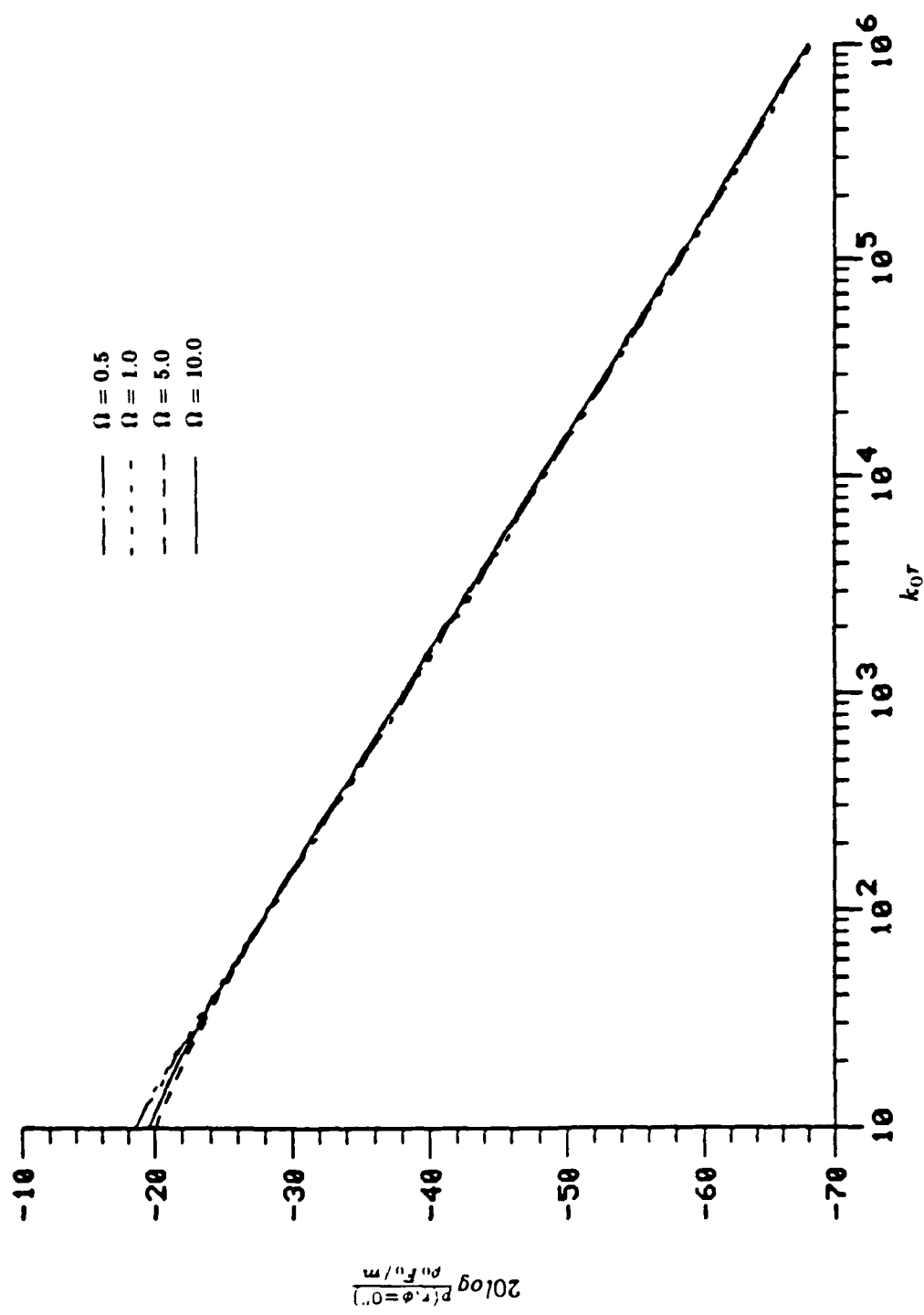


Figure 28 Radiated pressure from a line-excited steel plate. $\phi = 0^\circ$.

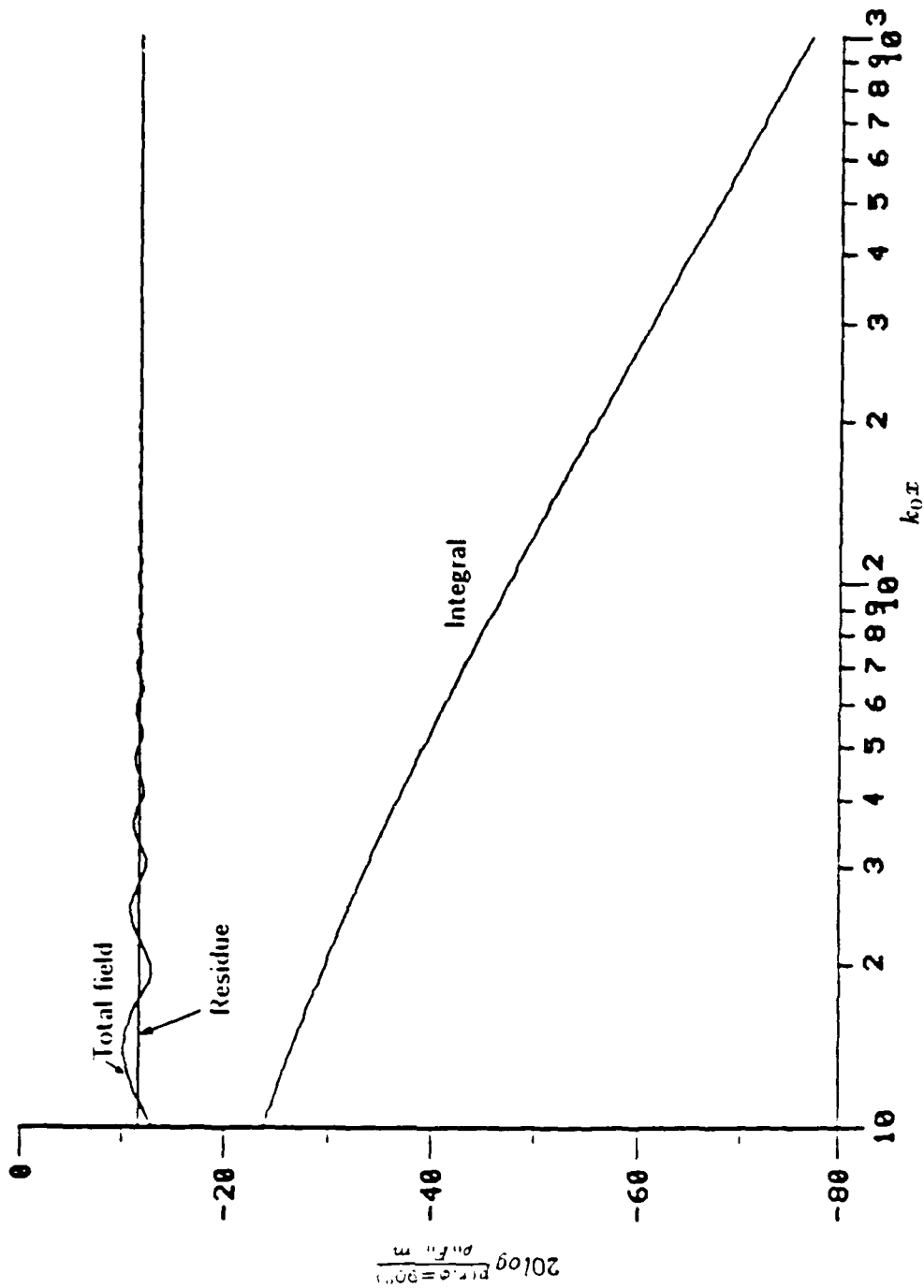


Figure 29 Grazing pressure field from a line-excited plate. $\Omega = 0.5$.

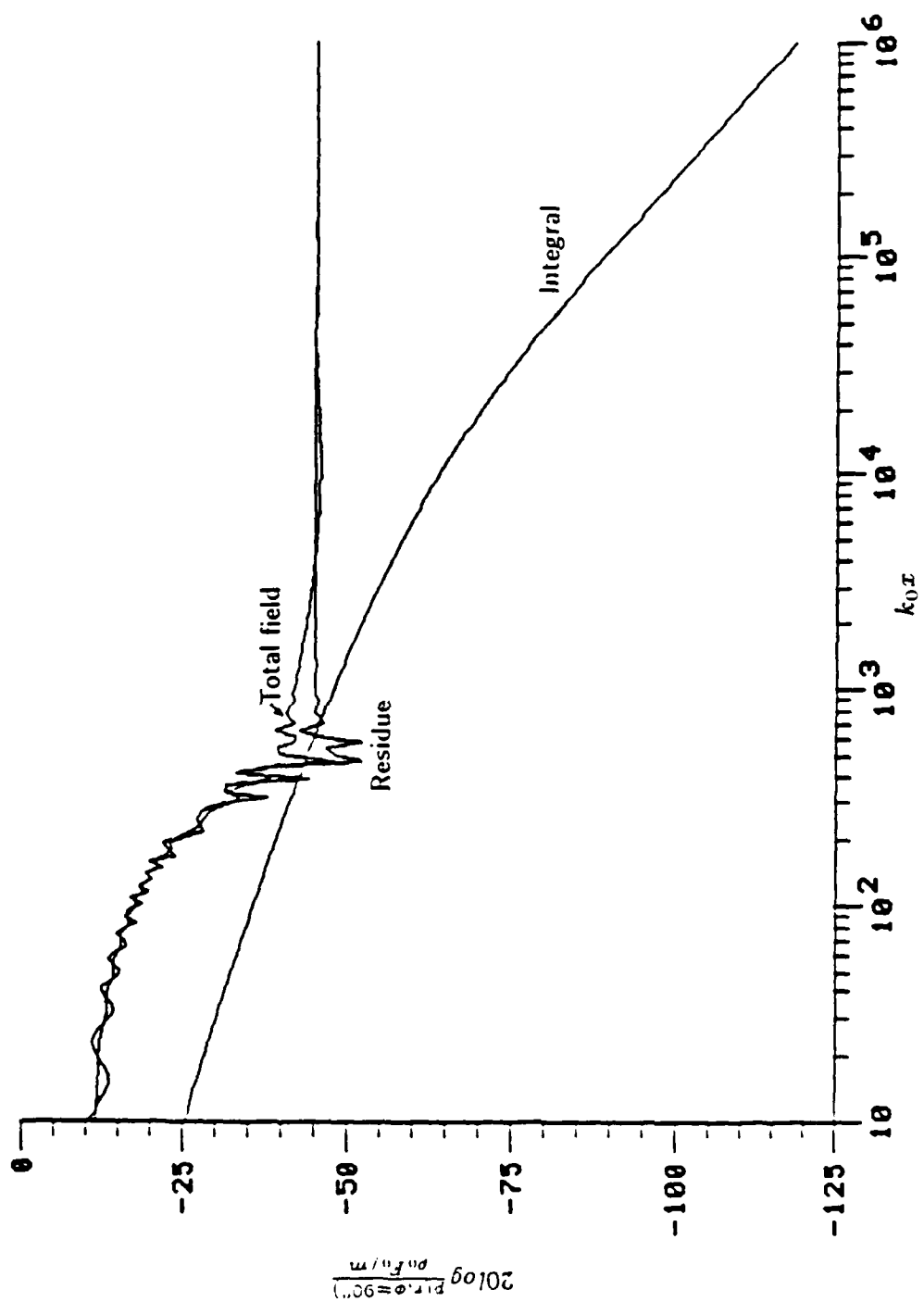


Figure 30 Grazing pressure field from a line-excited plate. $\Omega = 5.0$.

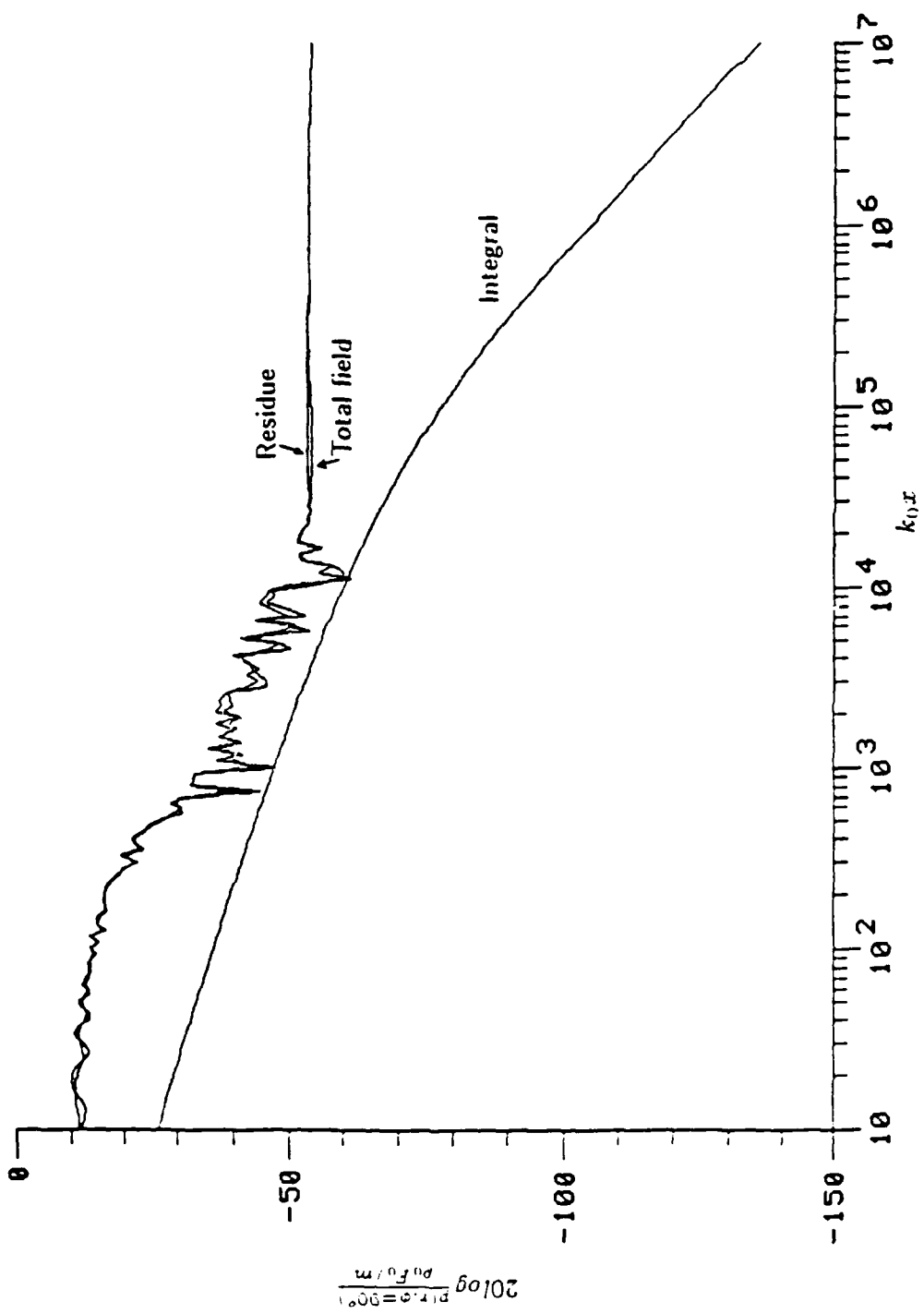


Figure 31 Grazing pressure field from a line-excited plate. $\Omega = 10.0$.

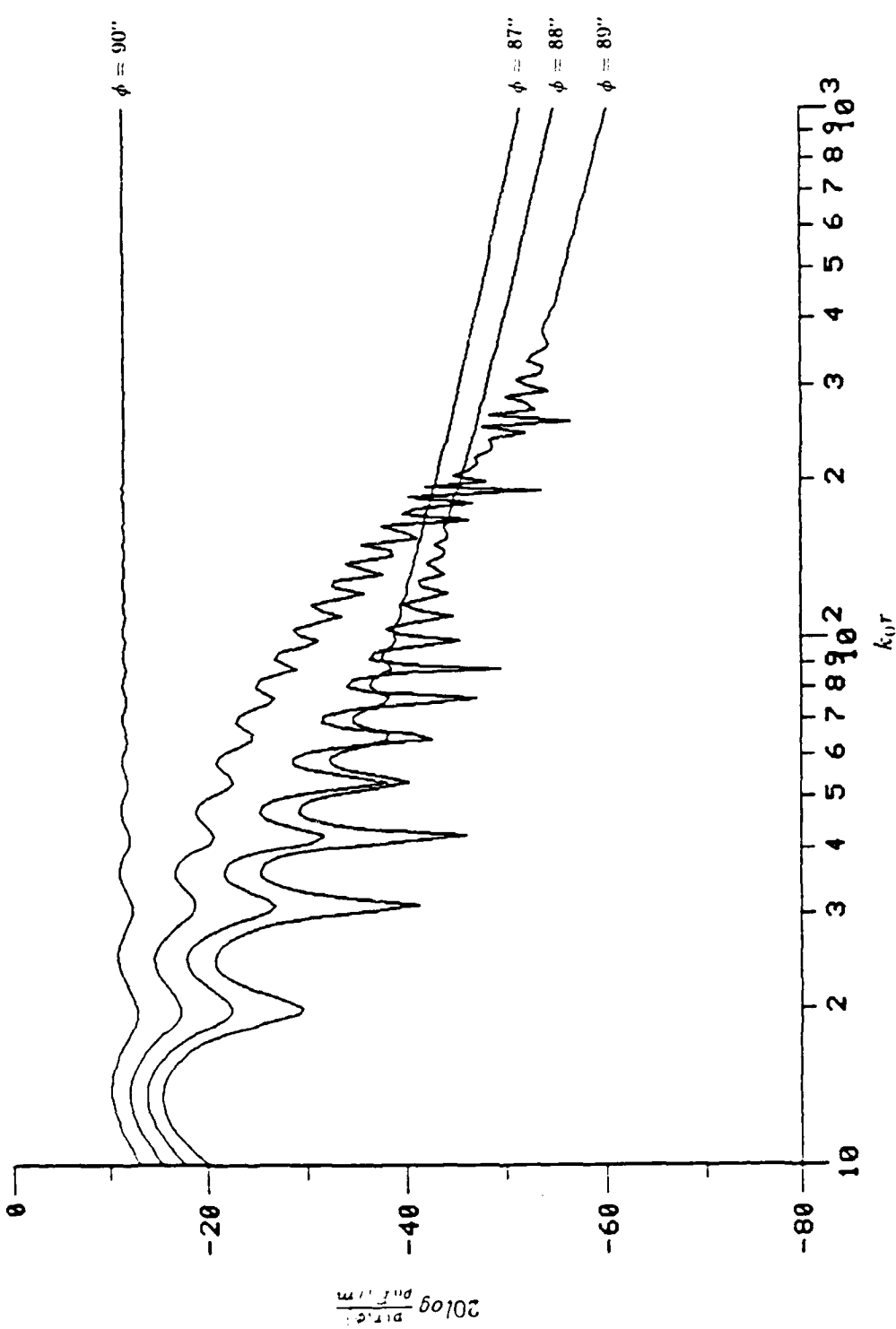


Figure 32 Nearfield pressure from a line-excited plate, $\Omega = 0.5$.

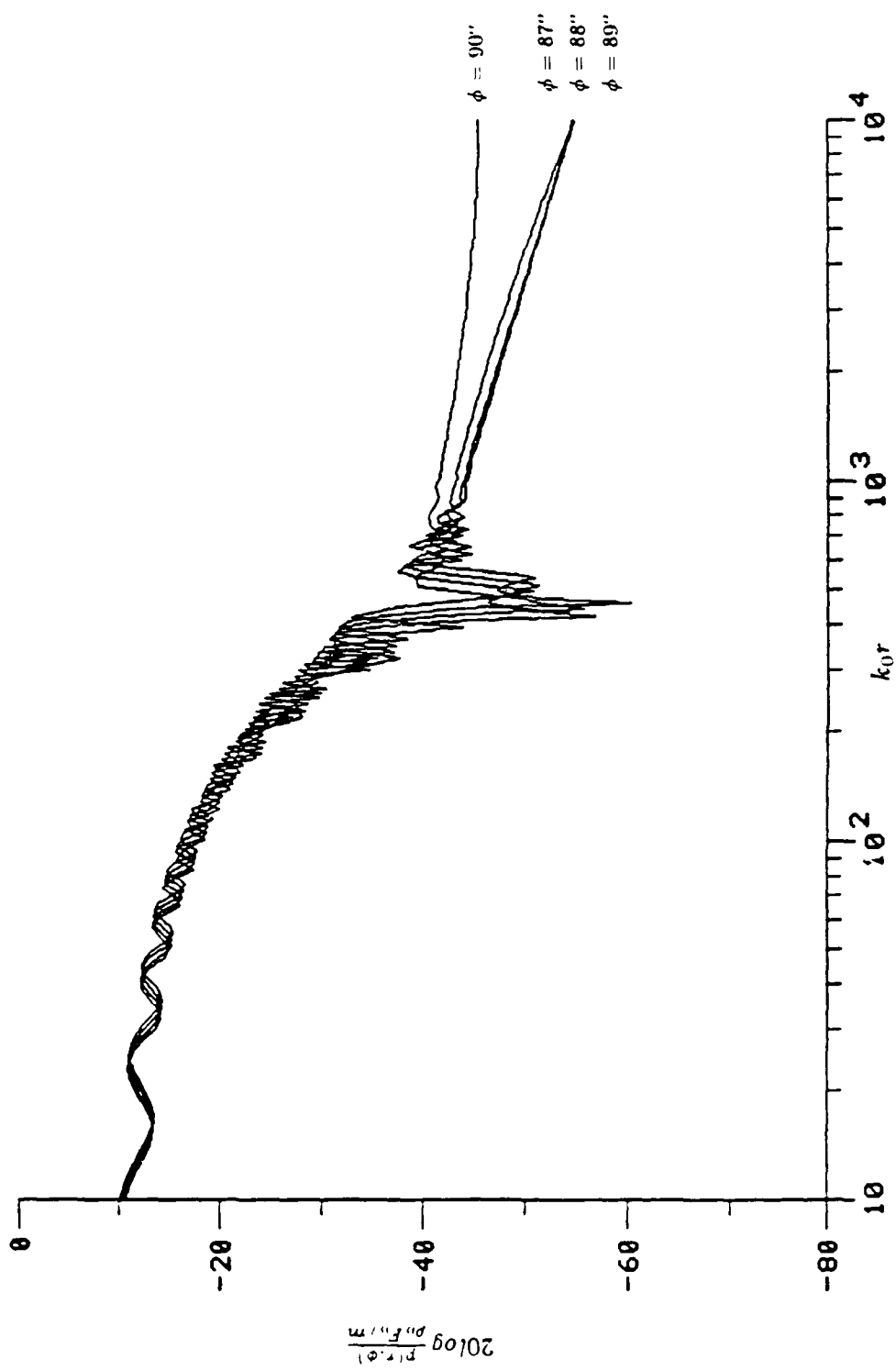


Figure 33 Nearfield pressure from a line-excited plate, $\Omega = 5.0$.

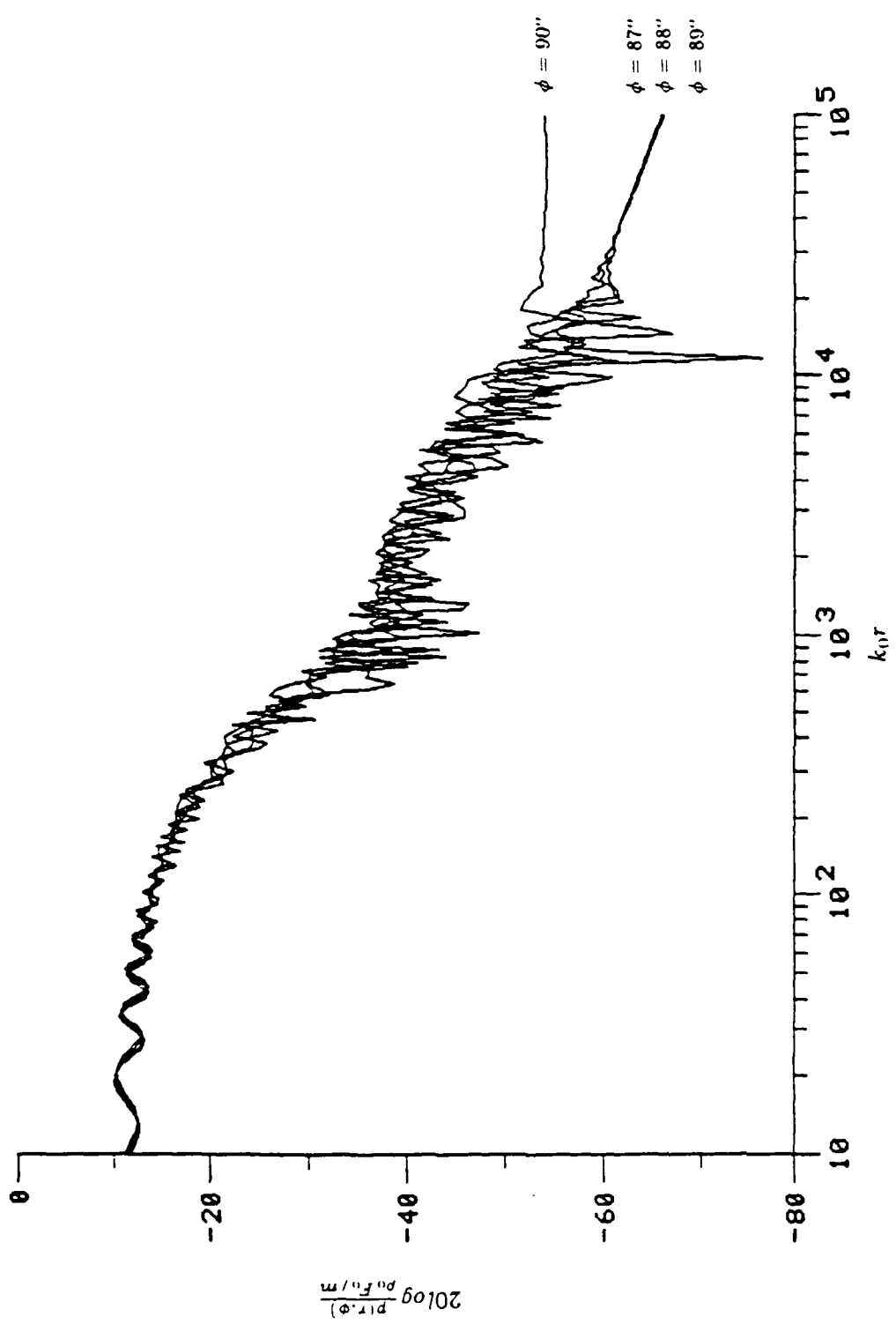


Figure 34 Nearfield pressure from a line-excited plate, $\Omega = 10.0$.

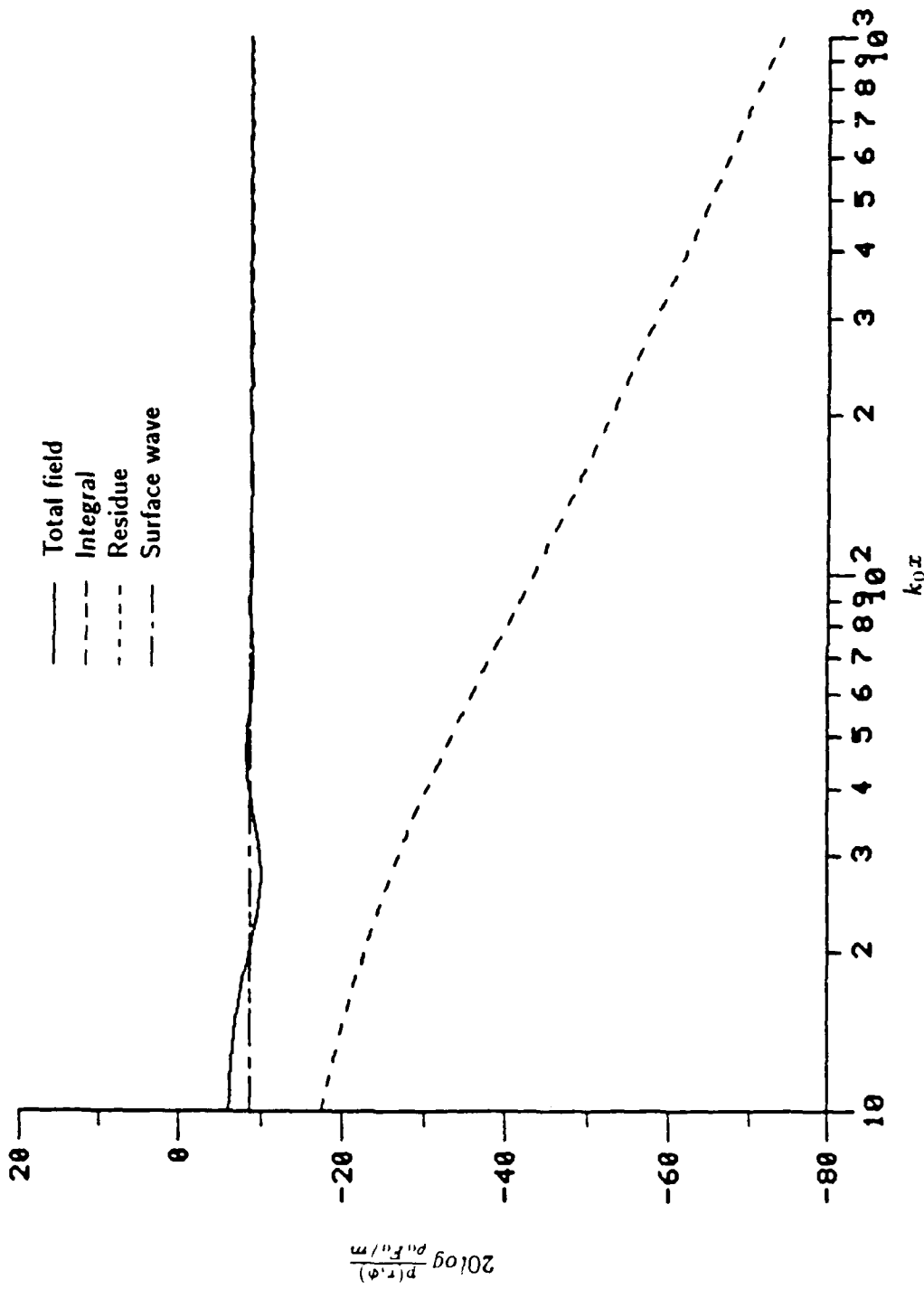


Figure 35 Radiated pressure from a line-excited steel plate
at $\Omega = 1.0$ and $z = 0.01\lambda$.

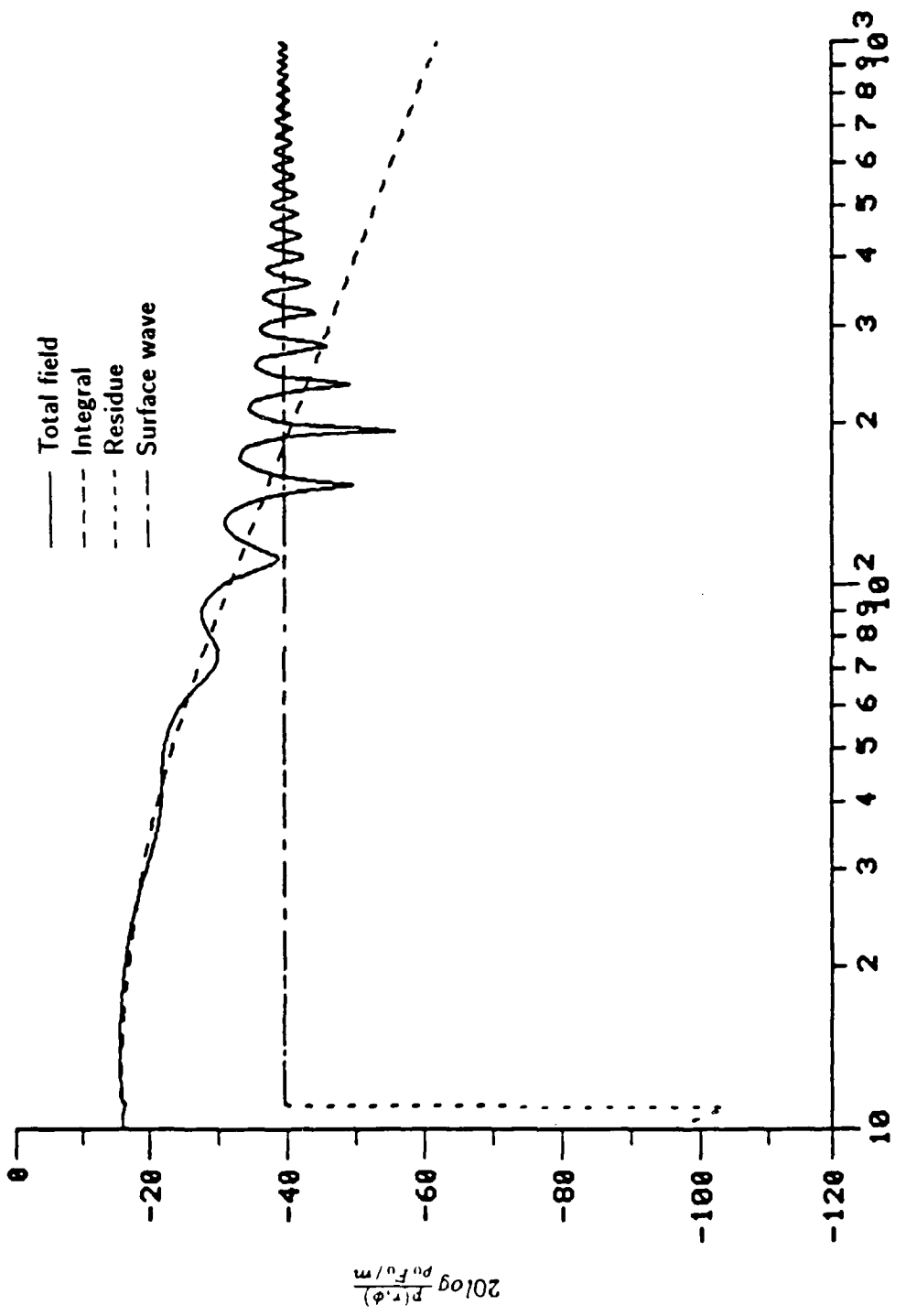


Figure 36 Radiated pressure from a line-excited steel plate
at $\Omega = 1.0$ and $z = 1.0\lambda$.

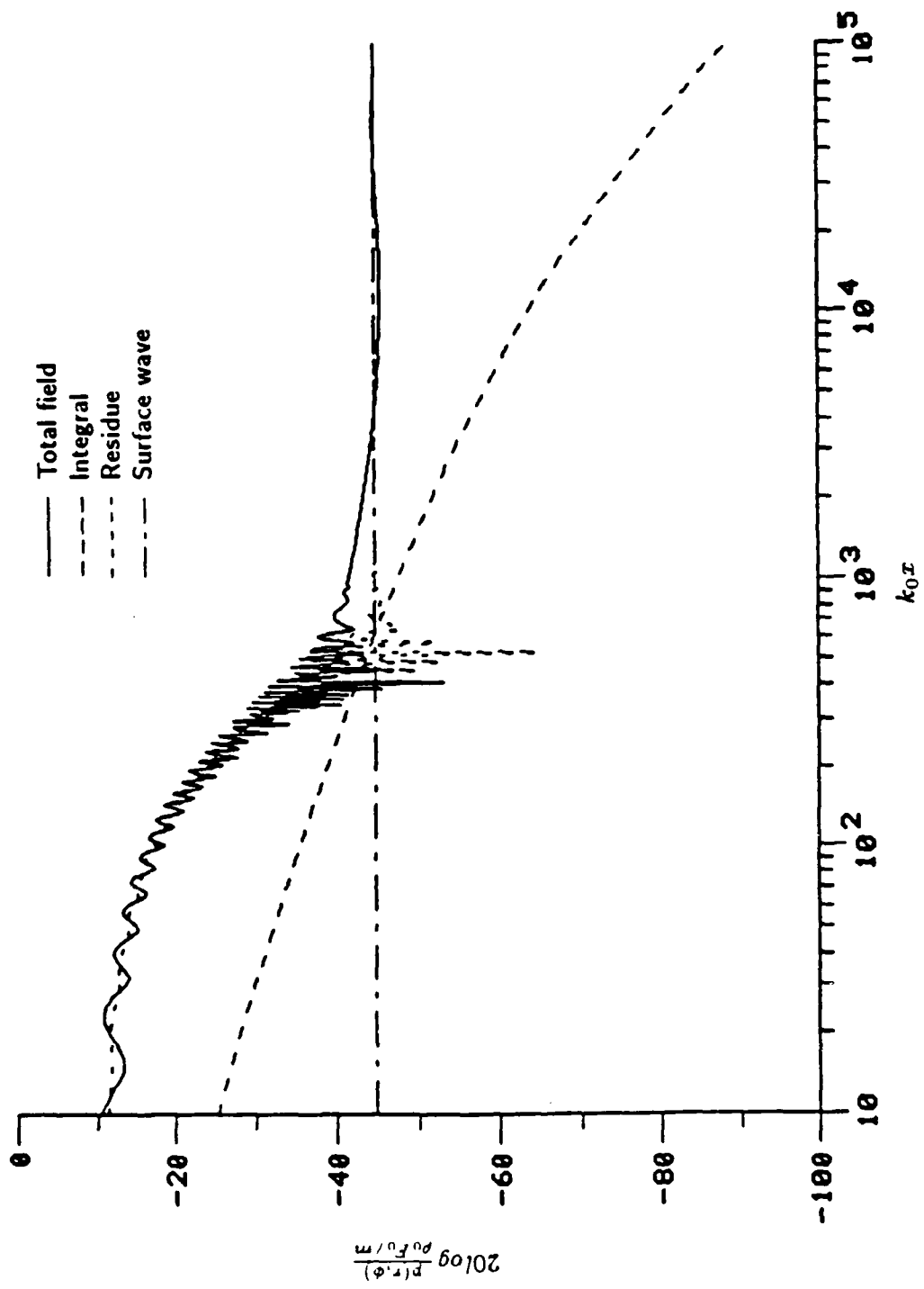


Figure 37 Radiated pressure from a line-excited steel plate
at $\Omega = 5.0$ and $z = 0.01\lambda$.

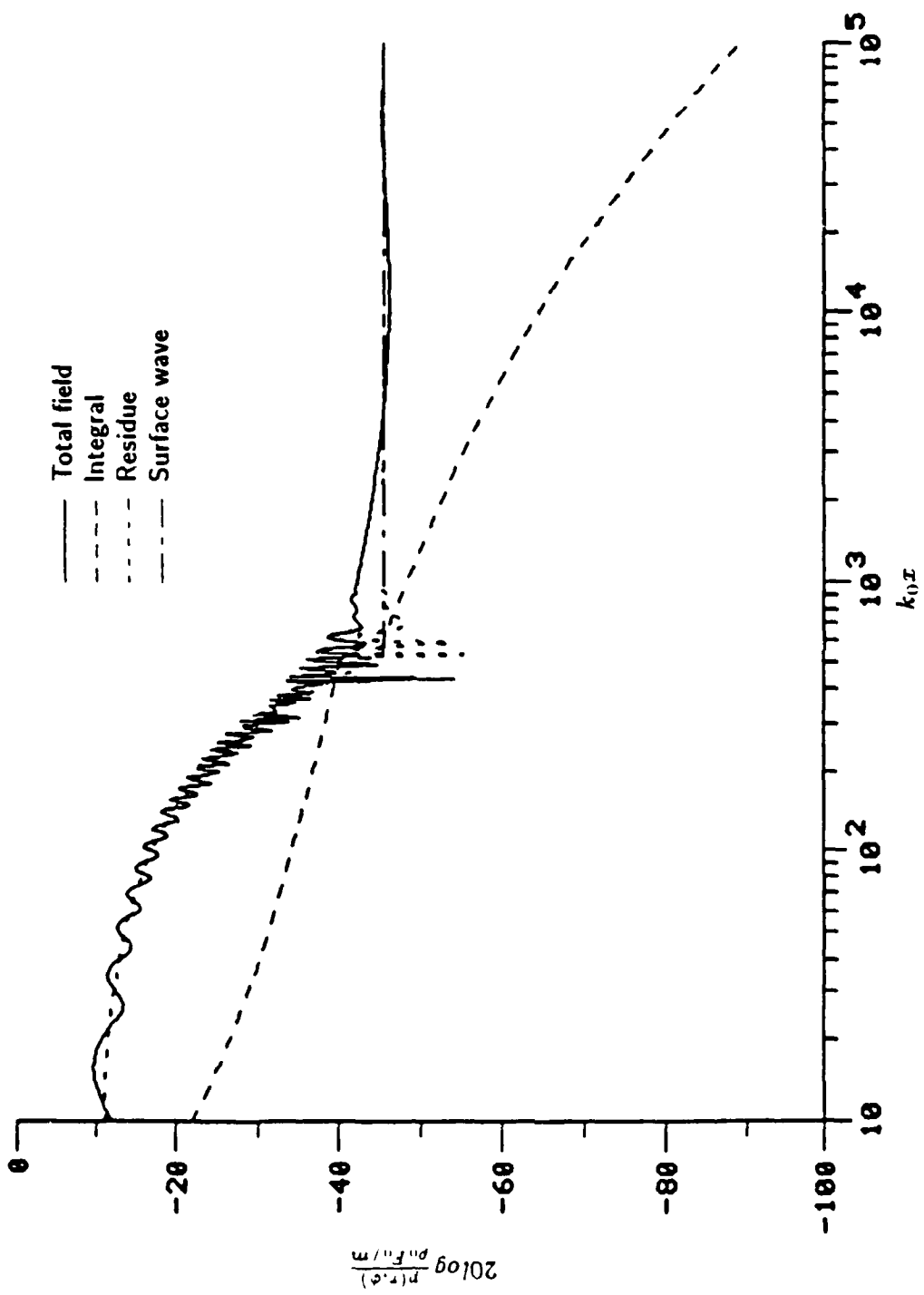


Figure 38 Radiated pressure from a line-excited steel plate
at $\Omega = 5.0$ and $z = 1.0\lambda$.

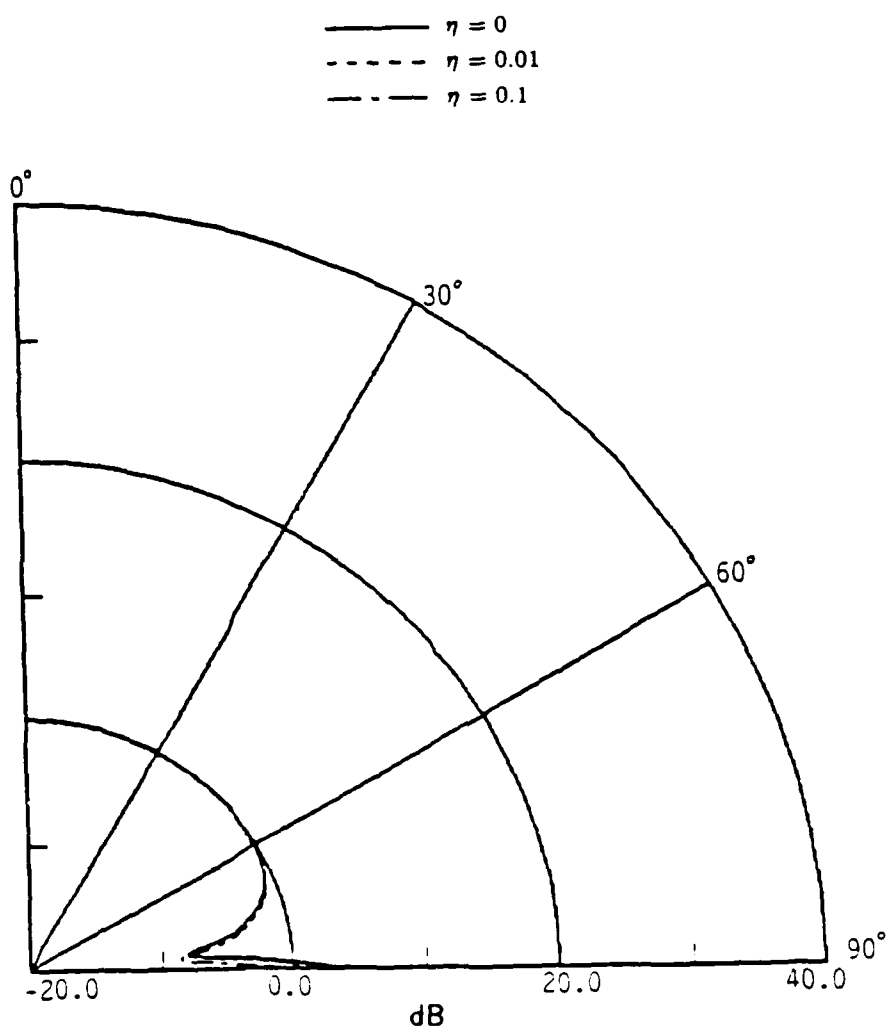
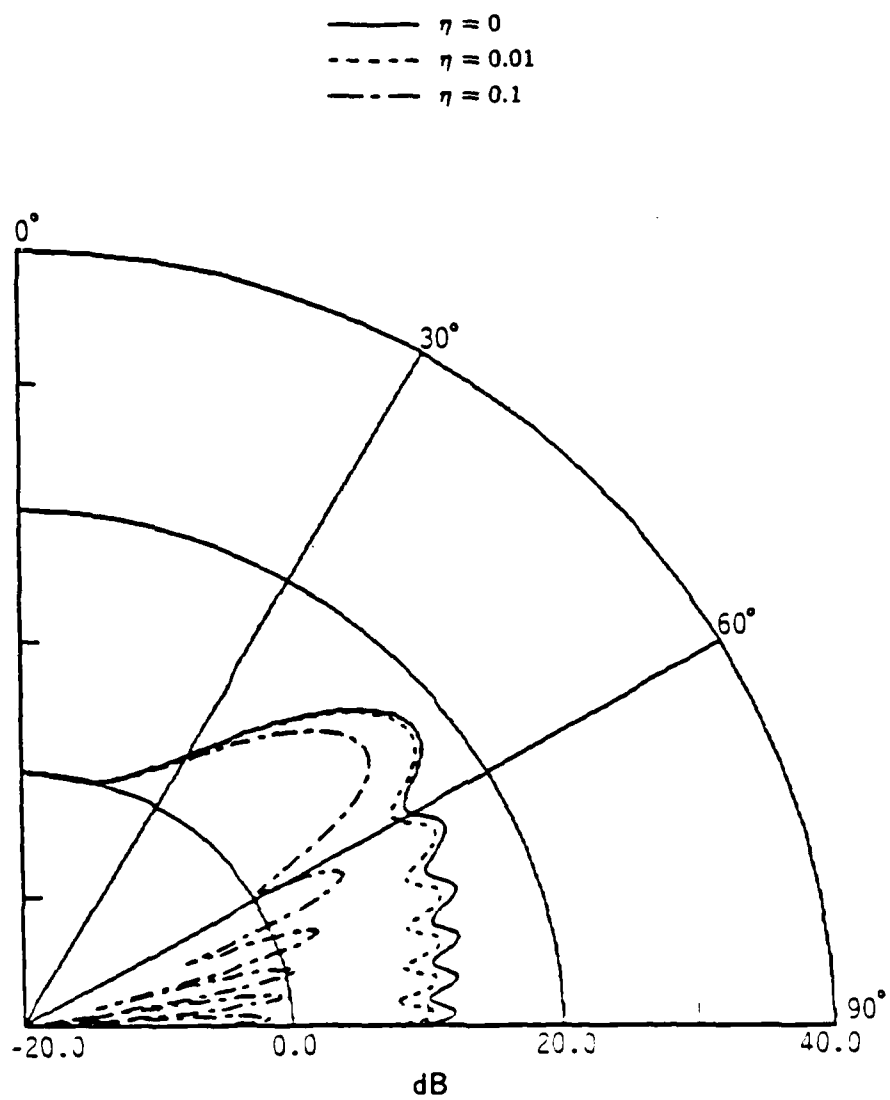
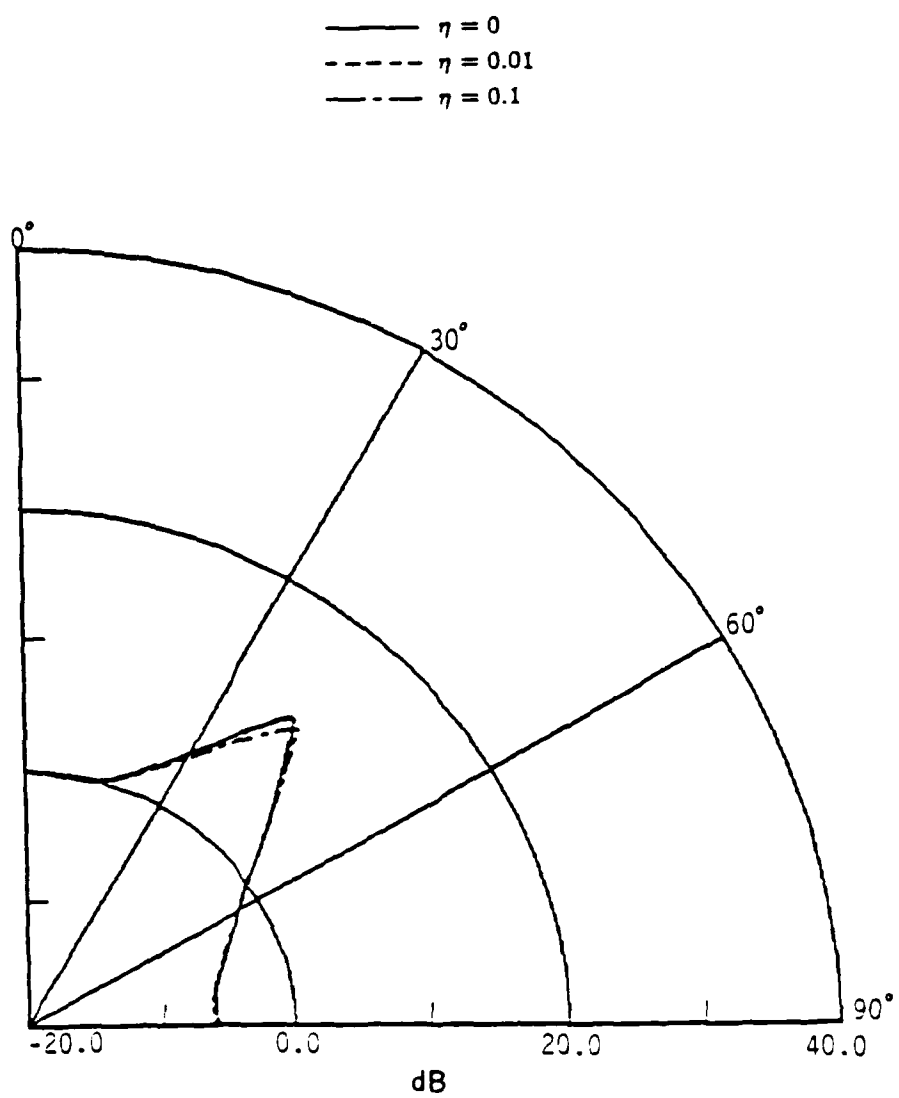


Figure 39 Normalized directivity function for a line-excited plate with structural damping, $k_0 r = 10$, $\Omega = 0.5$.



a. Total acoustic pressure.

Figure 40 Normalized directivity function for a line-excited plate with structural damping, $k_x r = 10^2$, $\Omega = 5.0$.



b. Integral along SDP only.

Figure 40 Continued

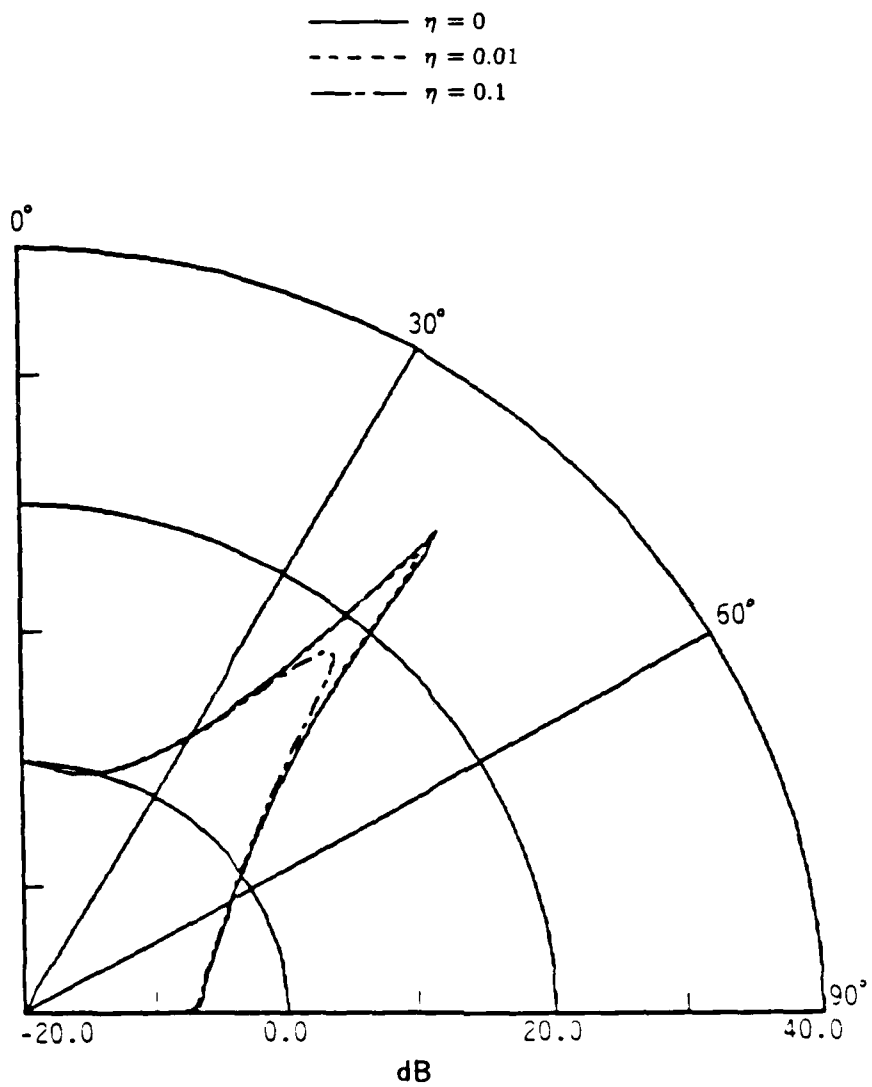


Figure 41 Normalized directivity function for a line-excited plate with structural damping. $k_0 r = 10^5$, $\Omega = 5.0$.

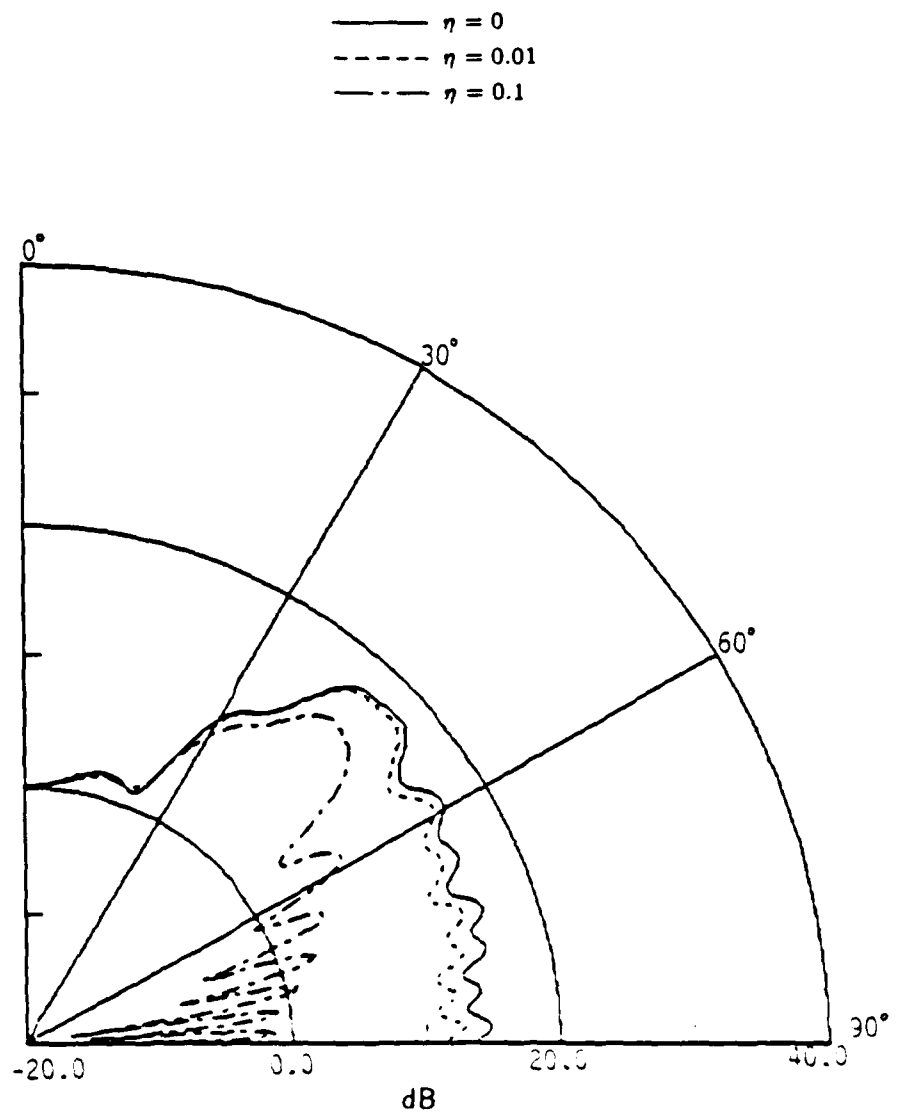


Figure 42 Normalized directivity function for a line-excited plate with structural damping. $k_0 r = 10^2$, $\Omega = 10.0$.

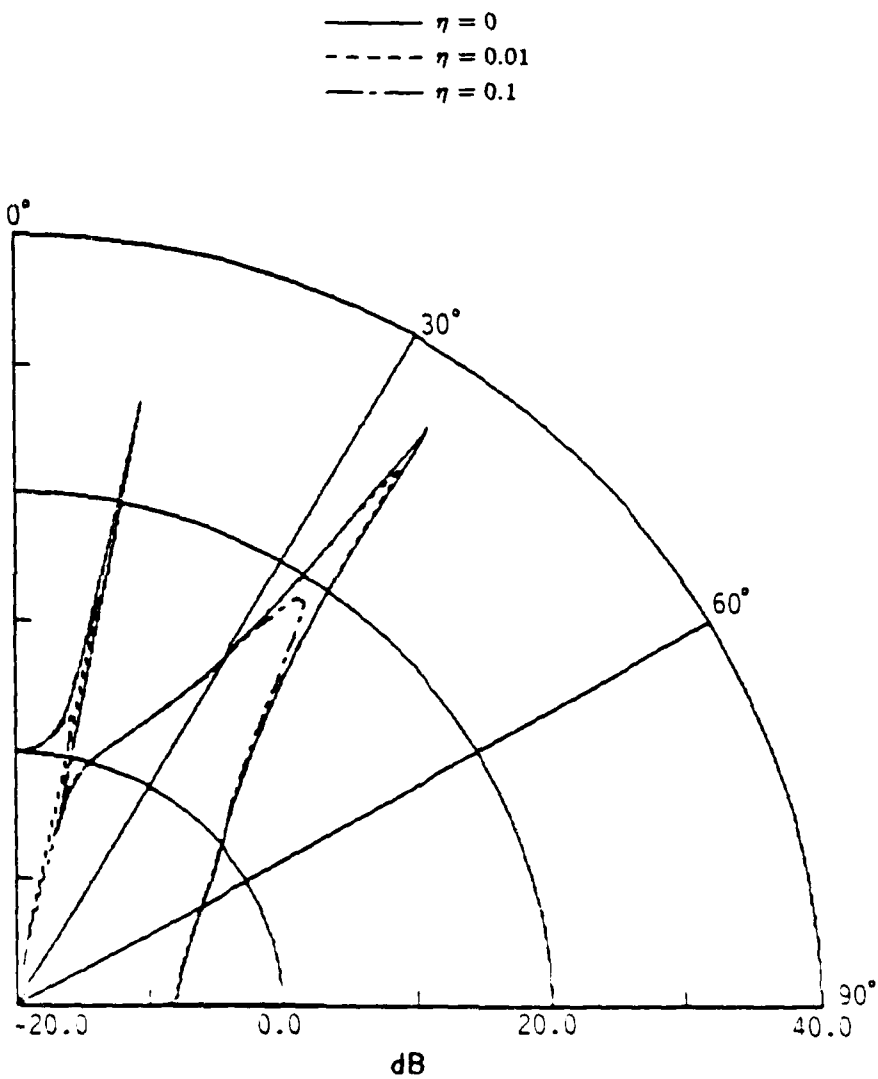


Figure 43 Normalized directivity function for a line-excited plate with structural damping. $k_0 r = 10^6$. $\Omega = 10.0$.

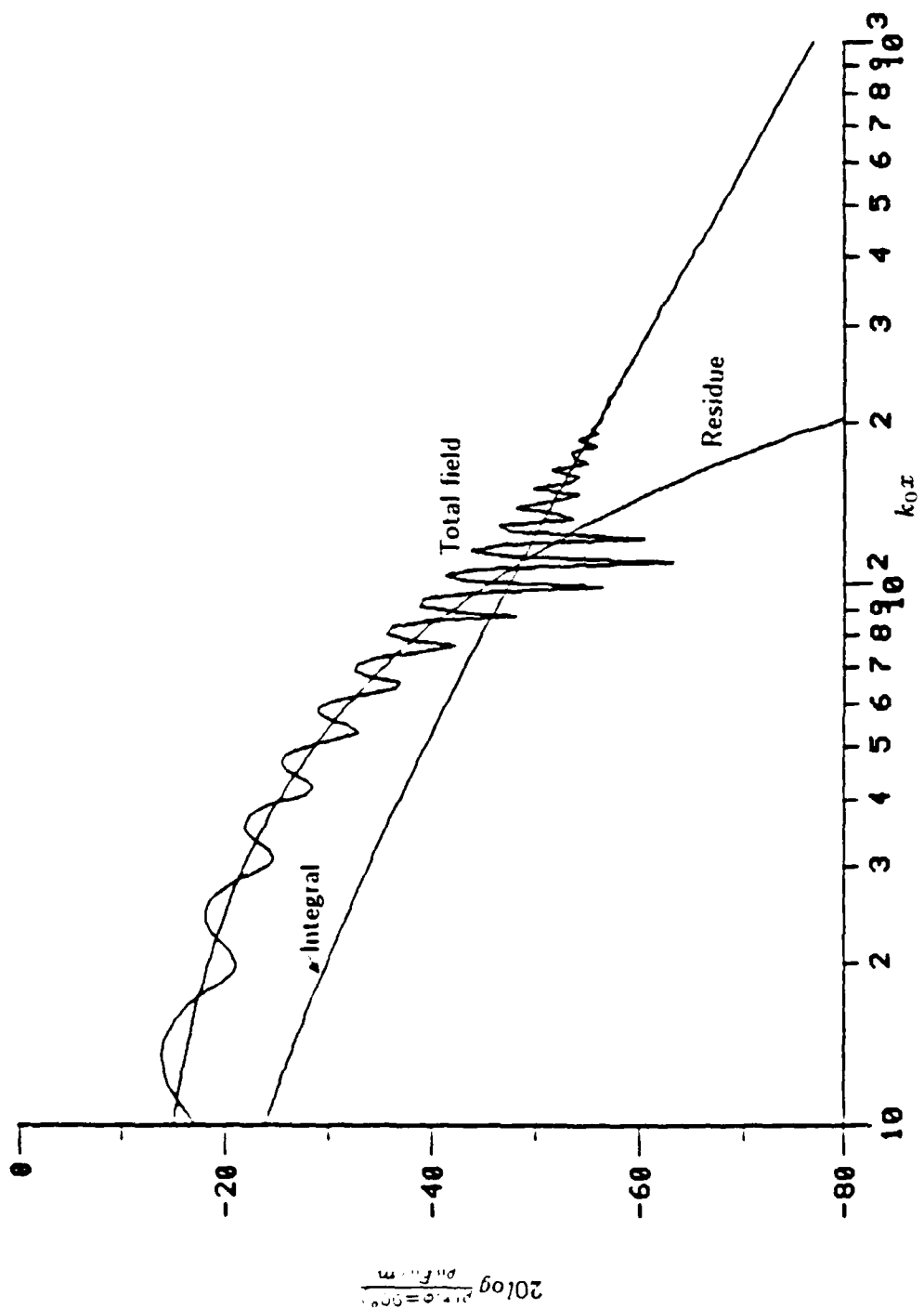


Figure 44 Grazing pressure field from a line-excited plate with structural damping. $\eta = 0.1$, $\Omega = 0.5$.

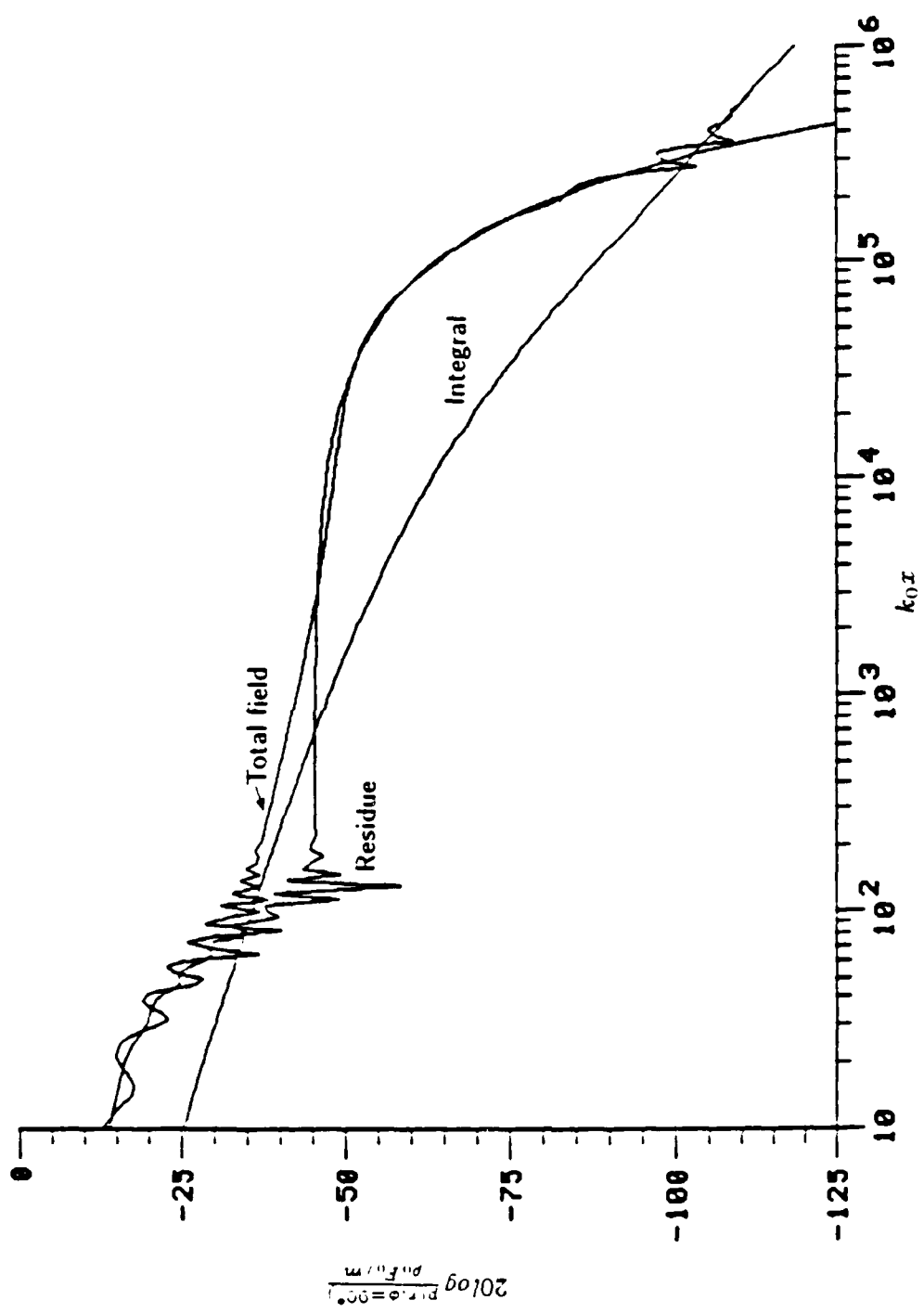


Figure 45 Grazing pressure field from a line-excited plate with structural damping. $\eta = 0$ to $\Omega = 5.0$.

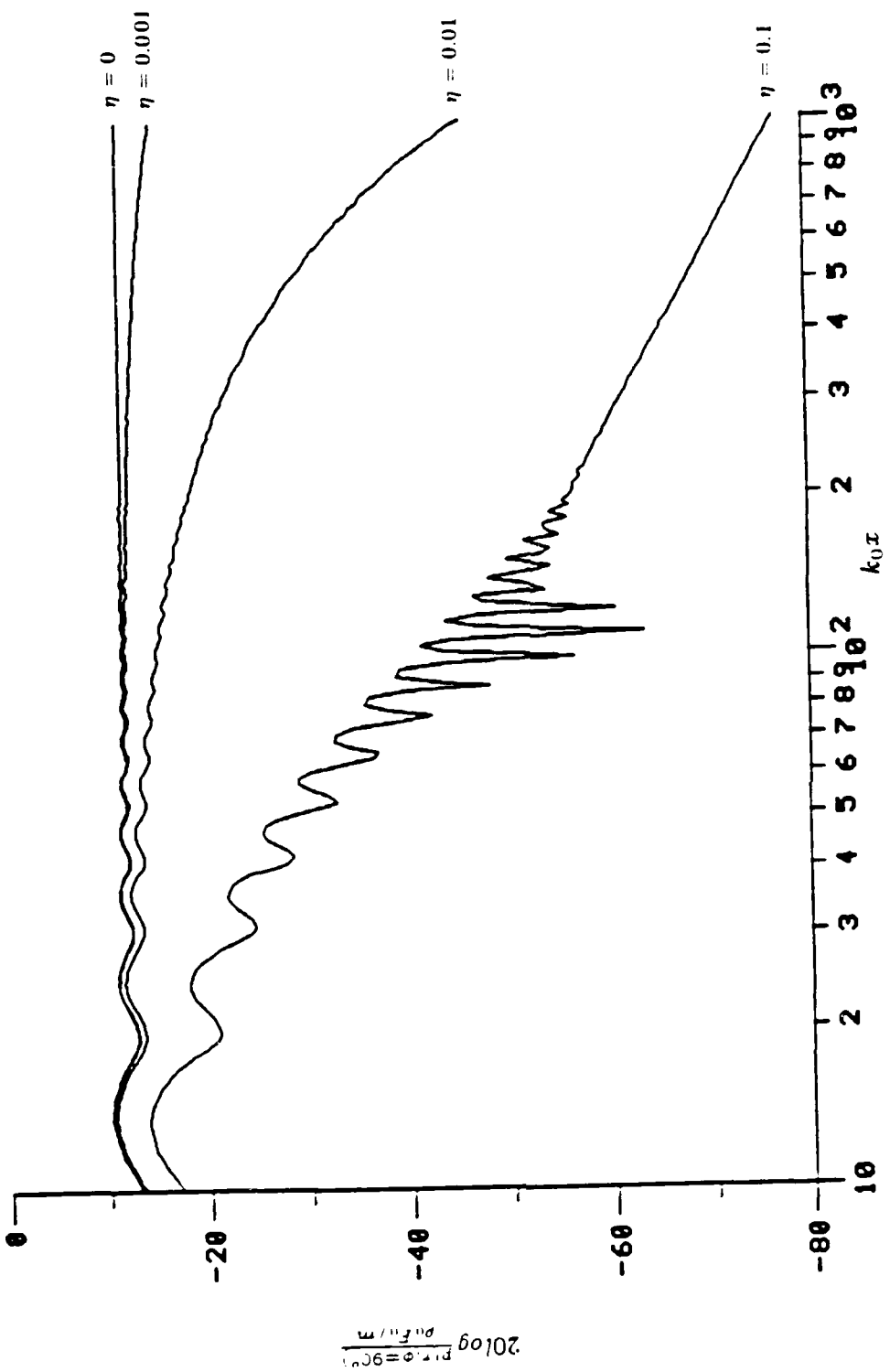


Figure 46 Grazing pressure field from a line-excited plate with structural damping. $\Omega = 0.5$.

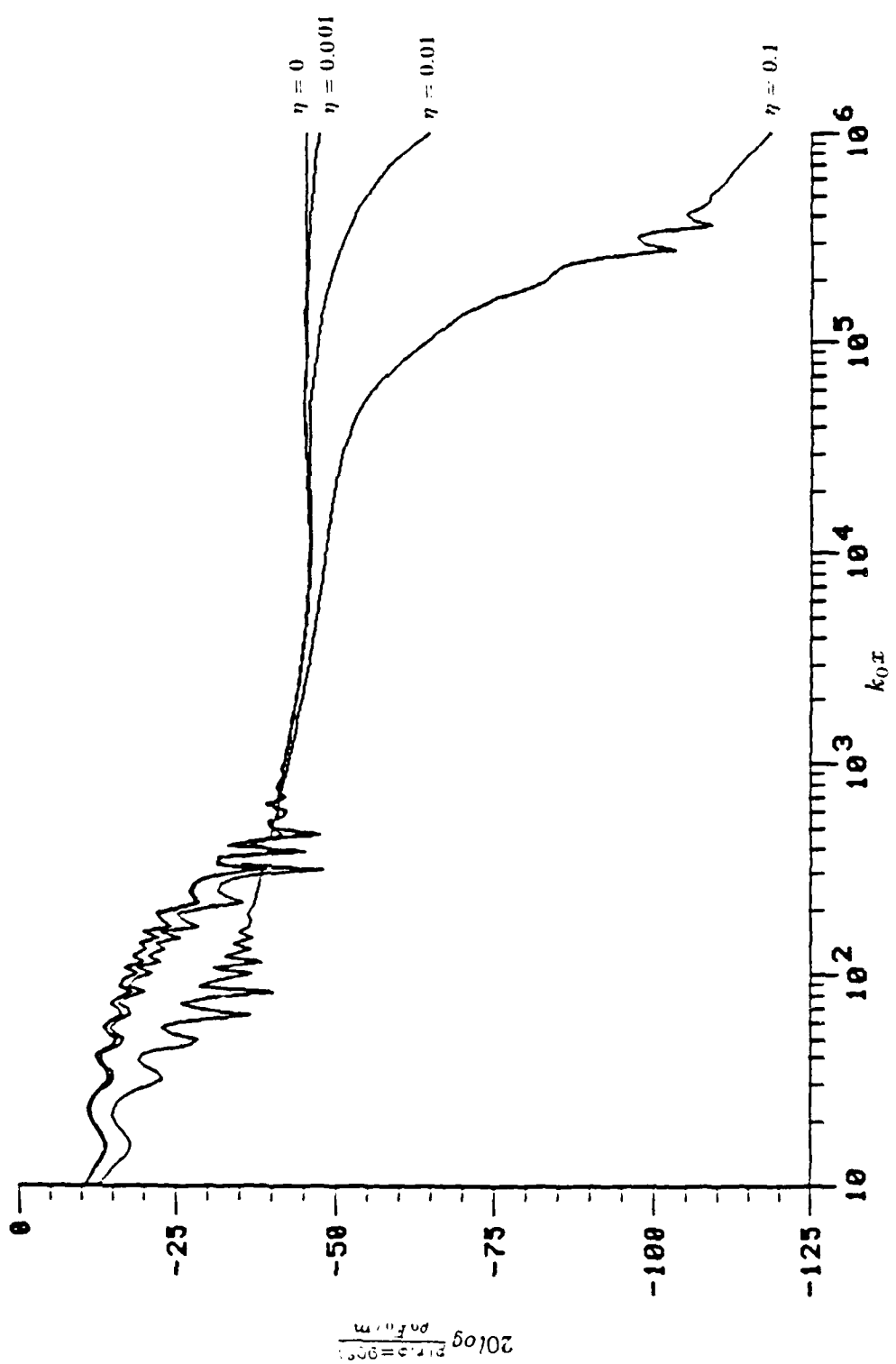


Figure 47 Grazing pressure field from a line-excited plate with structural damping. $\Omega = 5.0$.

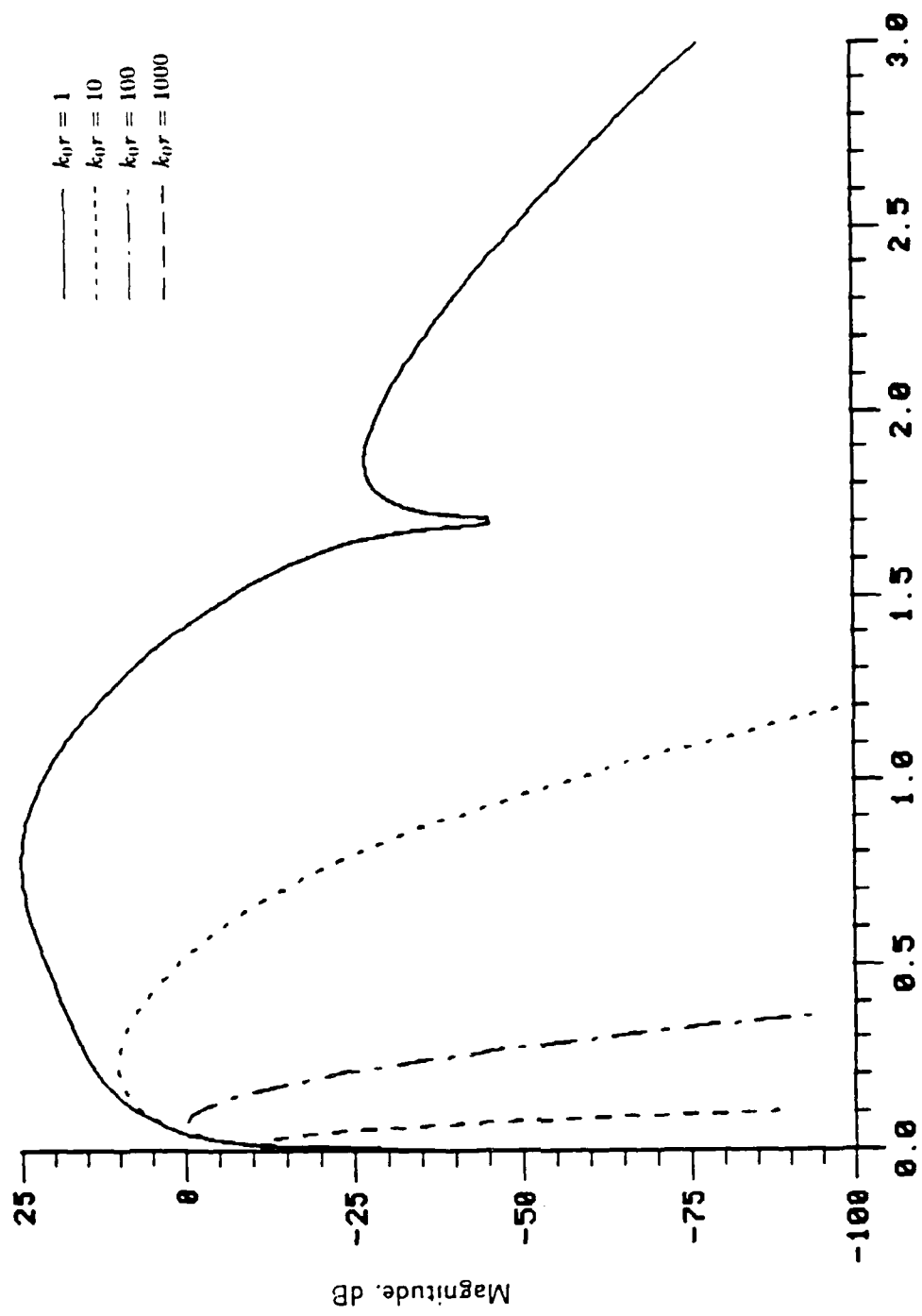


Figure 48 Magnitude of integrand along SDP-point-excited plate
at $\Omega = 1.0$ and $\phi = 0^\circ$.
 χ , distance from saddle point

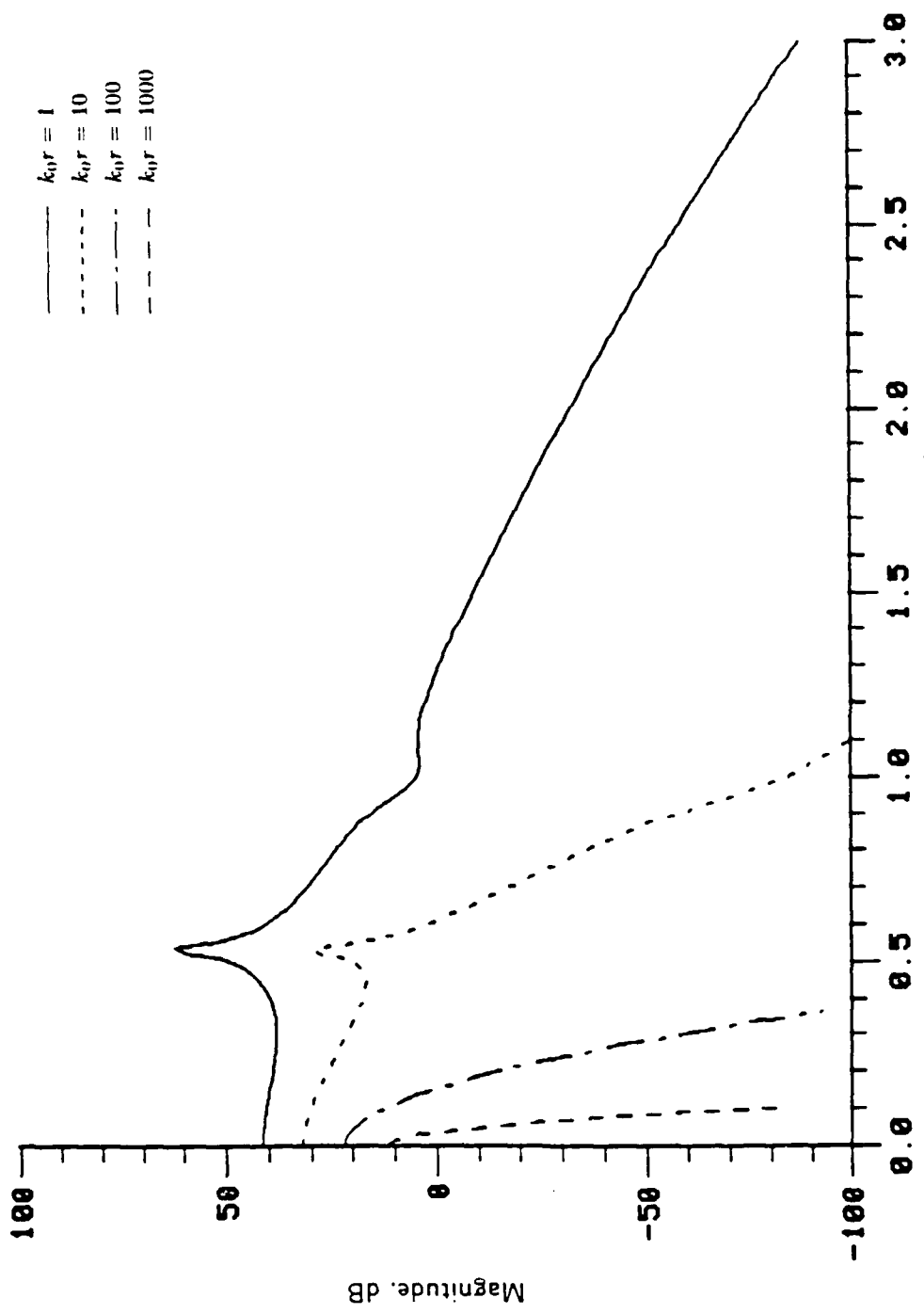


Figure 49 Magnitude of integrand along SOP- point-excited plate
at $\Omega = 1.0$ and $\phi = 60^\circ$.

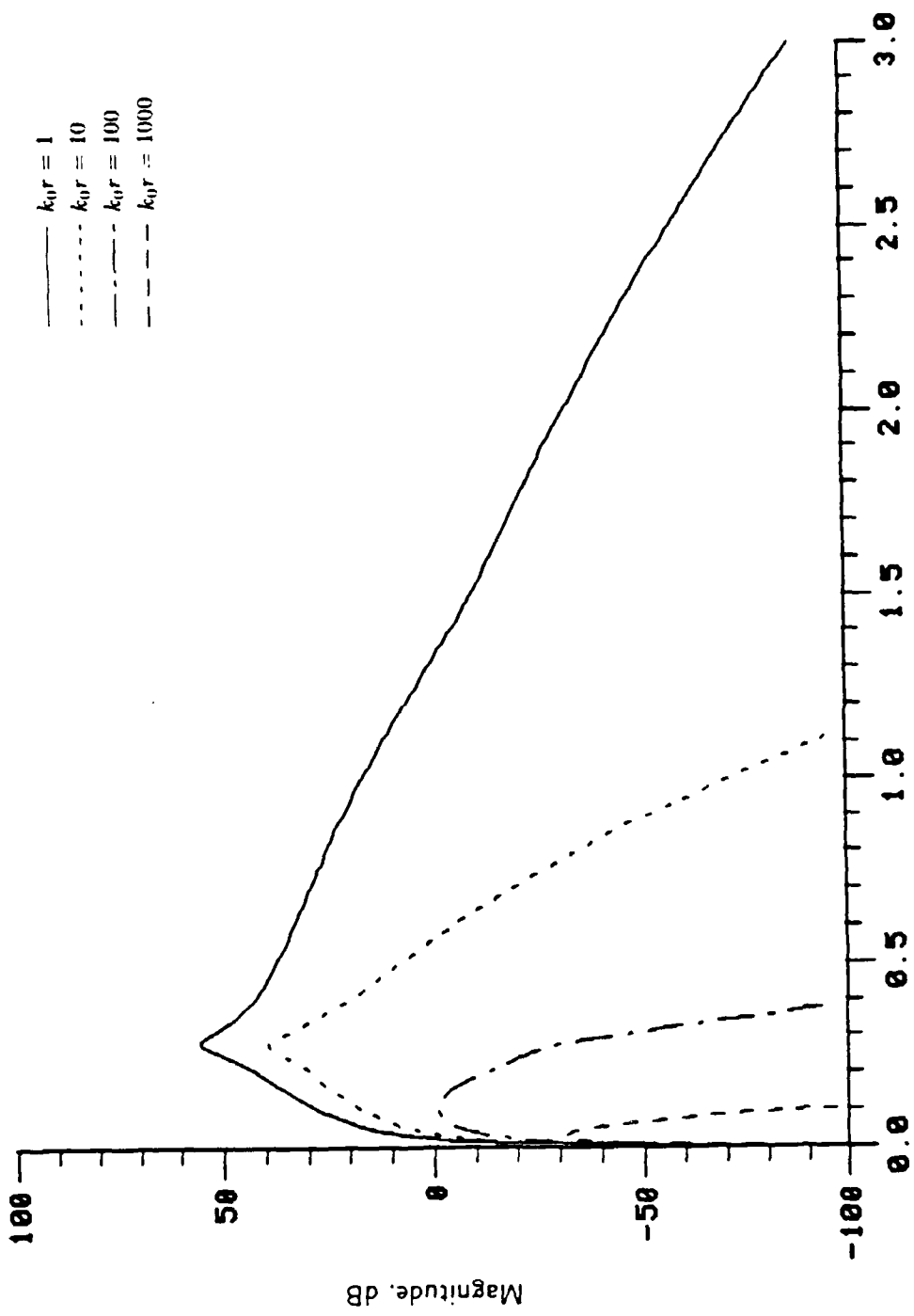


Figure 50 Magnitude of integrand along SDP-point-excited plate
at $\Omega = 1.0$ and $\phi = 90^\circ$.

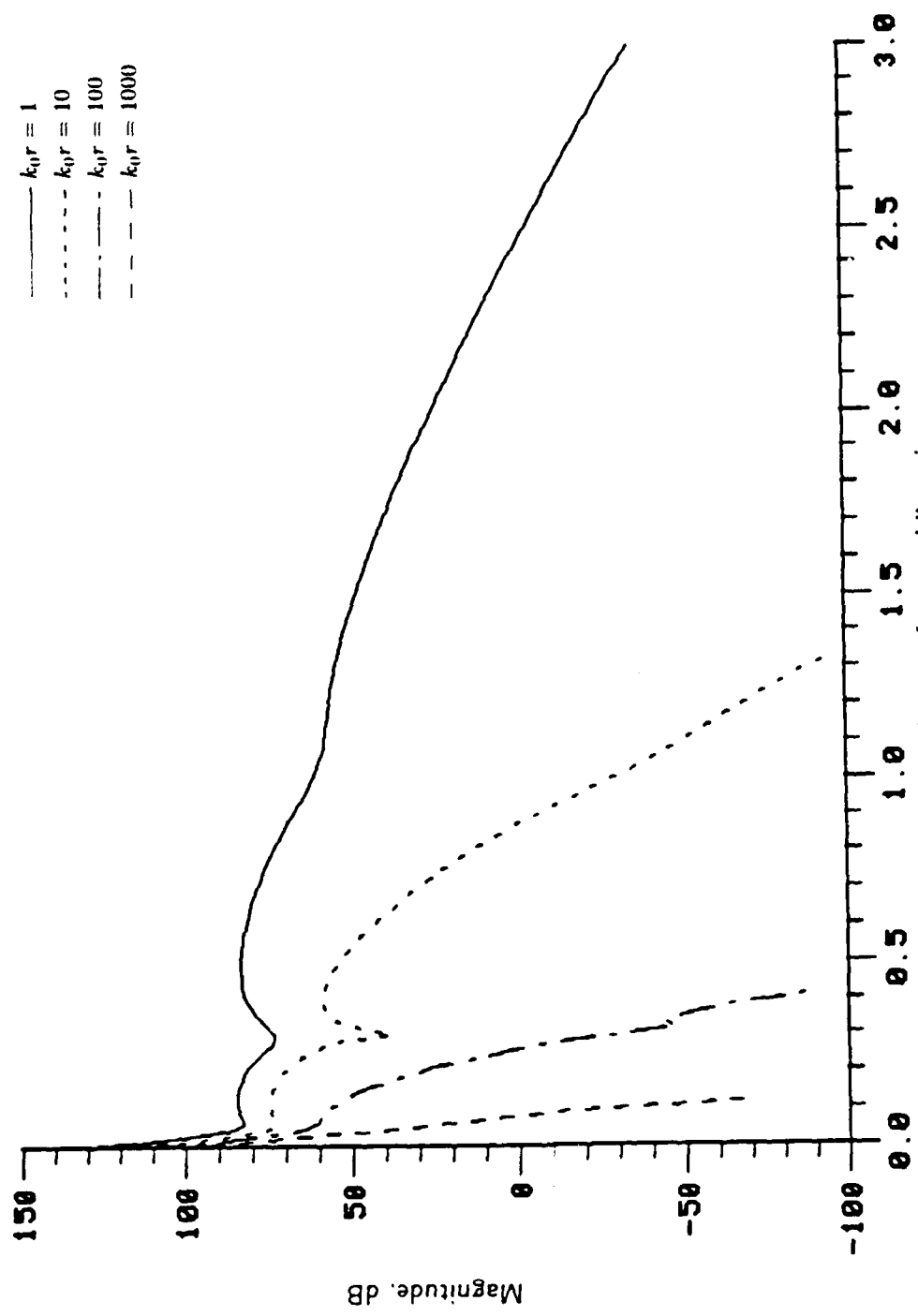


Figure 51 Magnitude of integrand along SDP-point-excited plate
at $\Omega = 10.0$ and $\phi = 34^\circ$.

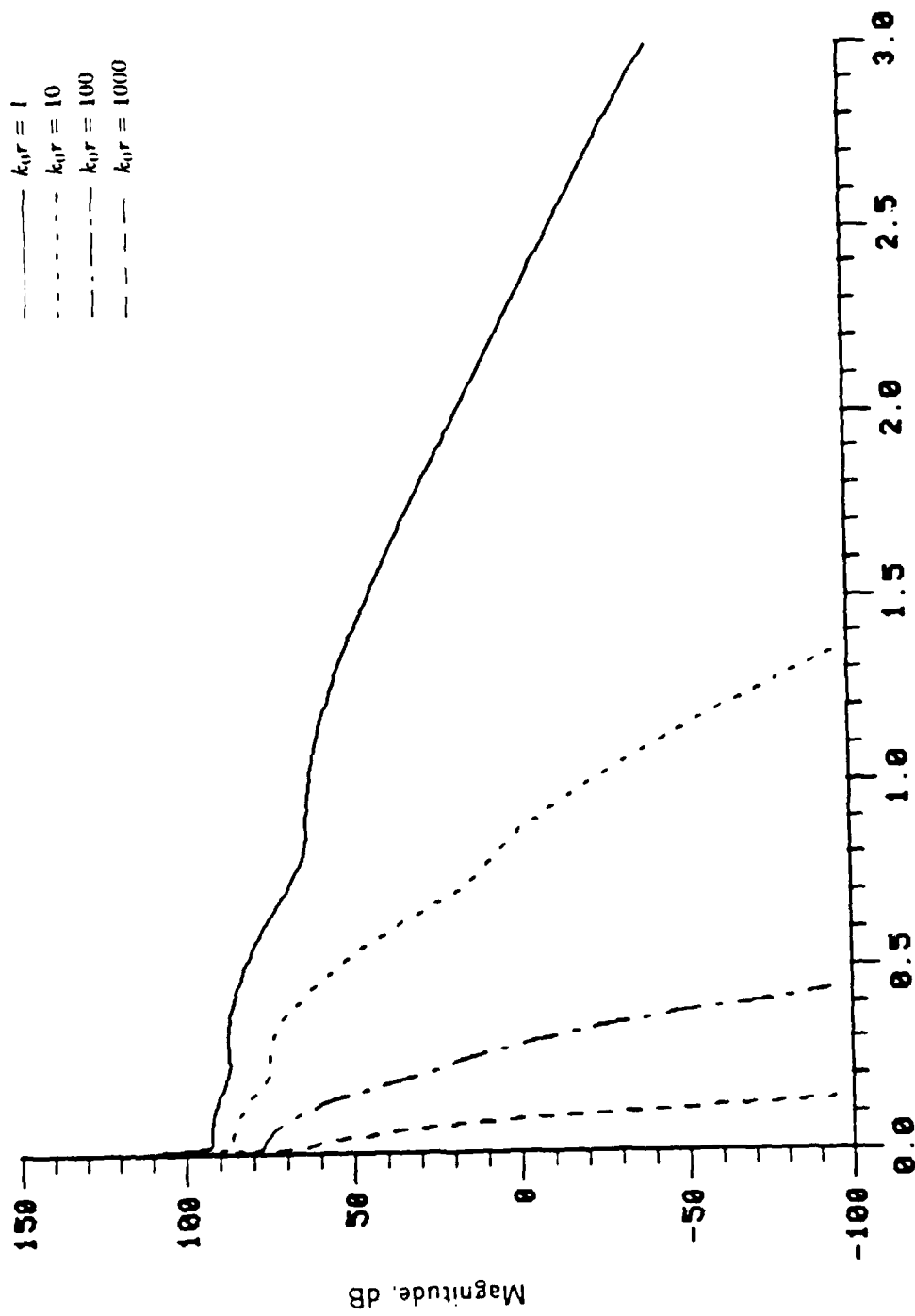


Figure 52 Magnitude of integrand along SDP-point-excited plate
at $\Omega = 10.0$ and $\phi = 11^\circ$.

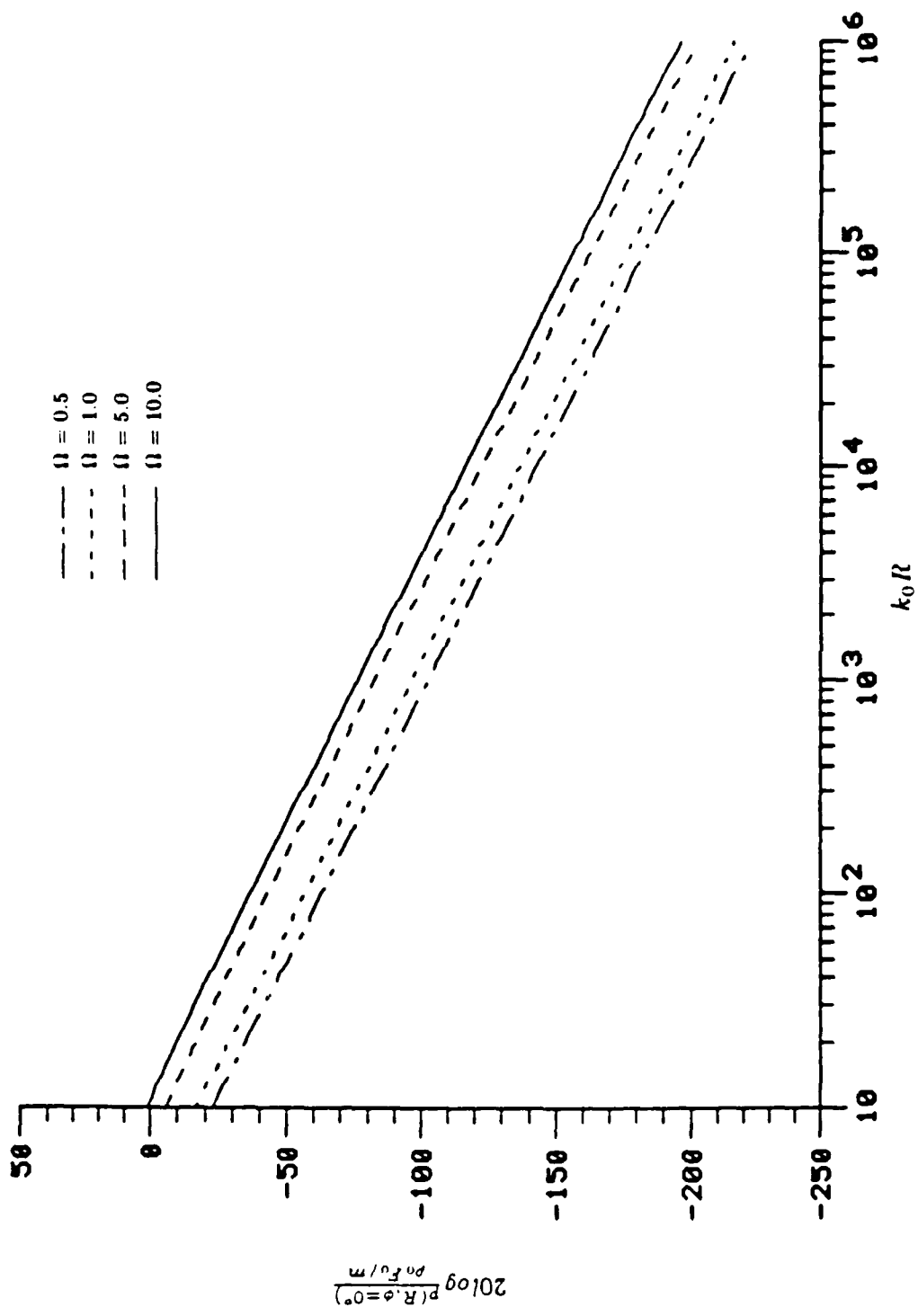


Figure 53 Radiated pressure from a point-excited steel plate. $\phi = 0^\circ$.

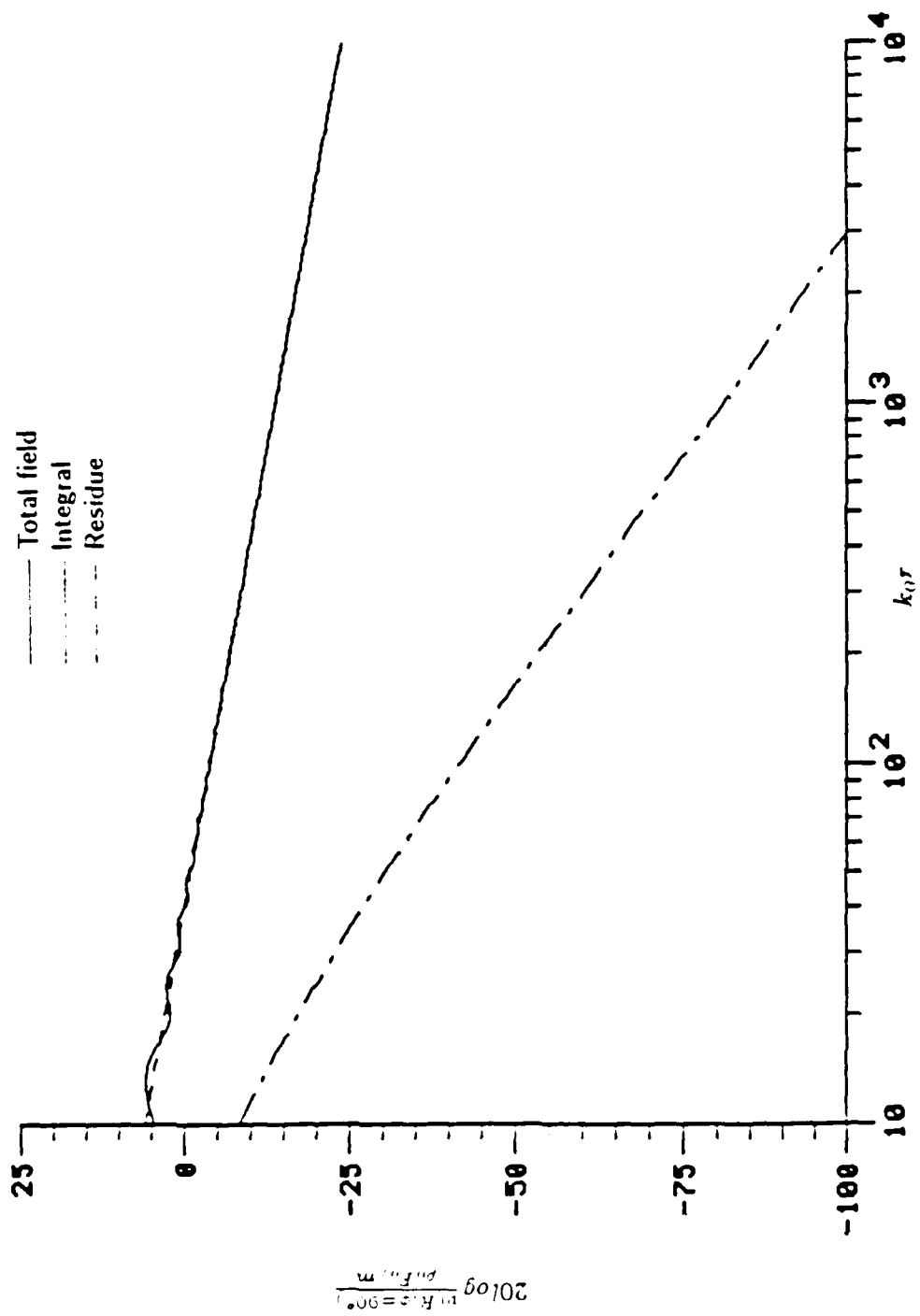


Figure 54 Grazing pressure field from a point-excited plate, $\Omega = 0.5$.

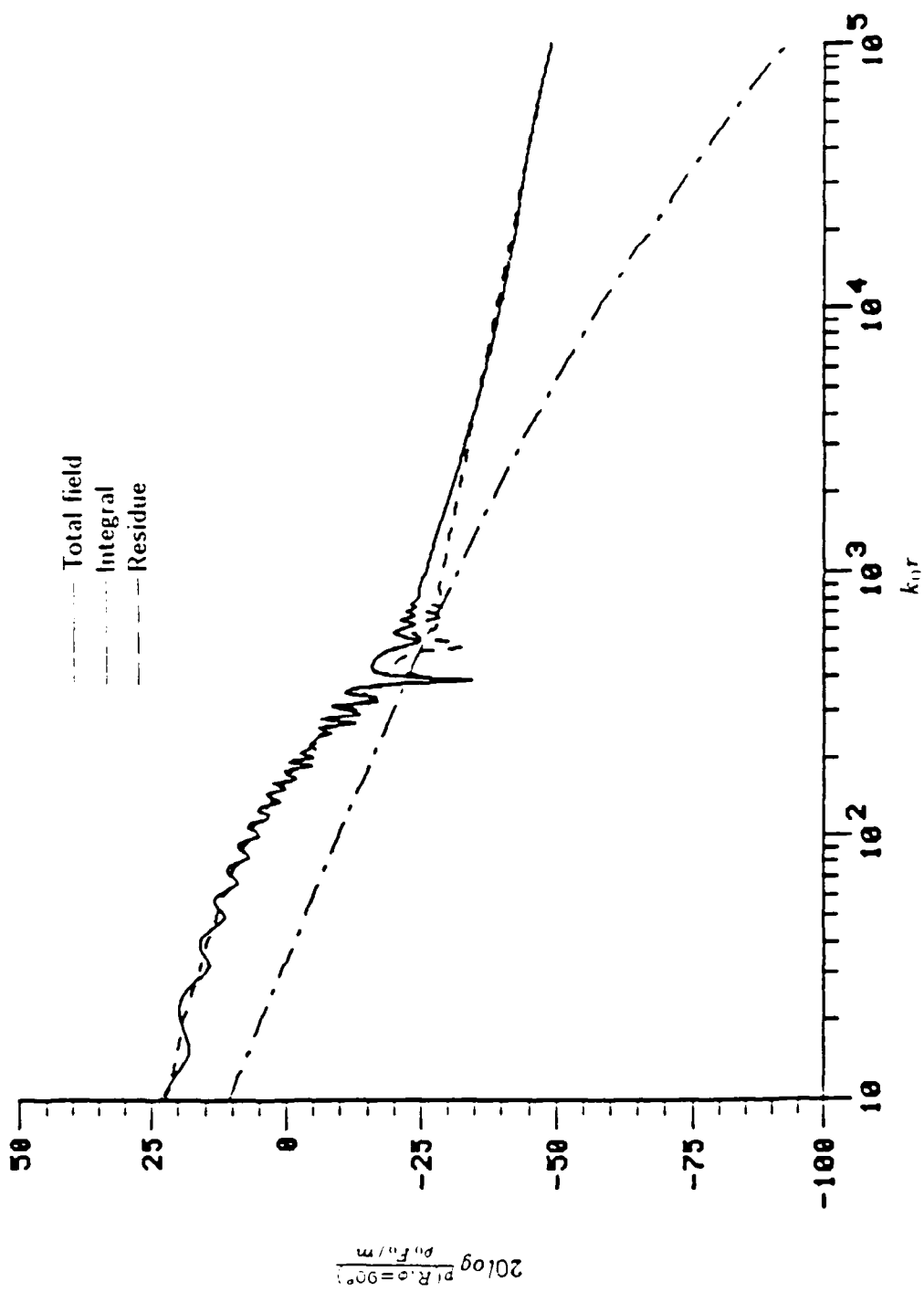


Figure 55 Grazing pressure field from a point-excited plate, $\Omega = 5.0$.

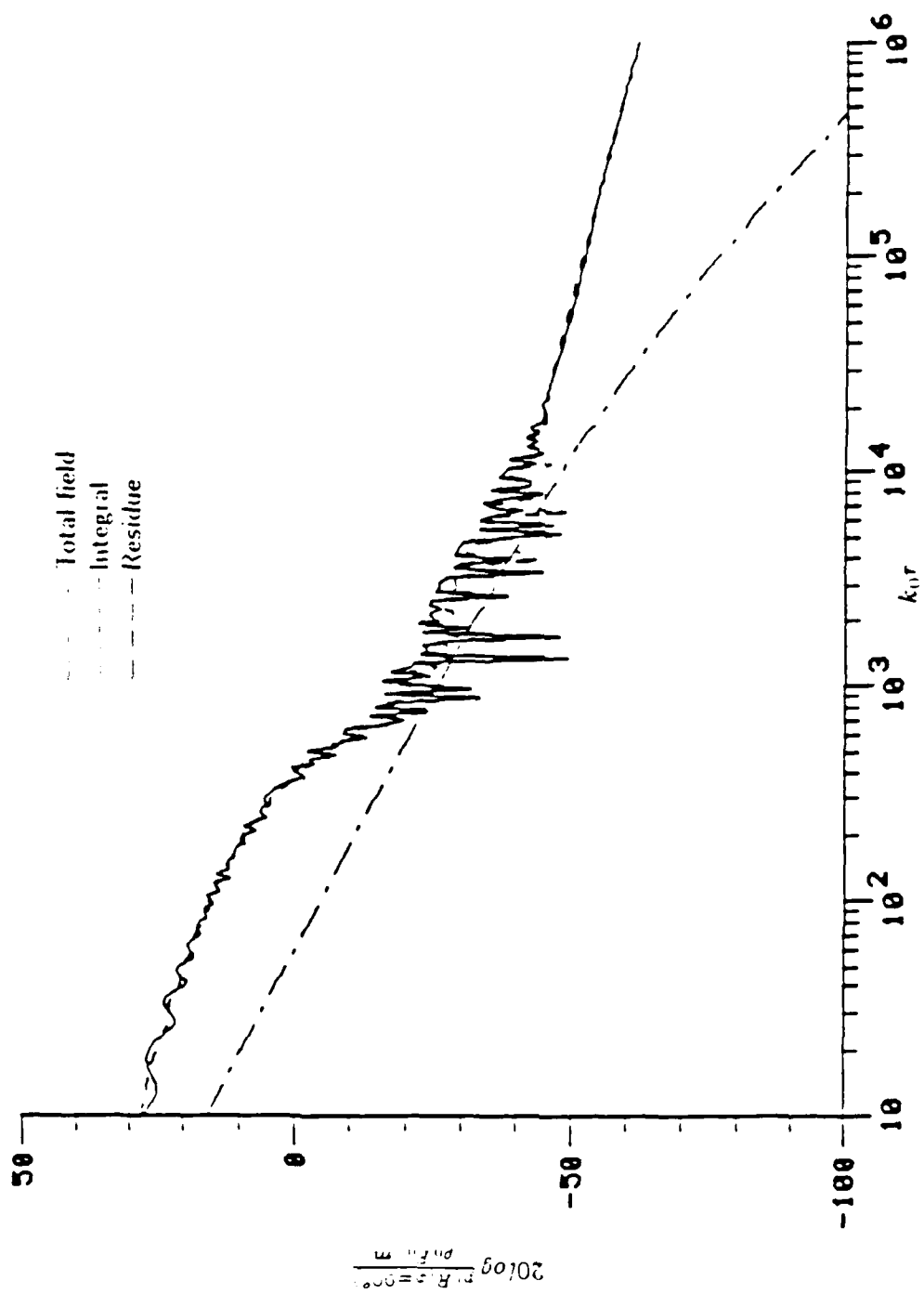


Figure 56 Grazing pressure field from a point excited plate. $\Omega = 10.0$.

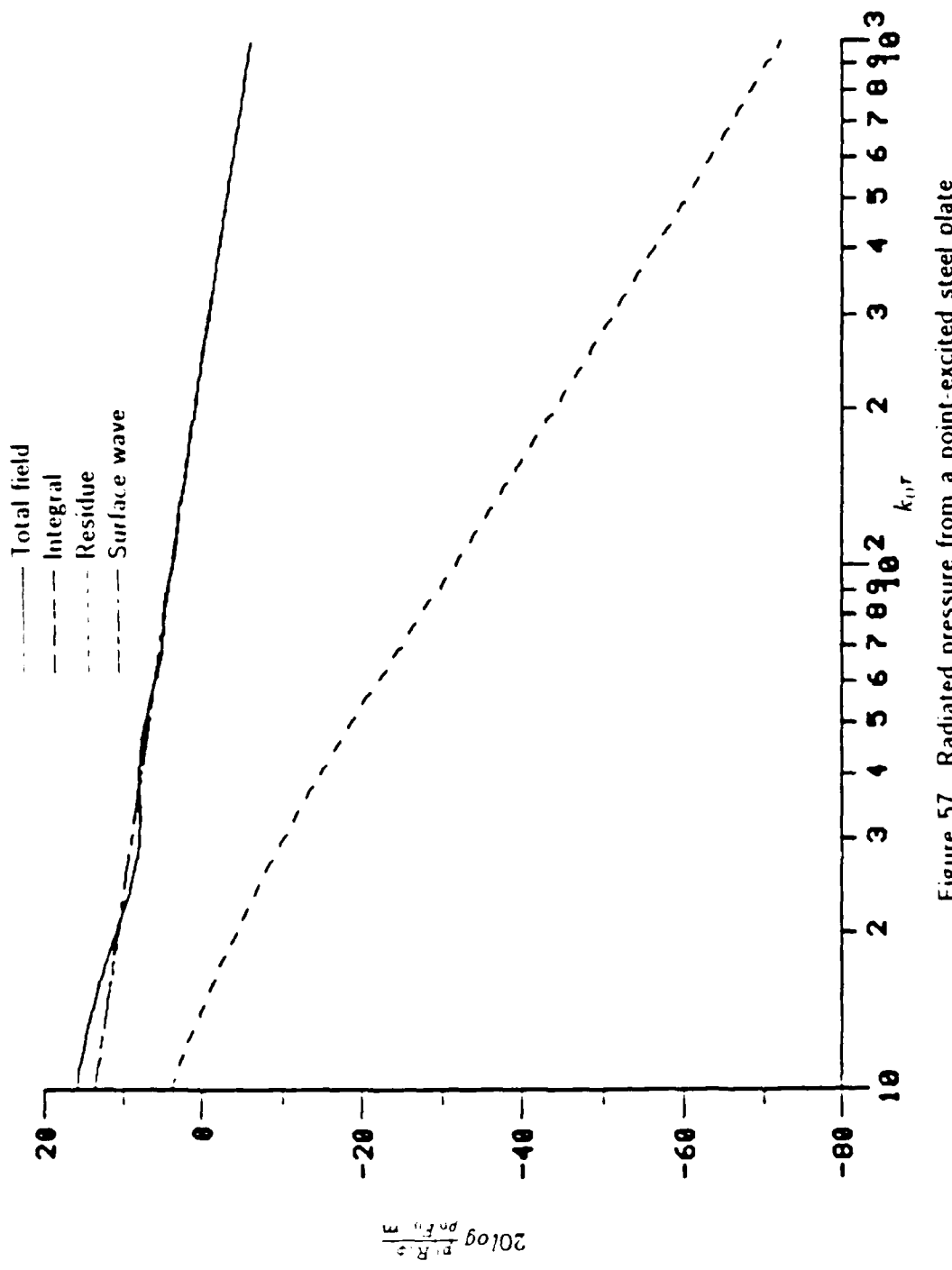


Figure 57 Radiated pressure from a point-excited steel plate
at $\Omega = 1.0$ and $z = 0.01\lambda$.

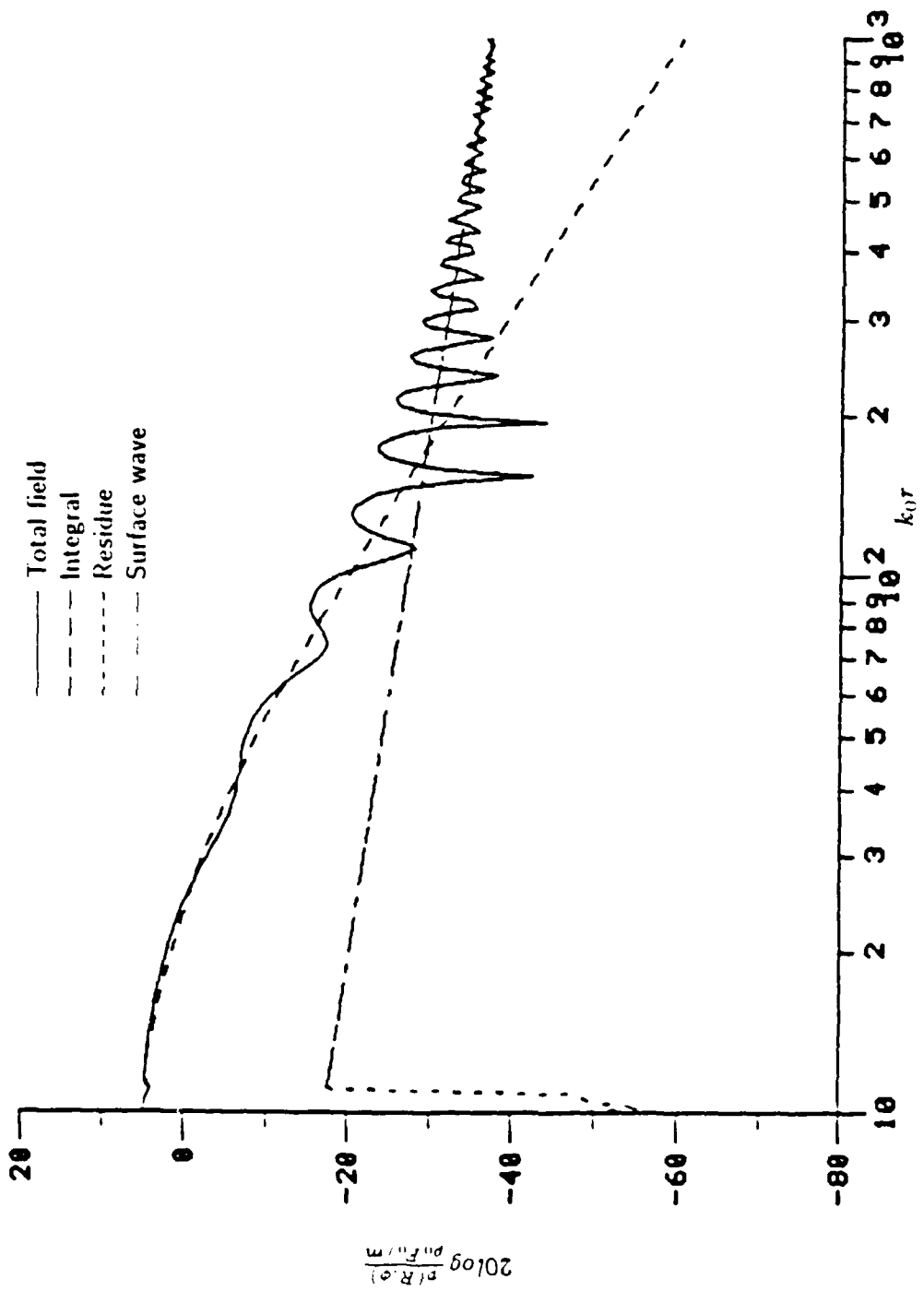


Figure 58 Radiated pressure from a point-excited steel plate
at $\Omega = 1.0$ and $z = 1.0\lambda$.

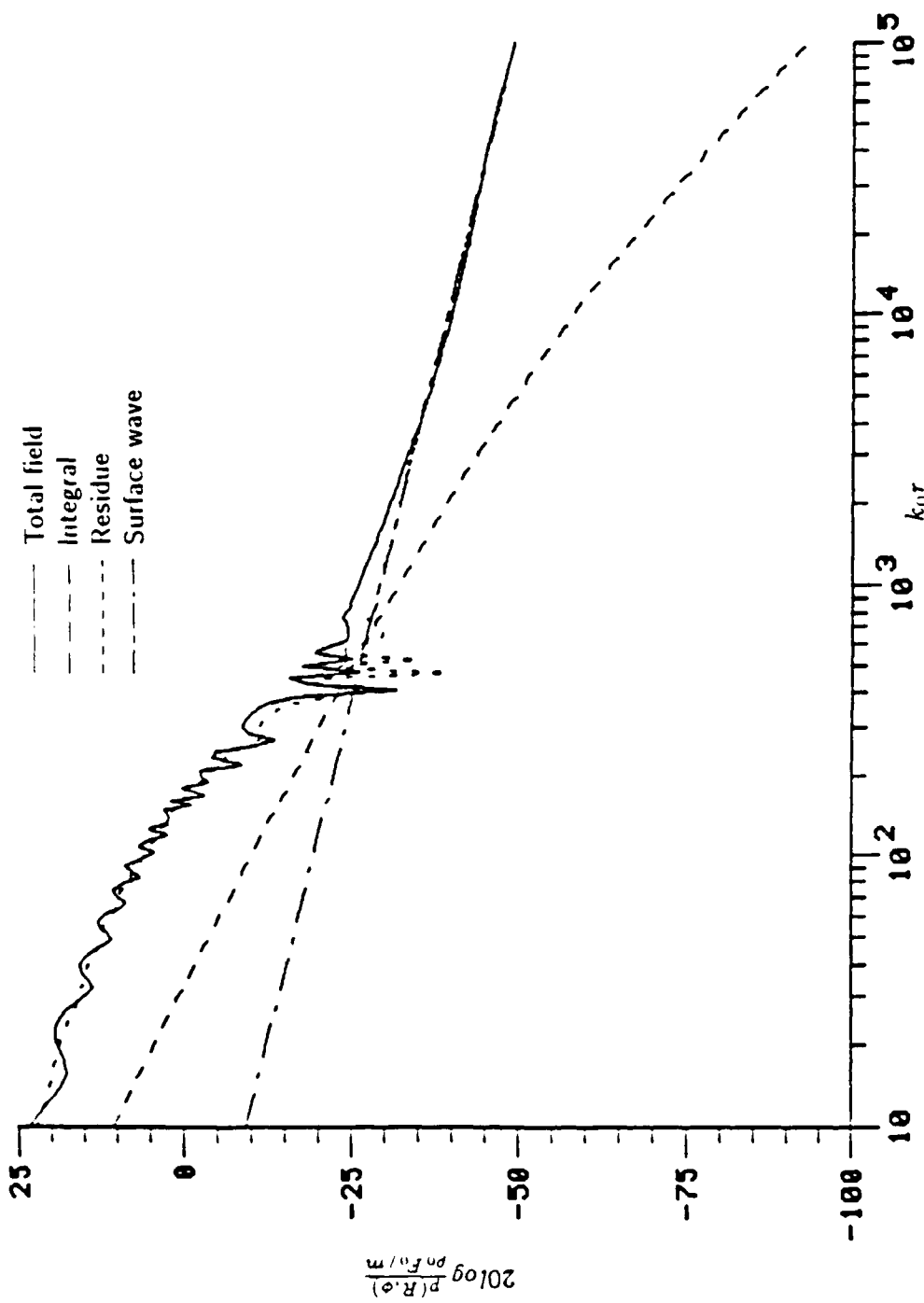


Figure 59 Radiated pressure from a point-excited steel plate
at $\Omega = 5.0$ and $z = 0.01\lambda$.

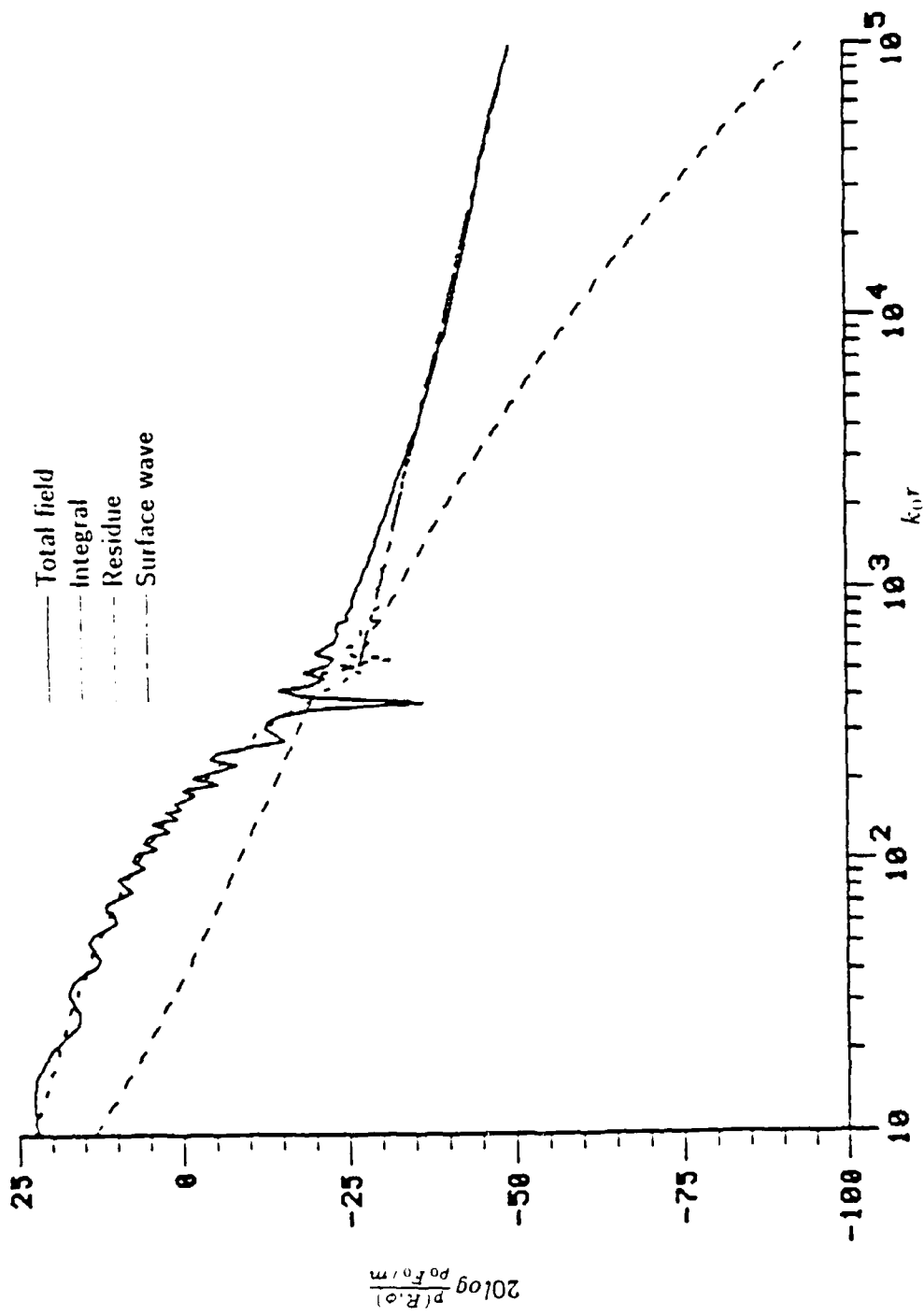


Figure 60 Radiated pressure from a point-excited steel plate
at $\Omega = 5.0$ and $z = 1.0\lambda$.

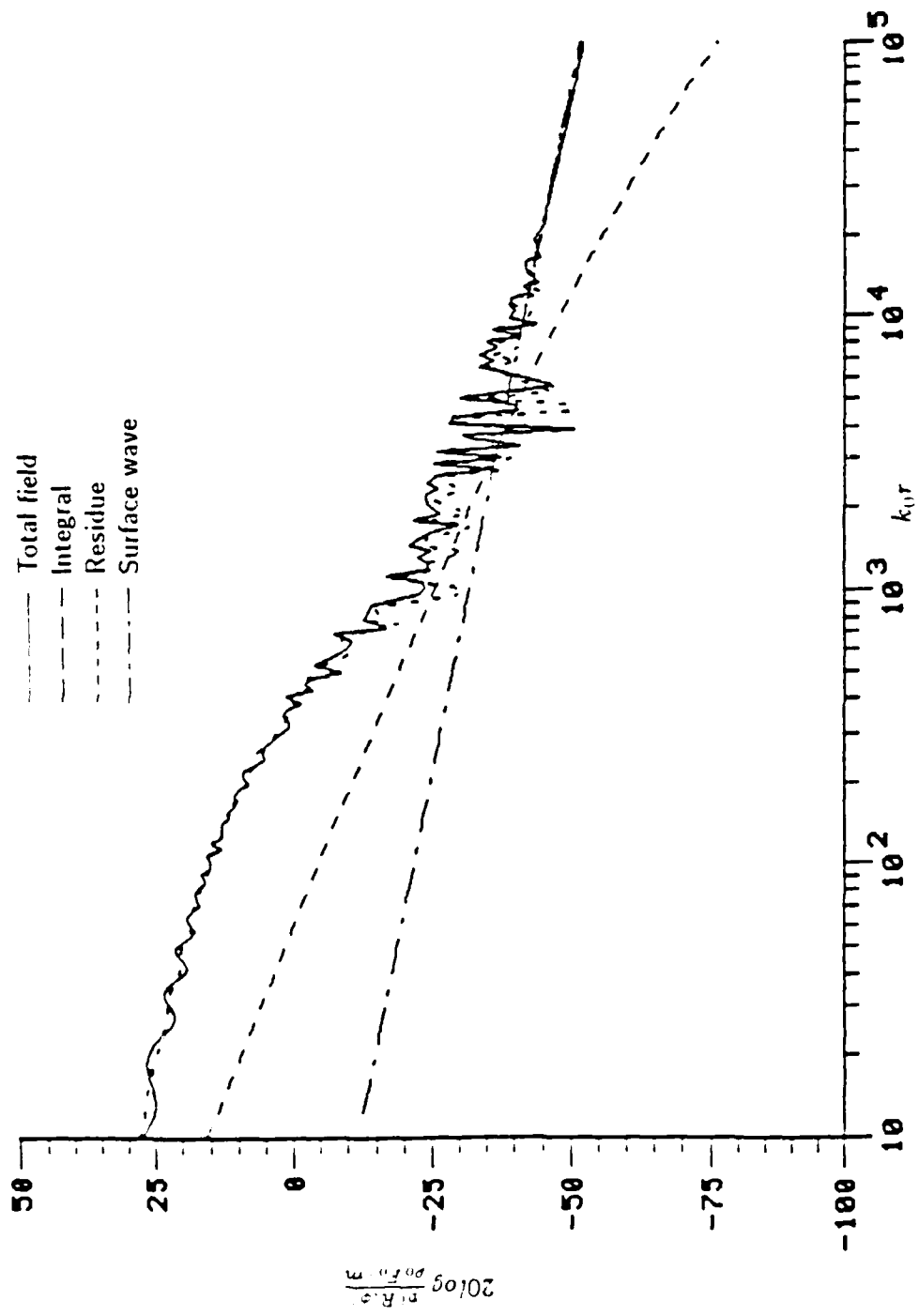


Figure 61 Radiated pressure from a point-excited steel plate
at $\Omega = 10.0$ and $z = 0.01\lambda$.

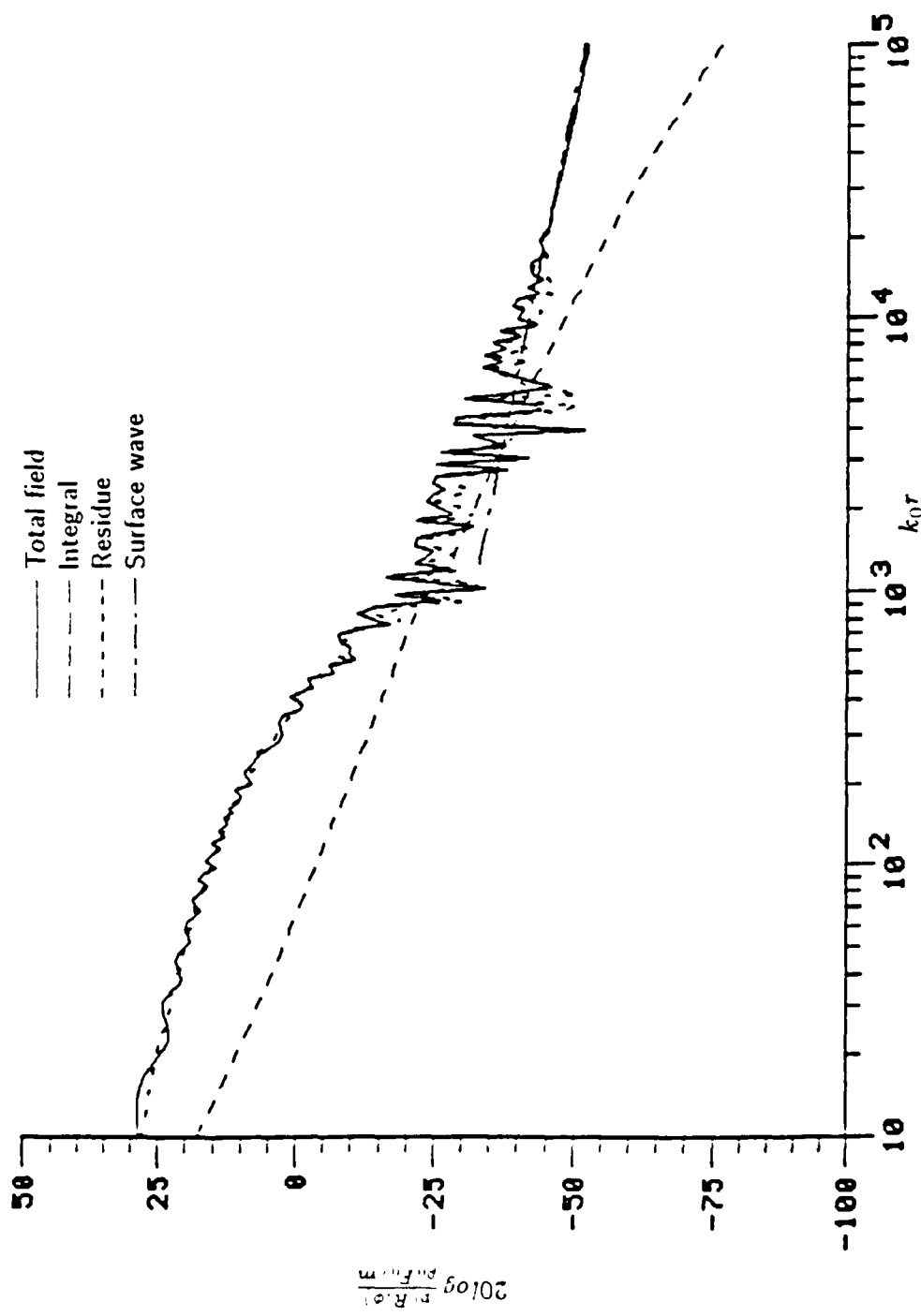


Figure 62 Radiated pressure from a point-excited steel plate
at $\Omega = 10.0$ and $z = 1.0\lambda$.

BIBLIOGRAPHY

1. Skudrzyk, E. J., Grundlagen der Akustik, Springer-Verlag, Vienna, 1954.
2. Skudrzyk, E. J., "Sound Radiation of a System with a Finite or Infinite Number of Resonances," J. Acoust. Soc. Am. 30, pp. 1152 (1958).
3. Heckl, M., "Sound Radiation from Point Excited Plates (in German)," Acustica 9, pp. 371-380 (1959).
4. Heckl, M., "Studies of Orthotropic Plates (in German)," Acustica 10, pp. 109-115 (1960).
5. Heckl, M., "Radiation from a Point Excited Infinitely Large Plate Under Water (in German)," Acustica 13, pp. 182 (1963).
6. Thompson, W., Jr. and Rattaya, J. V., "Acoustic Power Radiated by an Infinite Plate by a Concentrated Moment," J. Acoust. Soc. Am. 36, pp. 1488-1490 (1964).
7. Gutin, L. Y., "Sound Radiation from an Infinite Plate Excited by a Normal Point Force," Sov. Phys. Acoust. 10, pp. 369-371 (1965).
8. Feit, D., "Sound Radiation from Orthotropic Plates," J. Acoust. Soc. Am. 47, 388-389 (1970).
9. Skudrzyk, E. J., Simple and Complex Vibrating Systems, The Pennsylvania State University, University Park, 1968.
10. Maidanik, G. and Kerwin, E. M., Jr., "Influence of Fluid Loading on the Radiation from Infinite Plates Below the Critical Frequency," J. Acoust. Soc. Am. 40, pp. 1034-1038 (1966).
11. Feit, D., "Pressure Radiation by a Point-Excited Elastic Plate," J. Acoust. Soc. Am. 40, pp. 1489-1494 (1966).
12. Stuart, A. D., "Acoustic Radiation from Submerged Plates. I. Influence of Leaky Wave Poles," J. Acoust. Soc. Am. 59, pp. 1160-1169 (1976).
13. Stuart, A. D., "Acoustic Radiation from Submerged Plates. II. Radiated Power and Damping," J. Acoust. Soc. Am. 59, pp. 1170-1174 (1976).
14. Seren, C., "Acoustic Scattering from Ribs-Reinforced Plates- Uniform Asymptotic Solution," Ph.D. Thesis, The Pennsylvania State University, May 1986.
15. Mindlin, R. D., "Influence of Rotatory Inertia and Shear on Flexural Motions of Isotropic, Elastic Plates," J. Appl. Mech. 18, pp. 31-38 (1951).
16. Abramowitz, M. and Stegun, I. A., Handbook of Mathematical Functions, U. S. Department of Commerce, 1964.

17. Stuart, A. D., "Acoustic Radiation from a Point Excited Infinite Elastic Plate." Ph.D. thesis. The Pennsylvania State University, University Park, June 1972.
18. Crighton, D. G., "The Free and Forced Waves on a Fluid-Loaded Elastic Plate." J. Sound Vibr. 63, pp. 225-235 (1979).
19. Crighton, D. G., "The Free Waves on an Infinite Thin Fluid-Loaded Elastic Plate." J. Acoust. Soc. Am. 63, S9(A) (1978).
20. Pierucci, M. and Graham, T. S., "Unusual Characteristics of Free Bending Waves in Thick Plates with Fluid Loading." J. Acoust. Soc. Am. 62, S84 (1977).
21. Pierucci, M. and Graham, T. S., "A Study of Bending Waves in Fluid-Loaded Thick Plates." J. Acoust. Soc. Am. 65, pp. 1190-1197 (1979).
22. Strawderman, W. A., Ko, S. H. and Nuttall, A. H., "The Real Roots of the Fluid-Loaded Plate." J. Acoust. Soc. Am. 66, pp. 579-585 (1979).

APPENDIX

THE TAYLOR'S SERIES EXPANSION

In Eq. (77), the second integral, but not the exponential term, can be expanded into Taylor's series in x and y about $(x, y) = (0, 0)$. Since the integrands with odd power term in x will not contribute to the radiated acoustic pressure, only those with even power in x are considered. Thus,

$$\frac{1}{g(x, y) \sqrt{1 + \frac{x^2}{2}}} = -\sqrt{2} e^{-i\frac{\pi}{4}} \sum_{k=0}^{\infty} \sum_{l=0}^{\infty} f_{kl} x^{2k} y^{2l}, \quad (A-1)$$

where $g(x, y)$ is given in Eq. (74) and f_{kl} is the Taylor's series coefficient. For reference, the coefficients for an expansion through $x^4 y^4$ are given as follows:

$$\begin{aligned} f_{00} &= \frac{-1}{2 \sin \phi}, \\ f_{01} &= \frac{i}{8 \sin^3 \phi}, \\ f_{02} &= \frac{3}{64 \sin^5 \phi}, \\ f_{10} &= \frac{3i}{8 \sin^3 \phi}, \\ f_{11} &= \frac{7 + 8 \cos^2 \phi}{32 \sin^5 \phi}, \\ f_{12} &= \frac{-33i - 72i \cos^2 \phi}{256 \sin^7 \phi}, \\ f_{20} &= \frac{19 + 16 \cos^2 \phi}{64 \sin^5 \phi}, \\ f_{21} &= \frac{-i(75 + 240 \cos^2 \phi)}{256 \sin^7 \phi}, \\ f_{22} &= \frac{-(489 \sin^4 \phi - 3570 \sin^2 \phi \cos^2 \phi - 3465 \cos^4 \phi)}{2048 \sin^9 \phi}. \end{aligned} \quad (A-2)$$

Similarly, the second integrals in Eqs. (78-79) are expanded as

$$\frac{\sqrt{1 + \frac{x^2}{2}}}{g(x, y)} = -\sqrt{2} e^{-i\frac{\pi}{4}} \sum_{k=0}^{\infty} \sum_{l=0}^{\infty} g_{kl} x^{2k} y^{2l}, \quad (A-3)$$

where

$$\begin{aligned}
 g_{00} &= \frac{-1}{2\sin\phi}, \\
 g_{01} &= \frac{i}{8\sin^3\phi}, \\
 g_{02} &= \frac{3}{64\sin^5\phi}, \\
 g_{10} &= \frac{i(1+2\cos^2\phi)}{8\sin^3\phi}, \\
 g_{11} &= \frac{5+10\cos^2\phi}{32\sin^5\phi}, \\
 g_{12} &= \frac{-i(27+78\cos^2\phi)}{256\sin^7\phi}, \\
 g_{20} &= \frac{7+28\cos^2\phi}{64\sin^5\phi}, \\
 g_{21} &= \frac{-i(47\sin^4\phi + 330\sin^2\phi\cos^2\phi + 315\cos^4\phi)}{256\sin^7\phi}, \\
 g_{22} &= \frac{-(357\sin^4\phi + 3150\sin^2\phi\cos^2\phi + 3465\cos^4\phi)}{2048\sin^9\phi},
 \end{aligned} \tag{A - 4}$$

and

$$\frac{\chi}{g(\chi, y)} = \sum_{k=1}^{\infty} \sum_{l=0}^{\infty} h_{kl} \chi^{2k} y^{2l}, \tag{A - 5}$$

where

$$\begin{aligned}
 h_{10} &= \frac{-i\cos\phi}{2\sin^2\phi}, \\
 h_{11} &= \frac{-3\cos\phi}{8\sin^4\phi}, \\
 h_{12} &= \frac{i15\cos\phi}{64\sin^6\phi}, \\
 h_{20} &= \frac{-5\cos\phi}{8\sin^4\phi}, \\
 h_{21} &= \frac{i\cos\phi(27+8\cos^2\phi)}{32\sin^6\phi}, \\
 h_{22} &= \frac{\cos\phi(195-120\cos^2\phi)}{256\sin^8\phi}.
 \end{aligned} \tag{A - 6}$$

VITA

Hong-Yuan Hsu was born December 23, 1954, in Hsinchu, Taiwan. He graduated from Provincial Hsinchu Senior High School in June 1973, and received a B.S. degree in Naval Architecture from National College of Marine Science and Technology, Keelung, Taiwan, in June 1977, and an M.S. degree in Ocean Engineering from Florida Atlantic University, Boca Raton, Florida, in August 1983. From 1977 to 1979, he served in the Chinese Navy as a second lieutenant. From 1979 to 1981, he was employed by the United Ship Design and Development Center, Taipei, Taiwan, as a structural engineer in the area of ship structural design and analysis. In August 1983, he joined the Department of Engineering Science and Mechanics at The Pennsylvania State University, University Park, Pennsylvania, for his Ph.D. study.

END
DATE
FILMED
MARCH
1988

DTIC